Application of the discrete element method for concrete fracturing.

Tang, Lingwei

Swansea University
Prifysgol Abertawe

APPLICATION OF THE DISCRETE ELEMENT METHOD FOR CONCRETE FRACTURING

Lingwei Tang

SUBMITTED TO THE SWANSEA UNIVERSITY IN FULFILMENT OF THE REQUIREMENTS FOR THE DEGREEE OF DOCTOR OF PHILOSOPHY

SWANSEA UNIVERSITY

2013

DECLARATION AND STATEMENTS

Declaration

This work has not previously been accepted in substance for any degree and is not being concurrently submitted in candidature for any degree.

Signed ....(candidate)

Date.....22.07.2013.....

Statement 1

This thesis is the result of my own investigations, except where otherwise stated. Where correction services have been used, the extent and nature of the correction is clearly marked in a footnote(s).

Other sources are acknowledged by footnotes giving explicit references. A bibliography is appended.

Signed ....(candidate)

Date.....22.07.2013.....

Statement 2

I hereby give consent for my thesis, if accepted, to be available for photocopying and for inter-library loan, and for the title and summary to be made available to outside organizations.

Signed ....(candidate)

Date.....22.07.2013.....

ABSTRACT

This project focuses on discrete element modelling of fracturing of concrete material at meso-scale, and particularly on calibration of the particle assembly parameters to reproduce phenomenological properties of concrete, and on applying the discrete element method to analyze the failure mechanisms in a three-point bending test and debonding between the FRP sheet and the concrete. The particle flow code *PFC2D* and *PFC3D* are employed to carry out the parametric study but only *PFC2D* is used in the case studies.

The calibration of properties of the numerical samples is conducted to determine the effects of the particle level input parameters on the elastic constants, the uniaxial compressive strengths and failure mode of particle assembly. The input parameters are divided into two groups, model constitutive parameters (e.g., particle and bond stiffness, bond shear and normal strengths and friction coefficient) and geometric and physical parameters (e.g., particle and specimen size, particle distribution and loading velocity.). The analysis is constructed using dimensional analysis and numerical uniaxial tests.

A random aggregate generation algorithm is incorporated in the DEM code to reproduce the aggregate structure in real concrete material. The aggregate generation algorithm utilizes polygon and polyhedron as the basic shapes of aggregate and is capable of producing multi-graded concrete specimens with aggregate content up to 80% and 60% for two-dimensional and three-dimensional samples respectively.

The mode I fracture behavior of three-phased concrete is then simulated by performing a virtual three-point bending test. The mortar matrix phase is simulated with the linear elastic-pure-brittle and softening bond model to ensure a fair

comparison. The dynamic debonding process between the FRP sheet and the concrete is simulated with a particle assembly by a regular hexagonal packing arrangement where the heterogeneity of concrete is taken into account by incorporating the Weibull distribution.

Based on the analysis of the modelling results, it is conclude that the fracture behavior of concrete can be satisfactorily captured by meso-scale DEM model and comprehensive parameter study allows more confidently implementation of particle flow code.

ACKNOWLEDGEMENT

I wish to express my deep and sincere gratitude to many individuals. This thesis would not have been completed without their contributions.

I am grateful to my supervisor, Professor Y.T. Feng, for his guidance, support, constant encouragement and amazing patience during the course of this research.

To Dr. Jianwen Pan at Tsinghua University for his suggestion and inspiration, without his experience, knowledge, I would have been lost my way.

To Dr. Dongming Yang for his valuable discussions and help on application of numerical code *PFC*.

To my friends and colleagues, Dr. Feng Wang, Jianwen Feng, Liang Yang, Songgui Chen and many others, for making my life enjoyable through all my years in Swansea.

And last but not least, to my family: my wife, Qing Chen, for her unconditional love and support, my parents and parents in law for their love and belief in me.

CONTENTS

LIST OF FIGURES

LIST OF TABLES

Chapter 1
Introduction

As an artificial quasi-brittle material, modeling the mechanical behavior of concrete is one of the most challenging fields of modern computational solid mechanics. Concrete is one of the most common engineering materials applied in a wide range of engineering applications (e.g, dams, bridges, offshore platforms, nuclear power stations, tunnels). Since the nineteen seventies, researches on concrete materials and engineering structures have advanced from linear elasticity to nonlinear elastic-plastic fracture mechanics; from continuum mechanics to discrete mechanics; from homogeneous isotropic medium to heterogeneous anisotropic medium; from small deformation assumption to large deformation and simulation of damage process; from macro mechanical model to investigation of mechanical behavior from meso and micro scale point views. The remarkable progress of the above aspects mainly relies on the rapid development in modern science and technology.

Traditional concrete mechanics is based on the assumption of homogeneity. However, in reality the heterogeneity of concrete manifests itself at various levels. As a synthetic composite material, natural or man-made defects, damage, microcracks, cavities and inclusions exist in concrete. In order to reflect these characteristics, Wittmann (Wittmann *et al.*, 1985b) pointed out that concrete is a typical multiscale material with different structural details appearing at different levels of observation.

The three distinct levels are micro-, meso- and macro-levels.

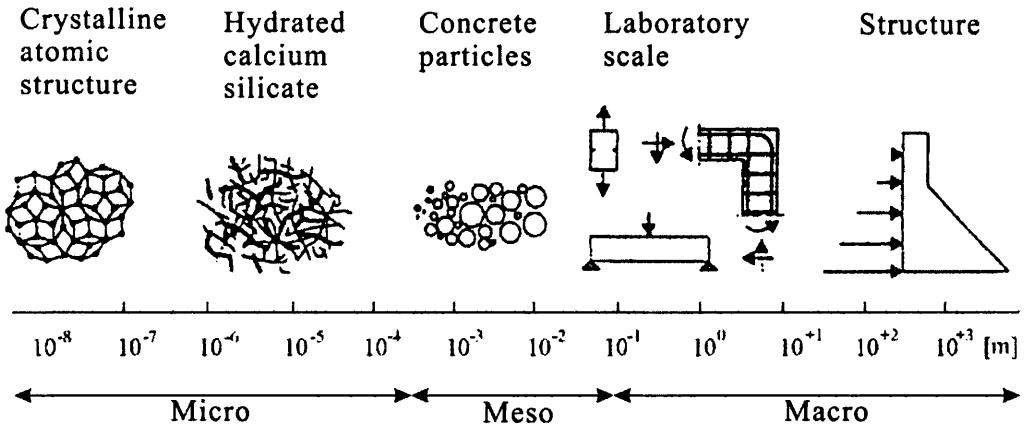

Figure 1.1: Schematic diagram of concrete material (Wittmann *et al.*, 1985a).

At meso-scale level, concrete is a nonhomogeneous material which consists of sand and aggregates embedded in a cement paste matrix and that the fracture mechanism is related to its meso- and micro-structure. The weak interfaces between the aggregates and the mortar matrix dominate the properties of the material on the macro-scale (Bentz *et al.*, 1995). The deformation and fracture of concrete are associated with complicated progressive failure, as characterized by initiation, propagation, and coalescence of microcracks due to material heterogeneity (Tang *et al.*, 2009).

Over the last two decades, two distinguished approaches, micromechanical or phenomenological based, have appeared in the field of brittle material science. The micromechanical approach is physically well-grounded but suffers from inherent complexity and restricted applicability; The phenomenological approach introduces the intrinsic variable to describe damage states of the material while at the mean time remains a macro-mechanical constitutive relationship (Halm *et al.*, 2002).

In recent years, there has been growing interest in numerically modeling the fracture process and evaluating the macro-scale response of concrete by meso-scale models. Typically meso-scale models includes: the M-H meso-scale mechanical model presented by Mohamed and Hansen (Mohamed and Hansen, 1999a, b), the lattice model presented by van Mier et al. (Schalangen and J.G.M. van Mier, 1994), the

meso-scale elastic-brittle model presented by Tang (Tang *et al.*, 2000a; Tang *et al.*, 2000b) and the particle based model presented by Cundall et al. (Cundall and Strack, 1979), and Bazant et al.(Bazant *et al.*, 1990).

This research project intends to numerically investigate the fracture process of concrete by meanings of the meso-scale particle based DEM model. The discrete element code *PFC* (particle flow code) (Itasca, 1999) will be used to carry out the modelling.

The discrete element method, one of the most popular particle based approaches, was originally proposed by Cundall (Cundall, 1971) for rock-mechanics problem, then applied to soils (Cundall and Strack, 1979). Since then it has been widely used as one of numerical methods for modeling soil and rock-like materials. The DE approach is based on discontinuous mechanics and the basic idea is to model the elements as rigid simple geometric entities such as disks, spheres, ellipses, or ellipsoids, so that Newton's equations of motion can be applied to entities individually. In addition, in order to obtain the response as an assembly system, the specified interaction forces between the particles are introduced based on an appropriate physical interaction law. The most significant advantage over the traditional continuum approach is the way that DEM discreteness a material domain, as dynamic material behaviour of composites, crack tip singularities and crack formulation criteria can all be avoided due to the naturally discontinuous representation of concrete materials via particle assemblies (Fakhimi and Villegas, 2006).

In general, DEM specifies properties for both particles and the contacts between them at a micro-scale, e.g., contact stiffnesses, bond strengths, friction coefficient between particles. However, unlike the continuum approach, the input parameters for the discrete particle assembly are unknown in advance. The discrete element models will behave differently for different input micro-parameter values, and accurate results can only be obtained if a correct relationship between the micro-parameters and the

macro-properties are specified. To determinate the proper input micro-parameters becomes one of the main challenges in the field of particle based approaches.

1.1 Objectives and scope of the dissertation

The overall aim of this research is to improve the understanding of the fracture behaviour of concrete by meanings of the meso-scale DEM model. The specific abjectives are:

1. To develop 2D and 3D random aggregate structure generation algorithms to accurately and efficiently describe aggregate distribution of concrete at meso-scale level.

2. To exam factors at meso scale that influence macro material deformability, strength and fracture behavior in DEM modeling, and to investigate the potential benefits of discrete element techniques, as well as the shortcomings.

3. To model the damage progression in concrete at meso-scale level under mode I fracture by utilizing random aggregate structure generation algorithms developed earlier.

4. To simulate the dynamic failure process in the FRP-to-concrete interface by adopting regular particle assembly.

1.2 Layout of dissertation

This dissertation consists of eight chapters. The present chapter is the introduction. The brief synopsis of the remaining chapters is as follows:

Chapter 2 presents a concise review of numerical methods for modelling the concrete damage at various scales, together with an overview of aggregate generation and

disposition algorithms and studies of the discrete element model and micro-parameter.

Chapter 3 introduces the theoretical background and constitutive laws of the discrete element method.

Chapter 4 describes methodology and rationale of the generation of random aggregate structures in detail. In particular, the background grid based algorithm which is employed in later meso-scale concrete fracture simulations is tested and verified.

Chapters 5 and 6 establish the scaling laws between the macro-material properties and governing factors at meso scale for DEM models. The factors governing the elastic constants, uniaxial compressive and failure mode of parallel bonded model are identified. Both 2D and 3D models are considered and compared with each other. The governing factors are dividing into two distinguished groups. Chapter 5 mainly focuses on physical parameters such as loading velocity, degree of discretization and particle size distribution. Chapter 6 investigates the effects of model constitutive micro-parameters and empirical equations are presented.

Chapter 7 presents a meso-scale DEM model for concrete under pure mode-I fracture. Both linear elastic-purely-brittle and softening contact models are considered for the mortar matrix phase to compare their effects.

Chapter 8 simulates the dynamic failure process in the FRP-to-concrete interface by meanings of a regular packed DE model. The heterogeneity of concrete is taken into account statistically by utilizing a Weibull distribution to micro-parameters.

Chapter 9 concludes the research work done in this dissertation and recommends some potential future work.

References

Bazant, Z.P., Tabbara, M.R., Kazemi, M.T., Pijaudier-Cabot, G., 1990. Random particle model for fracture of aggregate or fiber composites. Journal of engineering mechanics 116, 1686-1705.

Bentz, D., Schlangen, E., Garboczi, E., 1995. Computer simulation of interfacial zone microstructure and its effect on the properties of cement-based composites. Materials science of concrete IV, 155-200.

Cundall, P.A., 1971. A Computer Model for Simulating Progressive Large Scale Movements in Blocky Rock Systems, Proceedings of the Symposium of the International Society of Rock Mechanics, Nancy, France, pp. Paper No. II-8.

Cundall, P.A., Strack, O.D.L., 1979. A discrete numerical model for granualar assemblies. Geotechnique 29, 47-56.

Fakhimi, A., Villegas, T., 2006. Application of Dimensional Analysis in Calibration of a Discrete Element Model for Rock Deformation and Fracture. Rock Mechanics and Rock Engineering 40, 193-211.

Halm, D., Dragon, A., Charles, Y., 2002. A modular damage model for quasi-brittle solids–interaction between initial and induced anisotropy. Archive of Applied Mechanics 72, 498-510.

Mohamed, A.R., Hansen, W., 1999a. Micromechanical Modeling of Concrete Response under Static Loading—Part 1: Model Development and Validation. Materials Journal 96, 196-203.

Mohamed, A.R., Hansen, W., 1999b. Micromechanical modeling of concrete response under static loading: Part II - Model predictions for shear and compressive loading. ACI Materials Journal 96, 354-358.

PFC2D, 1999. Particle flow code in 2 dimensions. Itasca Consulting Group, Inc.

PFC3D, 1999. Particle flow code in 3 dimensions. Itasca Consulting Group, Inc.

Schalangen, E., J.G.M. van Mier, 1994. Simple lattice model for numerical simulation of fracture of concrete materials and structures. Materials and structures 25, 534-542.

Tang, C.A., Liu, H., Lee, P.K.K., Tsui, Y., Tham, L.G., 2000a. Numerical studies of the influence of microstructure on rock failure in uniaxial compression — Part I: effect of heterogeneity. International Journal of Rock Mechanics and Mining Sciences 37, 555-569.

Tang, C.A., Tham, L.G., Lee, P.K.K., Tsui, Y., Liu, H., 2000b. Numerical studies of the influence of microstructure on rock failure in uniaxial compression — Part II:

constraint, slenderness and size effect. International Journal of Rock Mechanics and Mining Sciences 37, 571-583.

Tang, X., Zhang, C., Shi, J., 2009. A multiphase mesostructure mechanics approach to the study of the fracture-damage behavior of concrete. Science in China Series E: Technological Sciences 51, 8-24.

Wittmann, F.H., Roelfstra, P.E., Sadouki, H., 1985. Simulation and analysis of compositestructures. Materials science and engineering 68, 239-248.

Chapter 2
Literature review

2.1 Concrete damage and fracture mechanism and failure characteristics

Concrete is a typical heterogeneous composite material consisting of microscopic defects such as microcracks, macro crack, slag, bubbles, pores and segregation. The strength, deformation and damage mode are mainly governed by crack initiation and propagation. Submicroscopic analysis of concrete internal structure (Mindess, 1991) revealed that the existence of cracks even before loading due to the intrinsic volume changes in concrete caused by shrinkage or thermal movements. These pre-exist cracks can be classified into two groups: 1) random distributed microcracks which govern the tensile and compressive strength; and 2) oriented macro cracks which lead to the anisotropic behavior of concrete. Ortiz (Ortiz, 1988) suggested that pre-exist microcracks have double effects on the fracture process. On one hand, macro crack growth is initiated by coalescence of microcracks, on the other hand, micro-cracks cause toughness degradation and shielding. Damage of concrete is originally caused by the inherent defects in the system, and the failure process is essentially the process

of cracks initiation, propagation, coalescence which eventually cause concrete fractured into separate pieces.

One of the most important issues is the recognition that concrete is not a perfectly brittle material in the linear sense, but that it has some residual load-carrying capacity after reaching the tensile strength (de Borst, 2002). A substantial non-linearity exists before the maximum stress (Fig.2.1). Thus, concrete is often classified as a quasi-brittle material. The failure process can be divided into at least three stages (Neville, 1995). Taking uniaxial compression or tension as an example, the first stage within the 30-40% compressive strength range (60% for tensile strength), strain localization appears at isolated points throughout the specimen where the tensile strain concentration is the largest. Localized microcracks are initiated but they are stable and do not propagate. Because the energy released by these microcracks is very small, the stress-train curve is almost linear. As the applied load is increased beyond the first stage, initially stable cracks begin to propagate. There will not be clear distinction between the first stage and the second stage since stable crack initiation is likely to overlap crack propagation and there will be a gradual transition. However, in some literatures the transition point is still referred to as the proportional limit. During this stage the crack system multiplies and propagates in a slow stable manner. If loading is stopped and the stress level remains constant, propagation ceases. The extent of the stable crack propagation stage will depend upon the applied state of stress, being very short for predominantly tensile stress states and longer for predominantly compressive states of stress. This steady-state propagation of crack implies that there is a small fracture process zone ahead of the crack tip. The mechanisms of deformation beyond the proportional limit are not fully understood. The final stage occurs when the crack system becomes unstable and the release of strain energy is sufficient to make the cracks self-propagate until a complete disruption and failure occurs. This stage starts at about 70-90% of the ultimate strength (referred to as initiation of strain localization in Fig.2.1), once this stage is

reached failure will occur whether or not the stress is increased.

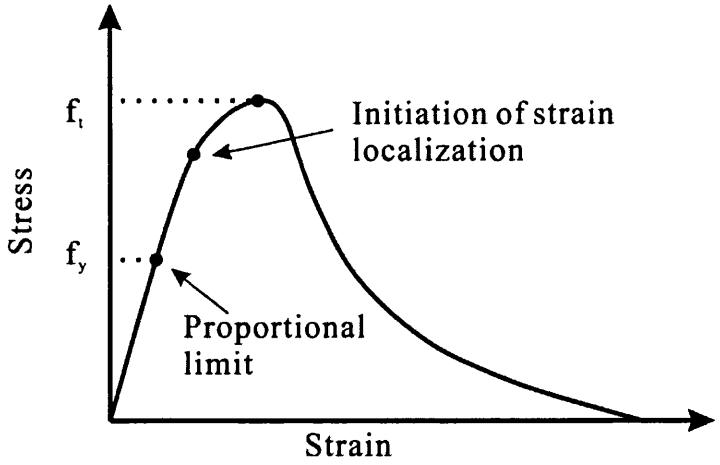

Figure 2.1: Typical tensile stress-strain curve for quasi-brittle material.

2.2 Fracture mechanics of concrete materials

Fracture mechanics applies the physics of stress, strain and energy release rate, in particular the theories of elasticity and plasticity, to the microscopic crystallographic defects to predict the macroscopic mechanical failure. The foundation for fracture mechanics was laid by Griffith in the early thirties for brittle materials (Glass) (Griffith, 1921). His work was largely ignored by the engineering community until the early 1950s. Irwin (Irwin, 1957) made significant modification and since then it has been mostly applied to metallic materials and formed linear elastic fracture mechanics (LEFM). Irwin stresses out that any fracture can be described in terms of the three fundamental cases of fracture: I. the symmetrical opening case, II. the sliding case, and III. the tearing case (Fig.2.2).

The pioneering effort to apply linear elastic fracture mechanics to concrete is conducted by Kaplan (Kaplan, 1961). Since the work of Kaplan, many attempts have been made to apply LEFM principles to fracture in concrete (Barsoum, 1976; Ingraffea *et al.*, 1984; Ingraffea and Manu, 1980; Shih *et al.*, 1976). As realized in 1971 by Shah and McGarry (Shah and McGarry, 1971) LEFM with one fracture

parameter cannot be directly applied due to the presence of a sizeable facture process zone in concrete material.

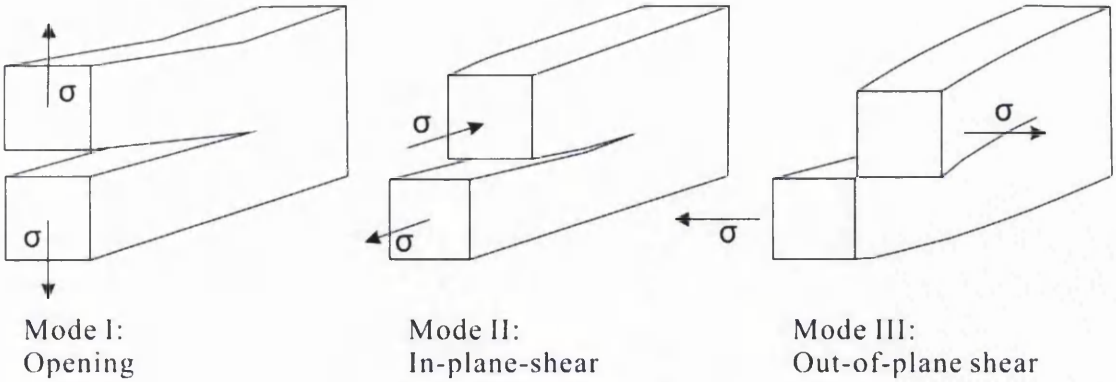

Figure 2.2: The fundamental cases of fracture

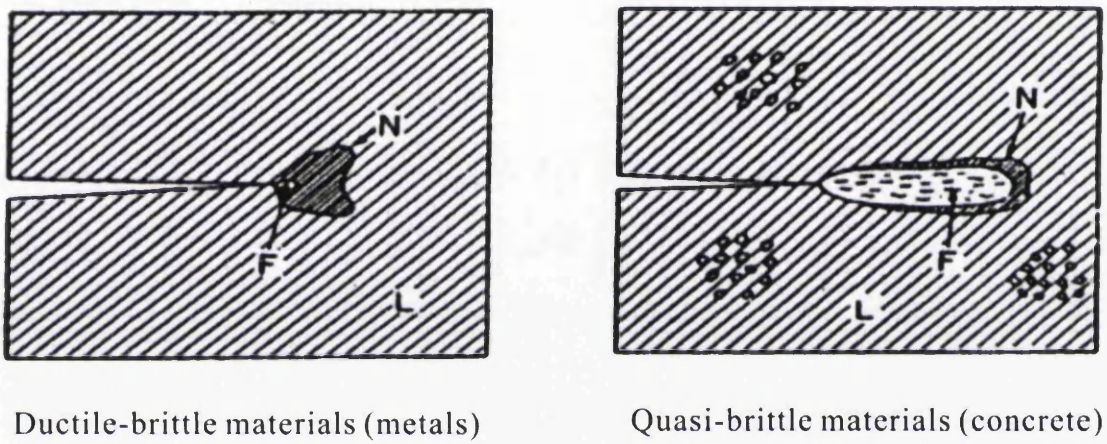

Figure 2.3: Fracture process zone in brittle-ductile materials.

The fracture behaviour of concrete is greatly influenced by the fracture process zone although it is quite small in concrete. The inelastic fracture response due to the presence of fracture process zone may be taken into account by cohesive pressure acting on the crack faces. Fig.2.3 illustrates fracture process zone in brittle-ductile materials (Bažant, 2002).

Substantive nonlinear fracture models have been reported to capture essential behavior mechanisms in cracked concrete. Generally, two basic approaches have been followed.: first method uses the finite element method or the boundary element method such as the cohesive crack model (CCM) or the fictitious crack mode (FCM)

(Hillerborg *et al.*, 1976) and the crack band model (Bažant and Oh, 1983) in the smeared-cracking framework; second approach uses the modified LEFM concept such as two-parameter fracture model (TPFM) (Bazant and Kazemi, 1990; Jenq and Shah, 1985), size effect mode (SEM) (Bazant and Kazemi, 1990), effective crack model (ECM) (Karihaloo and Nallathambi, 1989), double-*K* fracture model (DKFM) and double-*G* fracture model (DGFM).

Based on different description of displacement field used, the numerical simulation of concrete fracture can be classified as the discrete crack model and the smeared crack model. In late 1967, Ngo and Scordelis (Ngo and Scordelis, 1967) introduced the discrete crack model to simulate concrete fracture. The model is aimed at stimulating the initiation and propagation of dominant cracks. A crack is introduced as a geometric entity. Initially, this was implemented by letting a crack grow when the nodal force at the node ahead of the crack tip exceeds a tensile strength criterion. Then, the node is split into two nodes and the tip of the crack is assumed to propagate to the next node. When the tensile strength criterion is violated at this node, it is split and the procedure is repeated (Borst *et al.*, 2004). Based on Barenblatthe (Barenblatt, 1962) and Dugdale's (Dugdale, 1960) works, a major advance in concrete fracture modelling was made by Hillerborg *et al* (Hillerborg et al., 1976) who included the tension softening process zone through a fictitious crack ahead the pre-existing crack. It is known that the cohesive crack model requires a unique stress-strain curve to quantify the value of energy dissipation and the choice of the curve significantly influences the prediction. Many different shapes of curves, including linear, bilinear, trilinear, exponential and power functions, have been reported in the literatures. However, the original discrete crack approach has several disadvantages. Cracks tend to form and propagate along the element boundaries, i.e. a mesh bias will appear. Automatic remeshing technique (Ingraffea and Saouma, 1984) allows the mesh bias to be reduced but will aggravate a computational difficulty, namely, the continuous change in topology. Advent of meshless methods, such as the element-free Galerkin

method (Belytschko *et al.*, 1994), alleviated the change in topology but lead to significant computational costs.

Rashid (Rashid, 1968) introduced smeared crack models which are based on the concept of replacing the crack by a continuous medium with altered physical properties .When the combination of stresses satisfies a specified criterion, a crack is initiated. The isotropic stress-strain relation at the integration point is replaced by an orthotropic elasticity-type relation with the direction normal to the crack and the direction tangential to the crack being axes of orthotropy. In early studies, both the normal stiffness and the shear stiffness across the crack were equal to zero upon cracking. Modification of the model was conducted by introducing strain softening and the shear retention factor. The first modification allows results that are physically more appealing and numerically more stable. The later modification enables representation of some effects of aggregate interlocking and friction within the crack. Bazant (Bažant and Oh, 1983) developed the crack band model in which the fracture process zone is modeled as a band of parallel cracks that are uniformly and continuously distributed in the finite element. The material behavior is characterized by the constitutive stress-strain relationship. The width of the fracture process zone is assumed to be constant in order to avoid spurious mesh sensitivity. This assures that the energy dissipation due to fracture per unit length of crack is equal to the fracture energy of the material. The major advantage of the smeared crack model is that the remeshing is not required. The disadvantages include spurious mesh sensitivity and convergence of the solution for decreasing mesh size which cannot be checked. In the smeared context, a method is known as the extended finite element method has been applied for cohesive zone modeling. This method use the partition-of-unity property to avoid the numerical difficulties associated with the smeared cohesive zone modeling (Meschke and Dumstorff, 2007; Wells and Sluys, 2001).

2.3 Hierarchical of concrete modelling

Wittmann (Wittmann, 1986) incorporated a multi-scale model into concrete study and introduced three structural levels to link crack formation and failure of a composite material such as concrete with structural features.

1. Macroscopic Level

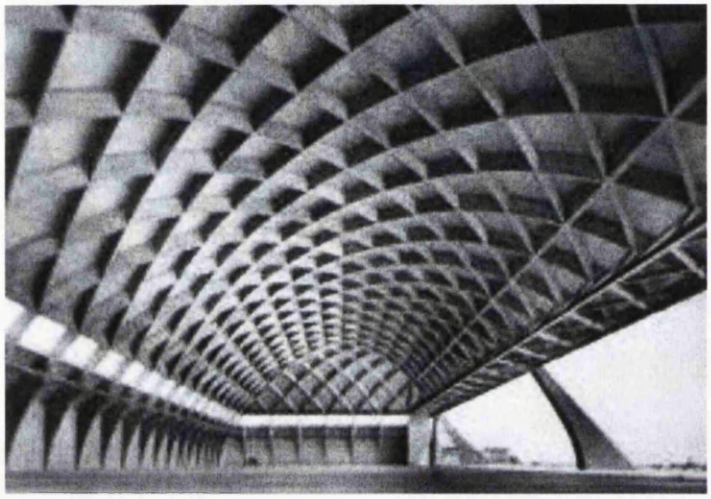

Figure 2.4: Concrete at macroscopic level.

At the macroscopic level (10^{-1}-10^{3}m), the characteristic size of concrete specimens and structures is much larger than the aggregate size, thus concrete can be assumed to be homogenous. Most concrete mechanics are based on this hypothesis. However, many experimental observations, such as the size effect, cannot be explained by such an assumption, permeability of concrete is much higher than cement mortar, and under fire loading, Young's modulus reduces more significantly than strength, etc.

2. Mesoscopic Level

At the mesoscopic level (10^{-4}-10^{-1}m), concrete is a three phased composite material consisting of mortar matrix, aggregate and interfacial transition zone. The interfacial transition zone is the weakest component. When loaded the microcracks often occur between aggregate and mortar first. Thus, the interfacial transition zone influence the overall performs of concrete significantly. This could well explain the fact that the

strength of concrete decreases with increasing aggregate size and the strength of concrete is smaller than aggregate strength and larger than mortar matrix strengths. In order to investigate the mechanical properties of interfacial transition zone, we have to go deeper into microscopic level

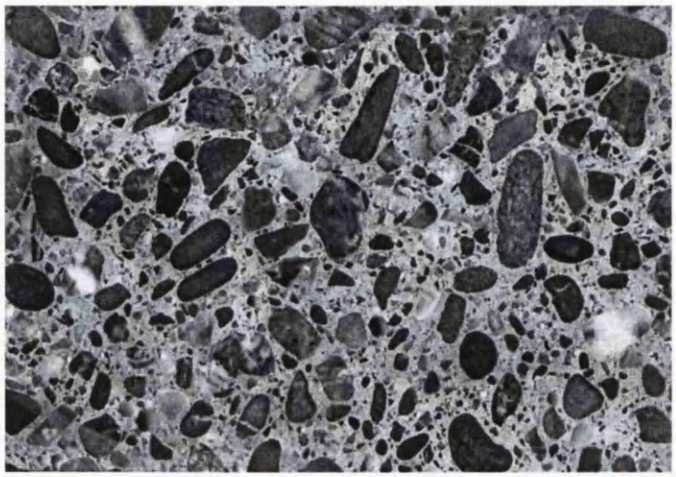

Figure 2.5: Concrete at mesoscopic level.

3. Microscopic Level

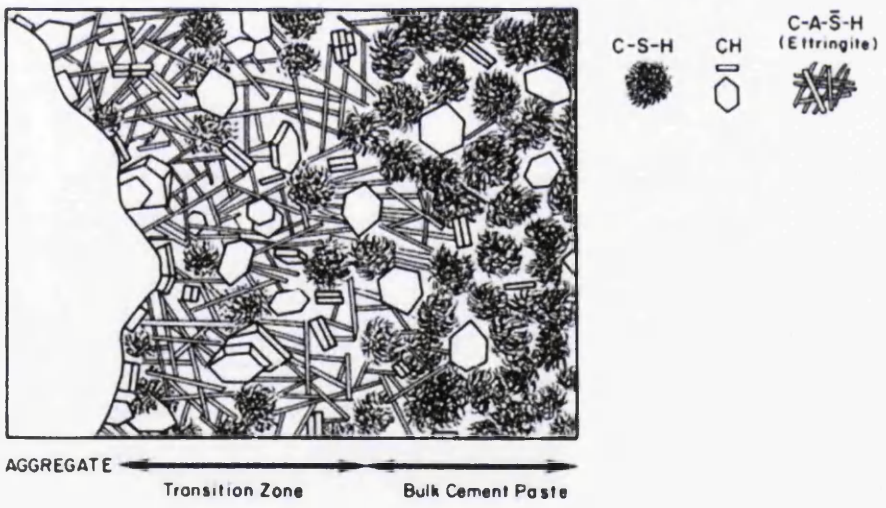

Figure 2.6: Interfacial transition zone and matrix at microscopic level (Mehta and Monteiro, 1993).

At the microscopic level (10^{-8}-10^{-4}m), concrete is heterogeneous where the paste is observed to be a mixture of different types of crystalline structures, at varying degrees of hydration, which form an amorphous gel. Loss of water to the hydration of cement

particles and evaporation, as well as entrained and entrapped air, cause voids to form in the heterogeneous mass and in particular the interface between aggregate and matrix. Maso (Maso *et al.*, 1995) suggests that the main reason of concrete strength is lower than mortar matrix due to the existence of these voids.

It has become clear that meso-scale level models are promising tools which can describe both qualitative and quantitative effects of independent mechanical properties of different material components on the global mechanical properties of the concrete material. The present project mainly focuses on the meso-scale level simulation of fracture behavior of the concrete.

2.4 Pre-process of meso-scale models

In order to capture the heterogeneous morphological features of concrete at meso-scale level, it is essential to introduce a preprocessor in the numerical modeling to reproduce the aggregate structure in which the shape, size and distribution of the aggregate particles resemble real concrete material. There may be two different methods to incorporate the aggregate structure. In the first method, the details about the structure can be measured and translated directly into a finite/discrete element mesh (Karihaloo *et al.*, 2003). Details about aggregate size distribution, interface geometry and so on are used directly. As a result distinct regions of varying stiffness and strength will be present in the mesh. In the other method, the structure information is translated into a statistical distribution that is subsequently used to assign strength and stiffness properties to different elements in a finite/discrete element mesh (Van Mier *et al.*, 2002). Although the second approach saves much computational effort, more realistic results are obtained by projecting directly the aggregate structure.

The aggregate structure can be either computer-generated or scanned from experimental specimen (Man and van Mier, 2011; Schlangen and Garboczi, 1997). Kim (Kim and Buttlar, 2009) developed a heterogeneous fracture model, based on the discrete element method, to investigate various fracture toughening mechanisms of asphalt concrete using image processing technique. The image processing technique

maps out the cross-sectional aggregate structure images of a typical material and then the digitized images were projected onto a two dimensional discrete element mesh (Figure 3.1). However, the image processing technique is limited by the requirement of experimental specimen sample. For this reason computer-generated approach is adopted in this research.

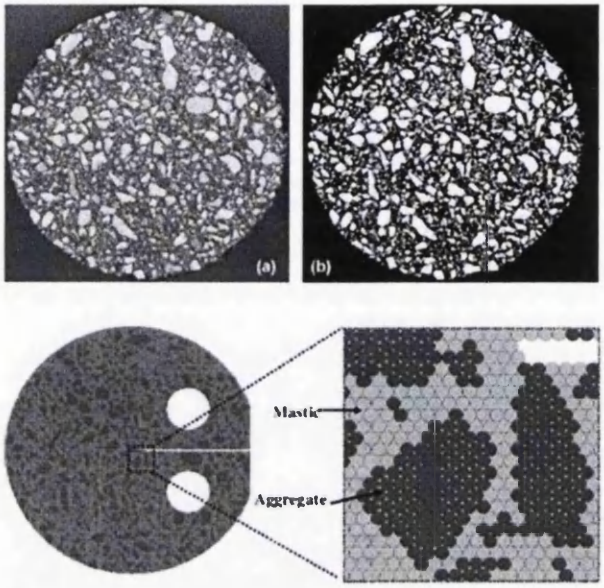

Figure 2.7: Digitized specimen images and DEM mesh (Kim and Buttlar, 2009).

In general a preprocessor consists of two stages:

- Generation of mesoscopic geometric model: the geometric model of aggregate structure can be either randomly generated by utilizing various random aggregate structure generators or scanned from experimental specimen by using image processing technique. Determination of shape and size of aggregates, aggregate content and grading will also be involved.
- Projection of three-phased geometric model onto element mesh: each element is assigned to its corresponding phase according to coordinates of the element. Then intrinsic mechanical properties are assigned for each element.

2.4.1 Single aggregate generators

In order to simulate the structure and components of the concrete material, a single

aggregate should be generated first. The first step towards aggregate generation is the determination of the shape of aggregate. Many single aggregate generators assumed that the aggregate particles are circular or spherical (Bažant *et al.*, 1990; Häfner *et al.*, 2006; Schalangen and J.G.M. van Mier, 1994; Schorn and Rode, 1991). Assuming that aggregate particles are circular or spherical is suitable for modeling gravel aggregates, simpler algorithms might be proposed. However, the obtained (artificial) material has more uniform consistence, and underestimates natural phenomenon such as clustering of particles (Yang and Xiang, 2012).

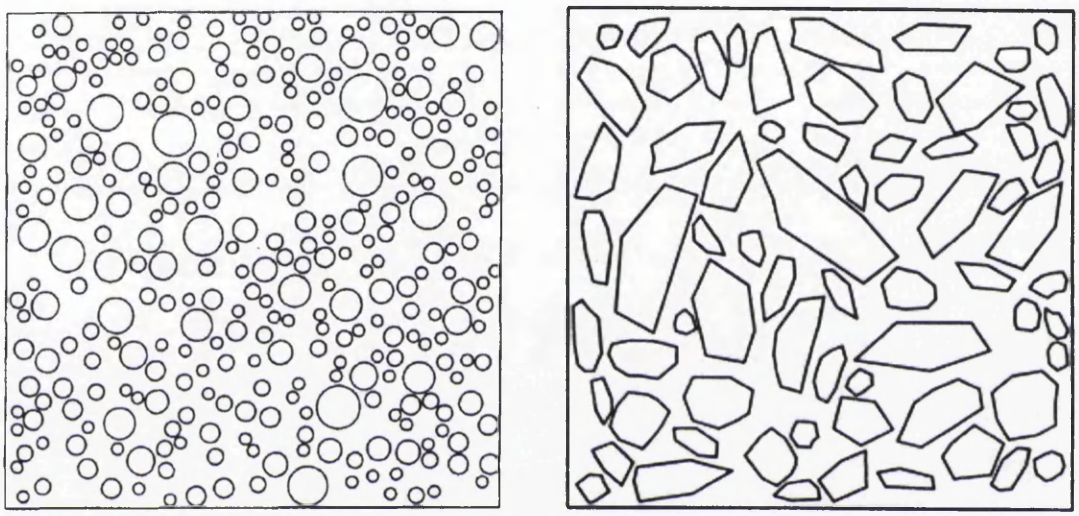

(a) Circular aggregate structure (Schalangen and Mier,1994)

(b) Polygonal aggregate structure (Wang *et al, 1999*)

Figure 2.8 Random aggregate structure model

In order to represent crushed rock aggregates which generally appear in angular and convex shape, more sophisticated random aggregate generators are required. By using the morphological law developed by Beddow and Meloy (Beddow and Meloy, 1980) Wittmann (Wittmann *et al.*, 1985b) have generated rounded aggregates as polygons each having the number of edges and the corresponding angles randomly chosen. One of the most generally applicable techniques to generate two dimensional random aggregate structure was developed by Wang (Wang *et al.*, 1999). In their research a procedure for generating random aggregate structures for rounded and angular

aggregates based on the Monte Carlo random sampling principle was proposed. Rounded aggregates were generated with shapes following Beddow and Meloy's morphological law while angular aggregates were generated as polygons with prescribed elongation ratios.

2.4.2 Aggregate disposition procedure and overlap detection algorithm

In order to reproduce the aggregate structure of a particular specimen, the aggregate disposition procedure must satisfy the following requirements:

- Randomness of the aggregate distribution
- Reasonable aggregate grading
- Compatible and sufficiently high aggregate content

Based on these requirements of size and spatial distributions various algorithms and models have been developed. Many researchers (Bažant *et al.*, 1990; Schalangen and J.G.M. van Mier, 1994; Wang *et al.*, 1999) adopted the so called take-and-place method in which the aggregates were placed one by one. The aggregates with prescribed size and shape were generated and stored by aggregate generation procedure first. Then at the start of aggregate allocation procedure, one aggregate was restored from the database and placed into 2D or 3D Euclidian space randomly, if overlaps are detected then the aggregate will be replaced to a new position until no overlap can be found. This take-and-place loop continues until the generation is completed. Leite (Leite *et al.*, 2004) proposed a stochastic-heuristic algorithm which is capable of generating a high aggregate content and realistic distributed aggregate structure in 3D space. Two dimensional analyses can be conducted by slicing from 3D specimen. The allocation procedure starting with the largest aggregate and after each successful allocation the aggregate position is fixed and settled.

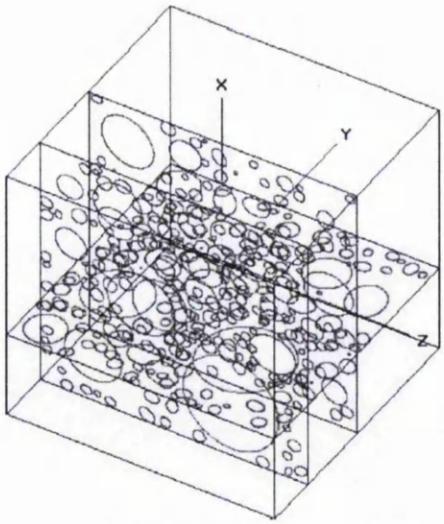

Figure 2.9 Idealised slice cut-outs from a 3D specimen for 2D analyses (Leite *et al.*, 2004)

Alternatively a random aggregate drop method can be adopted (Tang *et al.*, 2009; Vervuurt, 1997). The random generated aggregates were dropped into the prescribed space and settled at the deepest position one by one. Tang (Tang *et al.*, 2009) improved the effectiveness of previous algorithm using a layering disposition method. Each aggregate is packed into its external tangent rectangular box and the length and height of each box is recorded. Then the numbered boxes are dropped into the space layer by layer.

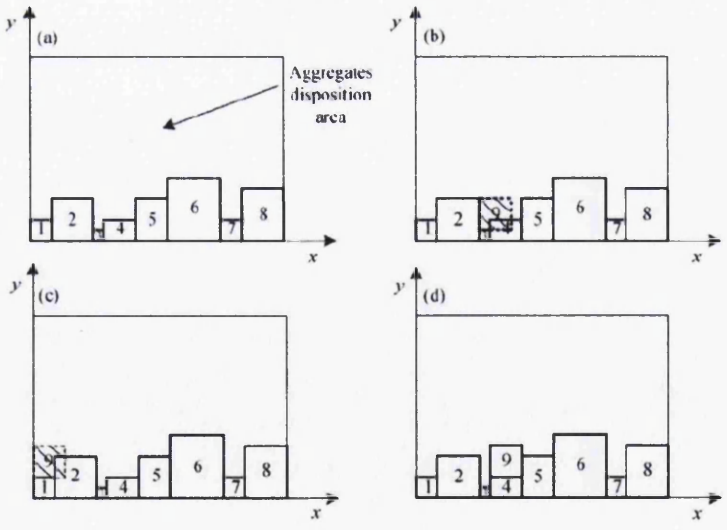

Figure 2.10 Layering disposition method (Tang *et al.*, 2009)

Other algorithms such as the divide-and-fill method bases on Delaunay triangulation (De Schutter and Taerwe, 1993) are also available. The benefit of this particular divide-and-fill algorithm is that a good representation of aggregate structure can be obtained quickly with low computational cost because no overlaps searching process is required. The disadvantage is the aggregate grading and distribution can be hardly controlled.

2.5 Numerical methods for meso-scale modelling of concrete fracture

The most commonly applied numerical methods for concrete problems are:

(1) Continuous methods: Finite Different Method (FDM), Finite Element Method (FEM) and Boundary Element Method(BEM)

(2) Discontinuous methods: Discrete Element Method (DEM), Discrete Fracture Network (DFN) methods.

(3) Hybrid continuous/discontinuous methods: Hybrid FEM/BEM, Hybrid FEM/DEM.

The FEM is a mainstream numerical tool in engineering sciences due to its flexibility in handling material inhomogeneity and anisotropy, complex boundary conditions and moderate efficiency in dealing with complex constitutive models and fracture. The FDM is easy to implement and it has been proved to be effective to simulate crack propagation when the geometry shape is simple. The BEM method is considered the best tool for simulating fracturing process in solids by many researchers and engineers. The BEM's advantage of smaller computer memory and block-like matrix structure when the multi-region technique is used makes it more suitable for solving large-scale problems with reduced degrees of freedom (Jing, 2003).

The discrete element method DEM was initially applied for the analysis of discontinuous media, e.g. rock mechanics and soil mechanics. Recently the DEM has been used in the fracture studies of continuous media, for example concrete. The most significant advantage over the traditional continuum approach is the way that DEM discretises a material domain, as dynamic material behaviour of composites, crack tip singularities and crack formulation criteria can all be avoided due to the naturally discontinuous representation of concrete materials via particle assemblies (Fakhimi and Villegas, 2006).

One of the current limitations of particle based methods for fracture analysis is related with the high number of particles required for larger structures. To overcome such limitation Azevedo proposed a hybrid discrete element/finite element method for fracture analysis of plain concrete. (Azevedo and Lemos, 2006). The coupling between the two different discretization is done by introducing interface elements with shear and normal spring in the boundaries between the two different discretization. When compared to a pure DEM model, the hybrid model allows significant computer savings. The model gives good results in terms of crack patterns, crack localization process and pre-peak load displacement relationship for both mode I and mixed mode fracture beam experiments. However, further work is still required in order for the particle model to display a more ductile post-peak response.

By combining different numerical methods with meso-scale modelling concepts, many different types of meso-scale models have been developed to model the failure process and the global mechanical properties of concrete in the past. The random particle model developed by Bazant (Bažant *et al.*, 1990), UDEC presented by Vonk et al., micromechanical model proposed by Mohamed and Hansen(Mohamed and Hansen, 1999a, b), the lattice mode, the random aggregate structure (RAS) and the fracture-based interfacial elements approach are all typical mesoscopic models that can simulate the damage process and the deformation of concrete.

Lattice model

Lattice model is a typical meso-scale model based on theoretical physics. The main concept of the lattice model is that the medium consists of a mesh of regular or irregular beam elements. Then the mesh is projected onto random aggregate structure. If two nodes of a beam element are within aggregate or matrix phase, then aggregate or matrix properties is assigned to the element, the rest of elements are defined as interfacial trisection zone elements. Stiffness and strength of the beams may have local variations and be generated randomly for representing statistical inhomogeneity of the medium. Fracture processes are reproduced by sequential removal of elements from the mesh and it is assumed that such elements have linear-elastic behaviour until failure. At each step, the element to be removed is that with maximum value of the ratio between the effective stress and the tensile strength (Lilliu and van Mier, 2003).

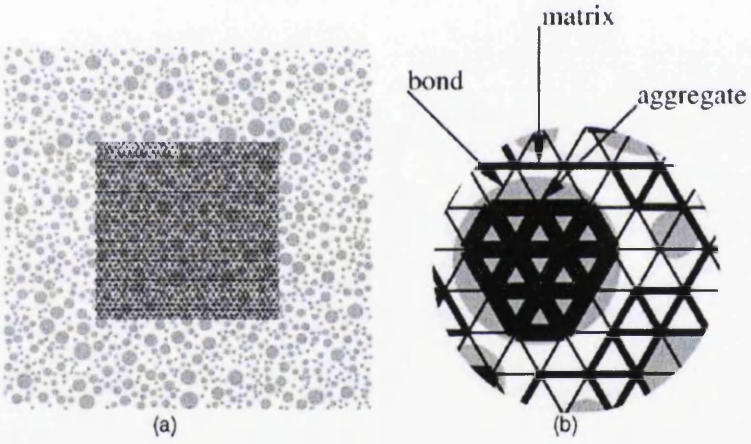

Figure 2.11:Overlaying the lattice mesh on top of computer-generated aggregate structure. (Lilliu and van Mier, 2003)

Such type of material modelling has already been used in the 1940s for simulating problems of elasticity. More recently it has been introduced in the field of statistical physics for studying fracture of disorder materials (Herrmann *et al.*, 1989).

Schlangen (Schlangen and van Mier, 1992) incorporated both statistic model and aggregate structure model into lattice model to simulate the typical failure mechanism, crack face bridging, in concrete. Input parameters for the beam elements are proved to

be important in the approach with the aggregate structure. The exact value of these input parameters should be determined from a parameter study and comparison with experimental measurements.

Schlangen (Schlangen and Garboczi, 1997) performed a study on the effect of lattice element type and lattice orientation on the fracture pattern by simulating a shear loading experiment. The effect of element resolution on fracture results was also investigated. Heterogeneity in the model was implemented by using digital images of the real aggregate structure of concrete material. A new fracture law base on the maximum tensile stress in each node has been developed. It has been found that crack pattern strongly influenced by element type, elements with three degrees of freedom per node gave the best agreement with experimentally observations. The orientation of beams also influenced the crack patterns, as cracks tending to follow the mesh lines. Further work is still required such as how to determine the input parameters such as stiffness and strength, in particular the for the interfacial zone element.

Lilliu (Lilliu and van Mier, 2007) performed 2D and 3D simulations to investigate the sensitivity of three-phase concrete to variations in the aggregate content and the thickness of the interfacial transition zone. It has been found that 2D and 3D analyses give qualitatively the same result. The extreme brittleness of the 2D analysis disappeared in 3D model.

To overcome extremely large computational effort, Liu (Liu *et al.*, 2007) proposed the generalized beam lattice in which aggregate is modeled by one single node rather than 10-100 nodes in beam lattice model by proposal of two-node and three-phase elements. The numerical results indicate that the model can reproduce the fracture process well and also reduce the computational effort significantly.

Sagar (Vidya Sagar *et al.*, 2010) verified the lattice model by AE study of concrete in the three-point bend test. The model was attempted to reduce the simulation time by using a regular triangular lattice network only over the expected fracture process zone

width and the rest of the beam specimen was discretized by a coarse triangular mesh. Reasonable load-deformation diagrams and cumulative number of fracture were reproduced.

Man (Man and van Mier, 2011) utilized 3D lattice model to study size effect in numerical concrete. A realistic aggregate structure was obtained from CT-scans of real concrete and overlaying these images with a 3-dimensional hcp-lattice. A large number of microcracks and just a few large cracks were observed at peak load. One of the larger cracks grew when loading was continued in the softening regime and no further microcracks developed.

Micromechanical model

Mohamed and Hansen (Mohamed and Hansen, 1999a, b) proposed a micromechanical model utilizes the finite element method as a numerical tool where the truss element is used as the basic element in the finite element mesh.. Randomness of the aggregate phase and the probabilistic nature of the properties of the three phases are considered. The constitutive relations of the elements are described according to the smeared cracking concept that is based on the fictitious crack model. The model considers tensile cracking as the only fracture criterion at the microlevel. Thus, it is capable to reproduce good predictions for tensile failure dominated problems.

Further development of M-H model was conducted by Tang and his colleagues (Zhu *et al.*, 2005; Zhu *et al.*, 2004a, b). The constitutive law of each phase is defined on the basis of elastic damage mechanics, and the maximum tensile strain criterion and the Mohr-Coulomb criterion are adopted as damage thresholds. A simple method analogous to the smeared crack method is used for tracing the crack propagation process and for capturing the interaction of multiple cracks. This model predicted well the fracture process of concrete when subjected to tensile, shear and uniaxial and biaxial compression load.

Particle model

Bazant et al. (Bažant *et al.*, 1990) proposed a particle model for brittle aggregate materials such as concretes. The material domain is discretized as a randomly distributed circular particle system. The particles are assumed to be elastic and have only axial interaction as in a truss. The interparticle contact layers of the matrix are described by a softening stress-strain relation. Fracture process of concrete and the size effect are investigated by performing three-point bending test and uniaxial tensile test.

Zhong et al. (Zhong and Chang, 1999) modified the random model by considering the interparticle contact layers with microcracks and these microcracks will grow when loaded. The fracture criterion can be expressed in terms of stress intensity factors. Other model input parameters, including elastic contacts and geometric parameters, first mode and second mode fracture toughnesses, interfacial friction angle, crack-interfacial cohesion, must be well defined in order to obtain accurate results.

Fracture of quasi-brittle materials, which is characterized by large zones of distributed cracking, can be effectively modeled by a particle system with braking bonds. Mechanical analysis of large systems of particles was initiated by Cundall (Cundall, 1971) to simulate the behavior of granular solids by rigid particles. This approach was developed and extensively applied by Cundall and Stack (Cundall and Strack, 1979). 2D disk code *Ball* and 3D sphere code *Trubal* have been developed which were prototypes of commercial software PFC2D and PFC3D (Itasca, 1999).

In particle flow code, medium is treated as an assembly of rigid discs or spheres. The movement of particles obeys Newton's law of motion while the interaction of the particles is defined through contact models. The elastic response of the contact is described by a linear contact law or Hertz-Mindlin contact model. The inelastic response of the contact is described through a slip model and a bond model. The conventional DE method does not consider the tensile resistance. Introduction of bond

model enables one to simulate cohesive-frictional materials such as concrete and rocks. The bond can be visualized as a set of springs with normal and shear stiffnesses and allows the transfer of both force and moments through the contacts. The fracture process is naturally captured by meanings of bond breakages when bond strength or energy is exceeded. Because of the naturally discontinuous representation of the material, problems such as the dynamic behaviour of material at meso-scale, crack tip singularities, crack formulation criterions can all be avoided. A brief review of particle flow code will be presented in the next chapter.

2.6 Parameter study of particle flow code

The particle approach contains several micro-properties such as normal and shear stiffness of particles and bonds, size of particles, tensile and shears strength of bond etc. Unlike the continuum approach, such as FEM, input parameters for the discrete particle assembly are unknown in advance. Not all of these parameters are directly linked to measurable physical material properties, but have a significant impact on the macroscopic behaviour of particle system. The relationship between the microscopic particle and bond properties and the macroscopic properties must be well understood before one can try to effectively control the behavior of the model and tune it up to match the real behavior of the material so that practical problems can be solved.

Two distinct approaches are proposed followed for the determination of micro-properties.

Direct analysis, where the micro-parameters are determined a set of specific simplified models prior to simulating the target application.

Back analysis, where the parameters by evaluated by solving the target simulation iteratively and optimising the micro-parameters to provide the best fit.

Direct analysis is obviously an attractive procedure simply because once the relation is determined, the target application can be solved without interactive correction of the micro-parameters. Griffiths and Mustoe (Griffiths and Mustoe, 2001) proposed the direct analysis for contact bond model to evaluate the bond stiffness. They utilise a representative unit cell consisting of bonded particles and determine the bond parameters equivalent to the macroscopic Young's modulus and Poisson's ratio by ensuring that the strain energy of the representative unit closely approximates that of the equivalent elastic continuum body. Based on strain energy and two-dimensional Hooke's law the relationship between elastic constants and stiffness in hexagonal arrangement have been obtained by Sawamoto (Sawamoto *et al.*, 1998), Tavarez and Plesha (Tavarez and Plesha, 2007) and Kim (Kim *et al.*, 2008). Both methods reached to the same solution and showed their effectiveness for evaluating equivalent micro-properties for characterisation of elastic response. However, above direct analysis assume regularly aligned particles with uniform radius. Consequently, the evaluated micro-properties may not be appropriate when the assembly consists of randomly distributed particles with various particle sizes.

The correlations of the micro-parameters to the macroscopic response of material have been extensively studied. Huang (Huang, 1999) obtained some scaling laws for an irregular disc assembly with a contact bond model by using dimensional analysis and numerical uniaxial and biaxial tests. Potyondy and Cundall (Potyondy and Cundall, 2004) proposed a parallel bond model and performed parameter study. Yang et al.(Yang *et al.*, 2006) investigated the relationships of between microparameters and macroproperties for parallel bond model using PFC2D. Dimensional analysis was adopted to obtain theoretical formulations while numerical simulations of uniaxial compression test were conducted to quantify the relationships. Fakhimi and Vilegas (Fakhimi and Villegas, 2006) employed dimensional analysis to establish a fast and efficient tool for calibration of a so-called slightly overlapped circular particle interaction model. Koyama and Jing (Koyama and Jing, 2007) proposed a numerical

procedure to determine the equivalent micro-mechanical properties of intact rocks using a stochastic representative elementary volume (REV) concept. The investigation is performed base on numerical simulation of uniaxial compression tests on parallel-boned PFC2D materials. Yoon (Yoon, 2007) developed a new approach for calibrating contact-bonded model using 'experimental design' and 'optimization' in uniaxial compression simulation. Sensitivities of micro-parameters with respect to material properties were tested by the Plackett-Burman design method. Wang and Tonon (Wang and Tonon, 2010) developed algorithms to calibrate model micro-parameters by utilizing their own DEM code. Deformability parameters were identified through parameter sensitivity analysis while strength parameters were identified by a global optimization process. The main findings are summaries as following:

Bond Stiffness

The elastic constants are affected by the bond or contact stiffness and the ratio of normal to shear stiffness. Yang et al. (Yang *et al.*, 2006) use uniaxial compression test simulations to observe the effect of the bond stiffness of parallel-bonded model on the macroscopic elastic constants such as Young's modulus (E) and Poisson's ratio (ν). The macroscopic Young's modulus is calculated by dividing stress at the start point to mid-point of the axial stress-strain curve by the corresponding strain. Using the same increment and assuming plane stress conditions, the Poisson's ratio is defined by: $\nu' = -\Delta\varepsilon_x / \Delta\varepsilon_y$. To reduce the number micro-parameters, grain stiffnesses are set equal to bond stiffnesses. By envisioning the bond at each contact as an elastic beam with its ends at the particle centres Potyondy and Cundall (Potyondy and Cundall, 2004) suggested that the grain and bond modulus are related to the corresponding normal stiffnesses. Based on several numerical tests they found: The macroscopic Young's modulus of specimen subjected to uniaxial compression is linearly proportional to a particle contact modulus. The Young's modulus is also affected by the stiffness ratio. In

terms of Poisson's ratio, Huang (Huang, 1999), Potyondy and Cundall (2004), (Fakhimi and Villegas, 2006), Yang et al. (2006), and Cho et al. (2007) showed the bond stiffness ratio link strongly with the equivalent macroscopic Poisson's effect. As the stiffness ratio is increased, the macroscopic Poisson's ratio also increases.

Inter-particle Friction

According to Huang (Huang, 1999) and Yang et al. (Yang *et al.*, 2006), peak compressive strength in uniaxial compression of particle assemblies is only slightly affected by the inter-particle friction coefficient. Wang and Mora (2008) also derived the same conclusion from uniaxial compression simulations with a pre-existing crack. Huang (Huang, 1999) concluded that the macroscopic residual strength is only slightly related to the inter-particle friction coefficient. They suggest instead that the residual strength can be linked to force anisotropies and the slip surface evolution. Cho et al. (Cho *et al.*, 2007) also investigate the effect of inter-particle friction coefficient and arrived at the conclusion that the friction coefficient only slightly affects dilation and has no effect to the macroscopic tensile strength to compressive strength ratio.

Bond Strength

Potyondy and Cundall (2004) suggest setting the same value for both bond normal and shear strength in order to include both micro-tensile and micro-shear failure mechanisms. They show that including both micro-failure mechanisms leads to more sophisticated damage evolution adjacent to a circular hole than the case excluding micro-shear failure.

Huang (Huang, 1999) investigated the influence of bond normal and shear strength by simulation of uniaxial compression tests of granular assemblies with different ratios of bond shear strength to normal strength. They conclude that a low ratio of shear strength to normal strength (less than 2) results in unrealistic response. Yang et al. (Yang *et al.*, 2006) also suggest the same threshold for the bond strength ratio, noting that when the

ratio larger than 2, the compressive strength is mainly determined by bond normal strength, otherwise bond shear strength is dominant.

Cho et al. (Cho *et al.*, 2007) conducted uniaxial compression test and Brazilian test simulations and found that the ratio of tensile to uniaxial compression strength of the predicted macroscopic behaviour is not influenced by the bond strength ratio. This discrepancy may come from the micromechanics modelling between parallel bond and contact bond models. Two factors are important;

1) Moment resistance system: moment resistance between particles is included in parallel bond model while the contact model does not provide moment resistance, especially in 2D case, since there are no contributions of moment to the tangential direction in 2D case. The additional moment resistance of the parallel model reduces the macroscopic displacement required to reach the normal strength than the contact bond model

2) Slip mechanism: in PB model grain friction or slip are independent from the bond behaviour, hence the model can consider the frictional force separately. In contrast, CB model does not allow friction before bond breakage occurs. Thus the friction effect in PB model increases the shear resistance relative to the CB model and may also prevent the microshear failure.

Degree of discretization effect

In number of literatures (Fakhimi and Villegas, 2006; Huang, 1999; Potyondy and Cundall, 2004; Yang *et al.*, 2006) the ratio L/R was considered as a measure of the degree of discretization, where L is the characteristic length of the discrete medium and R is the average particle size. According to Potyondy and Cundall (Potyondy *et al.*, 2002; Potyondy and Cundall, 2004), Young's modulus and Poisson's ratio appear to be independent of particle size as long as L/R ratio is large enough. Yang et al. (Yang *et al.*, 2006) conclude the critical limits for the size independence to valid is 130. Huang

(Huang, 1999) omit the effect of particle size on the elastic contacts. In terms of the effect on the macroscopic strength, there are no significant contributions to the uniaxial compressive strength due to particle size variation, while particle size has a major effect on the tensile strength. Since the macroscopic fracture toughness is proportional to Brazilian tensile strength, fracture toughness is also dependent on the particle size. Koyama and Jing (Koyama and Jing, 2007) scrutinized the particle size effect utilizing a stochastic representative elementary volume (REV) of particle assemblies in a statistical manner. According to their research, there are certain thresholds of both particle size and particle size distribution that are material dependent, hence care should be paid to determine a suitable particle size and its distribution. Results indicate that the variance of the calculated mechanical properties decrease significantly as the degree of discretization increase. The calculated macromechanical properties from random samples can be fitted to normal distribution curves approximately.

2.7 Findings

It has been noticed through the literature review that many numerical models can describe the mechanical behavior of concrete with acceptable accuracy. Particle based approach seems to be a attractive options to simulate the fracture behavior of concrete because of its simplicity and naturally discontinuous representation of the material.

In order to capture the heterogeneous morphological features of concrete at meso-scale level directly, it is essential to incorporate a random aggregate structure generation algorithm in the DEM code to reproduce the aggregate structure in real concrete material. Since the thickness of the interfacial transition zone (ITZ) is very small, the ITZ will be treated as particle contacts between aggregate particles and mortar particles in this study.

It has also been noticed that most of DEM parameter studies are based on

two-dimensional analyses to match deformability and strength rock material. Although it can be argued that the fracture behavior of rock and concrete are very similar, there is a big difference in terms of the range of Young's modulus and strength of these two materials. A comprehensive parameter study including dynamic effects will be performed in order to gain a better understanding of the calibration of particle flow model.

References

Azevedo, N.M., Lemos, J., 2006. Hybrid discrete element/finite element method for fracture analysis. Computer methods in applied mechanics and engineering 195, 4579-4593.

Barenblatt, G., 1962. The mathematical theory of equilibrium cracks in brittle fracture. Advances in applied mechanics 7, 104.

Barsoum, R.S., 1976. On the use of isoparametric finite elements in linear fracture mechanics. International Journal for Numerical Methods in Engineering 10, 25-37.

Bažant, Z., Tabbara, M., Kazemi, M., Pijaudier - Cabot, G., 1990. Random particle model for fracture of aggregate or fiber composites. Journal of engineering mechanics 116, 1686–1705.

Bažant, Z.P., 2002. Concrete fracture models: testing and practice. Engineering Fracture Mechanics 69, 165-205.

Bazant, Z.P., Kazemi, M.T., 1990. Determination of fracture energy, process zone longth and brittleness number from size effect, with application to rock and conerete. International journal of fracture 44, 111-131.

Bažant, Z.P., Oh, B.H., 1983. Crack band theory for fracture of concrete. Matériaux et construction 16, 155-177.

Beddow, J.K., Meloy, T., 1980. Testing and characterization of powders and fine particles, London: Heyden.

Belytschko, T., Lu, Y.Y., Gu, L., 1994. Element - free Galerkin methods. International Journal for Numerical Methods in Engineering 37, 229-256.

Borst, R.d., Remmers, J.J., Needleman, A., Abellan, M.A., 2004. Discrete vs smeared crack models for concrete fracture: bridging the gap. International Journal for Numerical and Analytical Methods in Geomechanics 28, 583-607.

Cho, N., Martin, C., Sego, D., 2007. A clumped particle model for rock. International Journal of Rock Mechanics and Mining Sciences 44, 997-1010.

Cundall, P.A., 1971. A Computer Model for Simulating Progressive Large Scale Movements in Blocky Rock Systems, Proceedings of the Symposium of the International Society of Rock Mechanics, Nancy, France, pp. Paper No. II-8.

Cundall, P.A., Strack, O.D.L., 1979. A discrete numerical model for granualar assemblies. Geotechnique 29, 47-56.

de Borst, R., 2002. Fracture in quasi-brittle materials: a review of continuum damage-based approaches. Engineering Fracture Mechanics 69, 95-112.

De Schutter, G., Taerwe, L., 1993. Random particle model for concrete based on Delaunay triangulation. Materials and structures 26, 67-73.

Dugdale, D., 1960. Yielding of steel sheets containing slits. Journal of the Mechanics and Physics of Solids 8, 100-104.

Fakhimi, A., Villegas, T., 2006. Application of Dimensional Analysis in Calibration of a Discrete Element Model for Rock Deformation and Fracture. Rock Mechanics and Rock Engineering 40, 193-211.

Griffith, A.A., 1921. The phenomena of rupture and flow in solids. Philosophical transactions of the royal society of london. Series A, containing papers of a mathematical or physical character 221, 163-198.

Griffiths, D.V., Mustoe, G.G.W., 2001. <Modelling of elastic continua using a grillage of.pdf>. International Journal for Numerical Methods in Engineering 50, 1759-1775.

Häfner, S., Eckardt, S., Luther, T., Könke, C., 2006. Mesoscale modeling of concrete: Geometry and numerics. Computers & Structures 84, 450-461.

Herrmann, H.J., Hansen, A., Roux, S., 1989. Fracture of disordered, elastic lattices in two dimensions. Physical Review B 39, 637-648.

Hillerborg, A., Modéer, M., Petersson, P.-E., 1976. Analysis of crack formation and crack growth in concrete by means of fracture mechanics and finite elements. Cement and concrete research 6, 773-781.

Huang, H.Y., 1999. Discrete element modeling of tool-rock interaction. American: University of Minnesota.

Ingraffea, A., Saouma, V., 1984. Numerical modeling of discrete crack propagation in reinforced and plain concrete, Fracture Mechanics of Concrete: structural application and numerical calculation. Springer, pp. 171-225.

Ingraffea, A.R., Gerstk, W.H., Gergely, P., Saouma, V., 1984. Fracture mechanics of bond in reinforced concrete. Journal of Structural Engineering 110, 871-890.

Ingraffea, A.R., Manu, C., 1980. Stress - intensity factor computation in three dimensions with quarter - point elements. International Journal for Numerical Methods in Engineering 15, 1427-1445.

Irwin, G.R., 1957. Analysis of stresses and strains near the end of a crack traversing a plate. J. Applied Mechanics 24, 351-369.

Jenq, Y., Shah, S.P., 1985. Two parameter fracture model for concrete. Journal of engineering mechanics 111, 1227-1241.

Jing, L., 2003. A review of techniques, advances and outstanding issues in numerical modelling for rock mechanics and rock engineering. International Journal of Rock Mechanics and Mining Sciences 40, 283-353.

Kaplan, M., 1961. Crack propagation and the fracture of concrete, ACI Journal Proceedings. ACI.

Karihaloo, B., Nallathambi, P., 1989. An improved effective crack model for the determination of fracture toughness of concrete. Cement and concrete research 19, 603-610.

Karihaloo, B., Shao, P., Xiao, Q., 2003. Lattice modelling of the failure of particle composites. Engineering Fracture Mechanics 70, 2385-2406.

Kim, H., Buttlar, W.G., 2009. Discrete fracture modeling of asphalt concrete. International journal of solids and structures 46, 2593-2604.

Kim, H., Wagoner, M., Buttlar, W., 2008. Simulation of Fracture Behavior in Asphalt Concrete Using a Heterogeneous Cohesive Zone Discrete Element Model. Journal of materials in civil engineering 20, 552-563.

Koyama, T., Jing, L., 2007. Effects of model scale and particle size on micro-mechanical properties and failure processes of rocks—A particle mechanics approach. Engineering Analysis with Boundary Elements 31, 458-472.

Leite, J.P.B., Slowik, V., Mihashi, H., 2004. Computer simulation of fracture processes of concrete using mesolevel models of lattice structures. Cement and concrete research 34, 1025-1033.

Lilliu, G., van Mier, J.G.M., 2003. 3D lattice type fracturemodel for concrete. Engineering Fracture Mechanics 70, 927–941.

Lilliu, G., van Mier, J.G.M., 2007. On the relative use of micro-mechanical lattice analysis of 3-phase particle composites. Engineering Fracture Mechanics 74, 1174-1189.

Liu, J.X., Deng, S.C., Zhang, J., Liang, N.G., 2007. Lattice type of fracture model for concrete. Theoretical and Applied Fracture Mechanics 48, 269-284.

Man, H.K., van Mier, J.G.M., 2011. Damage distribution and size effect in numerical concrete from lattice analyses. Cement and Concrete Composites 33, 867-880.

Maso, J.C., Ollivier, J.P., Bourdette, B., 1995. Interfacial transition zone in concrete. Advanced Cement Based Materials 2, 30-38.

Mehta, P.K., Monteiro, P., 1993. Durability. PK Mehta. Concrete, microstructure, properties and materials. Westerville: JP Skalny (Ed), 113-155.

Meschke, G., Dumstorff, P., 2007. Energy-based modeling of cohesive and cohesionless cracks via X-FEM. Computer methods in applied mechanics and engineering 196, 2338-2357.

Mindess, S., 1991. The Fracture Process Zone in Concrete, In: Shah, S.P. (Ed.), Toughening Mechanisms in Quasi-Brittle Materials. Springer Netherlands, pp. 271-286.

Mohamed, A.R., Hansen, W., 1999a. Micromechanical Modeling of Concrete Response under Static Loading—Part 1: Model Development and Validation. Materials Journal 96, 196-203.

Mohamed, A.R., Hansen, W., 1999b. Micromechanical modeling of concrete response under static loading: Part II - Model predictions for shear and compressive loading. ACI Materials Journal 96, 354-358.

Neville, A.M., 1995. Properties of concrete.

Ngo, D., Scordelis, A., 1967. Finite element analysis of reinforced concrete beams, ACI Journal Proceedings. ACI.

Ortiz, M., 1988. Microcrack coalescence and macroscopic crack growth initiation in brittle solids. International journal of solids and structures 24, 231-250.

PFC2D, 1999. Particle flow code in 2 dimensions. Itasca Consulting Group, Inc.

PFC3D, 1999. Particle flow code in 3 dimensions. Itasca Consulting Group, Inc.

Potyondy, D., Cundall, P., Generation, O.P., 2002. The PFC model for rock: Predicting rock-mass damage at the underground research laboratory. Ontario Power Generation, Nuclear Waste Management Division.

Potyondy, D.O., Cundall, P.A., 2004. A bonded-particle model for rock. International Journal of Rock Mechanics and Mining Sciences 41, 1329-1364.

Rashid, Y., 1968. Ultimate strength analysis of prestressed concrete pressure vessels. Nuclear Engineering and Design 7, 334-344.

Sawamoto, Y., Tsubota, H., Kasai, Y., Koshika, N., Morikawa, H., 1998. Analytical studies on local damage to reinforced concrete structures under impact loading by discrete element method. Nuclear Engineering and Design 179, 157-177.

Schalangen, E., J.G.M. van Mier, 1994. Simple lattice model for numerical simulation of fracture of concrete materials and structures. Materials and structures 25, 534-542.

Schlangen, E., Garboczi, E., 1997. Fracture simulations of concrete using lattice models: computational aspects. Engineering Fracture Mechanics 57, 319-332.

Schlangen, E., van Mier, J.G.M., 1992. Experimental and numerical analysis of micromechanisms of fracture of cement-based composites. Cement and Concrete Composites 14, 105-118.

Schorn, H., Rode, U., 1991. Numericalsimulation of crackpropagation from microcracking to fracture. Cement and Concrete Composites 13, 87-94.

Shah, S.P., McGarry, F.J., 1971. Griffith fracture criterion and concrete. Journal of the Engineering Mechanics Division 97, 1663-1676.

Shih, C., Lorenzi, H., German, M., 1976. Crack extension modeling with singular quadratic isoparametric elements. International journal of fracture 12, 647-651.

Tang, X., Zhang, C., Shi, J., 2009. A multiphase mesostructure mechanics approach to the study of the fracture-damage behavior of concrete. Science in China Series E: Technological Sciences 51, 8-24.

Tavarez, F.A., Plesha, M.E., 2007. Discrete element method for modelling solid and particulate materials. International Journal for Numerical Methods in Engineering 70, 379-404.

Van Mier, J.G., van Vliet, M.R., Wang, T.K., 2002. Fracture mechanisms in particle composites: statistical aspects in lattice type analysis. Mechanics of Materials 34, 705-724.

Vervuurt, A., 1997. Interface fracture in Concrete. TU Delft.

Vidya Sagar, R., Raghu Prasad, B., Karihaloo, B., 2010. Verification of the applicability of lattice model to concrete fracture by AE study. International journal of fracture 161, 121-129.

Wang, Y., Tonon, F., 2010. Calibration of a discrete element model for intact rock up to its peak strength. International Journal for Numerical and Analytical Methods in Geomechanics 34, 447-469.

Wang, Z.M., Kwan, A.K.H., Chan, H.C., 1999. Mesoscopic study of concrete I: generation of randomaggregate structure and finite element mesh. Computers & Structures 70, 533-544.

Wells, G., Sluys, L., 2001. A new method for modelling cohesive cracks using finite elements. International Journal for Numerical Methods in Engineering 50, 2667-2682.

Wittmann, F.H., 1986. Structure of Concrete and Crack Formation, In: Herrmann, K., Larsson, L. (Eds.), Fracture of Non-Metallic Materials. Springer Netherlands, pp.

309-340.

Wittmann, F.H., Roelfstra, P.E., Sadouki, H., 1985. Simulation and analysis of compositestructures. Materials science and engineering 68, 239-248.

Yang, B., Jiao, Y., Lei, S., 2006. A study on the effects of microparameters on macroproperties for specimens created by bonded particles. Engineering Computations 23, 607-631.

Yang, W.G., Xiang, H.J., 2012. A new approach for the simulation of cementitious materials. Journal of Mechanical Science and Technology 26, 45-51.

Yoon, J., 2007. Application of experimental design and optimization to PFC model calibration in uniaxial compression simulation. International Journal of Rock Mechanics and Mining Sciences 44, 871-889.

Zhong, X., Chang, C.S., 1999. Micromechanical modeling for behavior of cementitious granular materials. Journal of engineering mechanics 125, 1280-1285.

Zhu, W.C., Tang, C.A., Wang, S.Y., 2005. Numerical study on the influence of mesomechanical properties on macroscopic fracture of concrete. Structural Engineering and Mechanics 19, 519-533.

Zhu, W.C., Teng, J.G., Tang, C.A., 2004a. Mesomechanical model for concrete. Part I: Model development. Magazine of Concrete Research 56, 313-330.

Zhu, W.C., Teng, J.G., Tang, C.A., 2004b. Mesomechanical model for concrete. Part II: Applications. Magazine of Concrete Research 56, 331-345.

Chapter 3

Discrete Element Modeling of Concrete – Basic Formulation

The distinct element method or discrete element method is the most widely adopted non-continuum mechanics based numerical approach in the field of rock and concrete structure. Originally used in numerical simulation of the progressive failure of the rock slopes, its most important feature was able to reflect the slip, separation and rotation on contact surfaces between rock blocks and calculation of deformation and stress within rock blocks. The discrete element method splits blocks into tetrahedral elements and utilizing finite difference method to analysis deformation and stress. Since the discrete element method was proposed, further developments including extensions to three-dimensional applications and deformable blocks instead of rigid blocks have been conducted. Williams (Willam *et al.*, 1987) utilized the modal method to analyse deformation of blocks; Ghaboussi (Ghaboussi, 1988) modeled blocks as single quadrilateral elements; Lemos (de Lemos, 1997) developed the discrete element method and applied it to study dynamic interaction between structures and foundations. The hybrid distinct element-boundary element analysis was first implemented by Lorig (Lorig *et al.*, 1986); Munjiza (Munjiza *et al.*, 1995) successfully implemented the coupled finite element and discrete element method.

Base on the framework of the block discrete element method, Cundall (Cundall and Strack, 1979) proposed granular assemblies and constructed layout of particle flow method. 2D disk code *Ball* and 3D sphere code *Trubal* have been developed which were prototypes of commercial software PFC2D (PFC2D, 1999) and PFC3D (PFC3D, 1999). Since then the particle flow code has been widely used to solve rock, soil and concrete mechanics and engineering problems, mainly focusing on resolving mechanisms of damage and fracture of materials from meso-mechanical perspective. The macro-properties of bulk materials are affected by particle and bond stiffness and strength, particle size, shape, packing arrangement and density and other medium interaction factors. Utilizing particle flow code, meso-structure of materials can be simulated and compared with the macro-response of material properties obtained from experimental tests to establish a quantitative relationship between both micro-parameters and macro-properties. The particle flow code has also been widely adopted in powder processing, milling and crushing technology, mining engineering and chemical pharmaceutical. This chapter reviews the basic formulations of the discrete element method, and also introduce the particle flow code.

3.1 Overview of the discrete element method

The discrete element method as a particle based approach was originally proposed by Cundall (Cundall, 1971) for rock-mechanics problems, and then applied to soils by Cundall and Strack (Cundall and Strack, 1979). Since then it has been widely used as a numerical method for modeling soil and rock-like materials. The discrete element approach is based on discontinuous mechanics and the basic idea is to model the elements as rigid simple geometric entities such as disks, spheres, ellipses, or ellipsoids, so that Newton's equation of motion can be applied to entities individually. In addition, in order to obtain the response as an assembly system, the specified interaction forces

between the particles/elements are introduced based on appropriate physical interaction laws.

The contact model of two rigid entities in the discrete element approach can be classified as 'soft-contact' and 'hard-contact'(Duran, 2000). Fig.3.1 illustrates schematically the differences between these two approaches. The essential difference is that in the soft-contact model a small overlap between two rigid particles is allowed and the magnitude of this overlap is related to the contact forces developed through various predefined interaction laws. On the other hand, the hard-contact model (Hoomans *et al.*, 1996) calculates the particle motion by considering the energy loss during the impact. Most particulate mechanics models adopted the soft-contact approach, while the hard-contact model is suited for simulation of classic Newtonian mechanics problem (O'Sullivan, 2011).

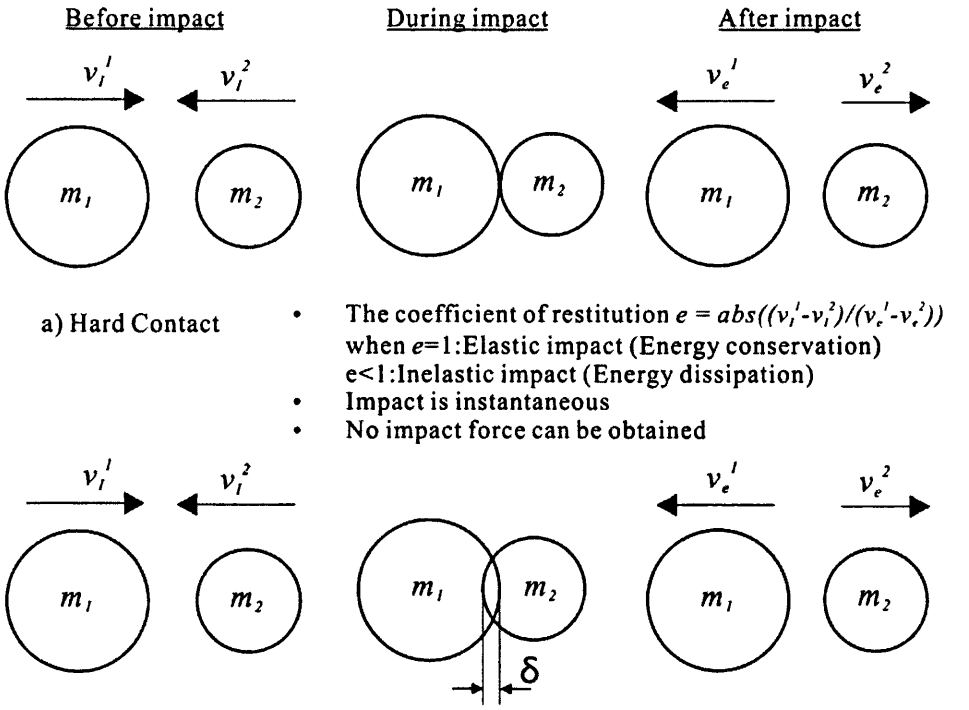

Figure 3.1: Soft and hard contact model.

The particle flow method is based on the following assumptions (Cundall and Strack, 1979):

- The particles are circular or spherical rigid bodies with a finite mass.
- The particles move independently of one another and can both translate and rotate.
- The particles only interact at the contact.
- The soft contact model is adopted and the overlap between the two particles in contact is allowed to represent deformation.
- All overlaps are small in relation to the particle size such that contacts occur over a small region and can be treated as point contact.
- Bonds with finite stiffness can exist at contacts, and these bonds carry load and may break. The particles at a bonded contact need not overlap.

By assuming circular and spherical rather than polygonal-shaped particles, the contact detection is much simpler and can be performed with a much higher computational efficiency. The calculation cycle is illustrated in Fig 3.2. At the beginning of each timestep, the set of contacts is updated from the known particle and boundary positions. The contact forces are calculated by applying the force-displacement laws to each contact based on the relative motion between the two particles at the contact and the predefined constitutive models. Next, to update particles accelerations, velocities and positions as well as boundary walls positions, the law of motion is applied to each particle taking into account the resultant force and moment arising from the contact forces and body force acting on the particle. The calculations performed parallel between law of motion and force-displacement law because the set of input data remains fixed during the execution.

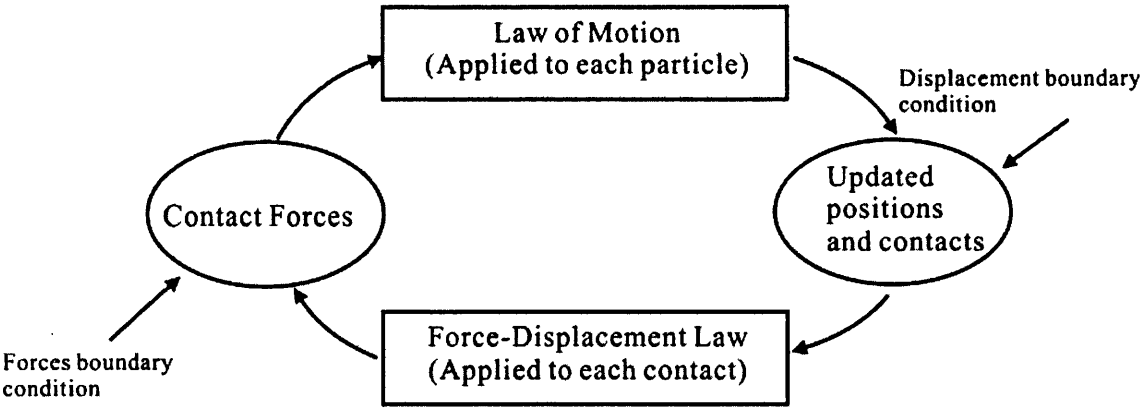

Figure 3.2: Calculation cycle in discrete element method.

The sections below will discuss force-displacement laws, law of motion and timestep determination in detail, it should be noticed that all formulas presented in this chapter are extracted from *PFC* manual (Itasca, 1999) .

3.2 Principle formulations

3.2.1 Force-displacement laws

The force-displacement laws link the contact forces between two particles in contact to their relative displacements. The contact between two circular or sphere in soft-contact model occurs at a point. The contacts behavior between ball-ball and ball-boundary wall described in this section ignore any cementatious bond effect which will be discussed in detail in later sections. Fig 3.3 illustrates the notations used to describe typically contact where A, B, b represent the particles, w is boundary wall, R is particle radius, n_i is unit normal vector, x and U^n denotes coordinates and overlap respectively.

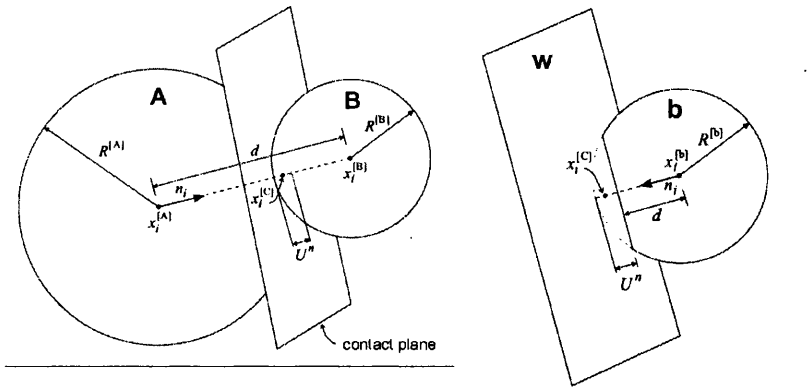

(a) ball-ball contact (b) ball-wall contact

Figure 3.3: Notations used to describe contacts (Itasca, 1999).

The unit normal vector n_i of the ball-ball contact plane is given by:

$$n_i = \frac{x_i^{[B]} - x_i^{[A]}}{d} \tag{3.1}$$

where $x_i^{[A]}$ and $x_i^{[B]}$ are the position vectors of the centers of balls A and B, and d is the distance between the ball centers:

$$d = \left| x_i^{[B]} - x_i^{[A]} \right| = \sqrt{(x_i^{[B]} - x_i^{[A]})(x_i^{[B]} - x_i^{[A]})} \tag{3.2}$$

For ball-wall contact, n_i is directed along the line defining the shortest distance d between the ball center and the wall. Once the unit normal is defined, the overlap U^n, which is defined to be the relative contact displacement in normal direction, and the point of contact $x_i^{[C]}$ are given by (2.3) and (2.4) respectively:

$$U^n = \begin{cases} R^{[A]} + R^{[B]} - d & \text{ball-ball contact} \\ R^{[b]} - d & \text{ball-wall contact} \end{cases} \tag{3.3}$$

$$x_i^{[C]} = \begin{cases} x_i^{[A]} + (R^{[A]} - \frac{1}{2}U^{[n]})n_i & \text{ball-ball contact} \\ x_i^{[b]} + (R^{[b]} - \frac{1}{2}U^{[n]})n_i & \text{ball-wall contact} \end{cases} \tag{3.4}$$

The shear component of the contact displacement is calculated in an incremental form. The increment of shear contact displacement at each time step is evaluated as:

$$\Delta U^s = V^s \Delta t \tag{3.5}$$

$$V^s = (\dot{x}_i^{\Phi_2} - \dot{x}_i^{\Phi_1})t_i - \omega_3^{\Phi_2}\left|x_k^{[C]} - x_k^{\Phi_2}\right| - \omega_3^{\Phi_1}\left|x_k^{[C]} - x_k^{\Phi_1}\right| \tag{3.6}$$

$$\{\Phi_1, \Phi_2\} = \begin{cases} \{A, B\} & \text{ball-ball contact} \\ \{b, w\} & \text{ball-wall contact} \end{cases} \tag{3.7}$$

where $\dot{x}_i^{[\Phi^j]}$ and $\omega_3^{[\Phi^j]}$ are the translation and rotational velocity and $t_i = \{-n_2, n_1\}$.

Once the normal and shear component overlaps are known, the force-displacement laws can be applied to calculate the contact forces. Note that the normal stiffness, K^n, is a secant modulus in that it relates the total displacement and the normal force. The shear stiffness, k^s, is a tangent modulus in that it relates the incremental displacement and the tangential force. At the end of each timestep, the new shear contact force is updated by summing the old shear force existing at the start of the timestep with the shear elastic force increment.

$$F = F^n + F^s \tag{3.8}$$

$$F^n = K^n U^n \tag{3.9}$$

$$\Delta F^s = -k^s \Delta U^s \quad \text{with} \quad F^s \le \mu F^n \tag{3.10}$$

3.2.2 Law of motion

The motion of a rigid particle can be described in terms of the translational motion of the center of mass and the rotational motion of the particle. The equations of motion can be expressed as two vector equations, one of which relates the resultant force to the translational motion, and the other relates the resultant moment to the rotational motion. The equation for translational motion is express as:

$$m\ddot{x}_i = F_i + mg_i \tag{3.11}$$

where F_i is the resultant force; m is the total mass of the particle; and g_i is the body force acceleration vector. The equation for rotational motion:

$$M_i = \dot{H}_i \tag{3.12}$$

Where M_i is the resultant moment; and $\dot{H}_i$ is the angular momentum. If the local system lies along the principal axes of inertia of particle, then Eq. 3.12 reduces to:

$$\begin{aligned} M_1 &= I_1\dot{\omega}_1 + (I_3 - I_2)\omega_3\omega_2 \\ M_2 &= I_2\dot{\omega}_2 + (I_1 - I_2)\omega_1\omega_3 \\ M_3 &= I_3\dot{\omega}_3 + (I_2 - I_1)\omega_1\omega_2 \end{aligned} \tag{3.13}$$

where I_j are the principal moments of inertia of the particle; $\dot{\omega}_j$ are the angular accelerations about the principal axes; and M_j are the components of the resultant moment. For either a spherical or disk-shaped particle with the mass uniformly distributed then the center of mass coincides with the sphere or disk center. For a spherical particle, the three principal moments of inertia are the same. For disk-shaped particle, $\omega_1 = \omega_2 \equiv 0$. Eq. (3.13) can be simplified as:

$$M_3 = I\dot{\omega}_3 = (\beta mR^2)\dot{\omega}_3 \tag{3.14}$$

$$\beta = \begin{cases} 2/5 & \text{spherical particle} \\ 1/2 & \text{disk-shaped particle} \end{cases} \tag{3.15}$$

The equations of translational and rotational motion are integrated using the central finite-difference procedure and the translational and rotational accelerations can be expressed as:

$$\ddot{x}_i^{\,t} = \frac{1}{\Delta t}(\dot{x}_i^{(t+\Delta t/2)} - \dot{x}_i^{(t-\Delta t/2)}) \tag{3.16}$$

$$\dot{\omega}_3^{\,t} = \frac{1}{\Delta t}(\omega_3^{(t+\Delta t/2)} - \omega_3^{(t-\Delta t/2)}) \tag{3.17}$$

Submitting Eqs. (3.16) and (3.17) into Eqs. (3.11) and (3.12) respectively results in

$$\dot{x}_i^{(t+\Delta t/2)} = \dot{x}_i^{(t-\Delta t/2)} + \left(\frac{F_i^t}{m} + g_i\right)\Delta t \tag{3.18}$$

$$\omega_3^{(t+\Delta t/2)} = \omega_3^{(t-\Delta t/2)} + \left(\frac{M_3^{\,t}}{I}\right)\Delta t \tag{3.19}$$

Finally, the velocities in Eq. (3.19) are used to update the position of the particle centre as

$$x_i^{(t+\Delta t)} = x_i^{\,t} + \dot{x}_i^{(t+\Delta t/2)}\Delta t \tag{3.20}$$

3.2.3 Timestep determination

The solution process is computational intensive because of the small time-steps imposed in the explicit-integration procedure and the contact detection routines that need to be executed at every time step. The equations of motion are integrated using the centered finite-difference scheme. The computed solution process will remain stable only if the timestep does not exceed a critical timestep that is related to the minimum eigenperiod of the total system. However, global eigenvalue analysis is impractical to apply to a large and constantly changing system. Therefore, a simplified procedure is

implemented to estimate at the start of each cycle and the actual timestep used in simulation is taken as a fraction of this estimated value.

First, consider a single mass-spring system as shown in Fig. 3.4. The motion of this system is governed by the differential equation: $-kx = m\ddot{x}$ and the critical timestep for a second-order finite-difference scheme is given by Bathe and Wilson (Bathe and Wilson, 1976):

$$t_{crit} = \frac{T}{\pi}; T = 2\pi\sqrt{\frac{m}{k}} \tag{3.21}$$

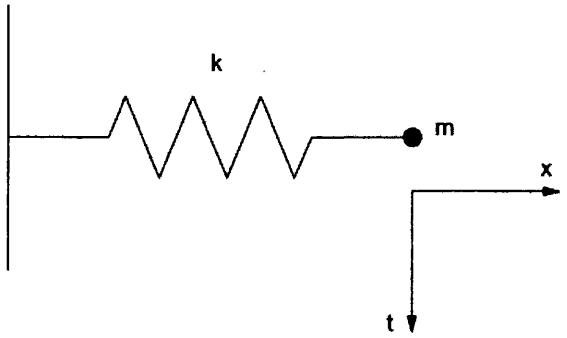

Figure 3.4: Single mass-spring system (Itasca, 1999).

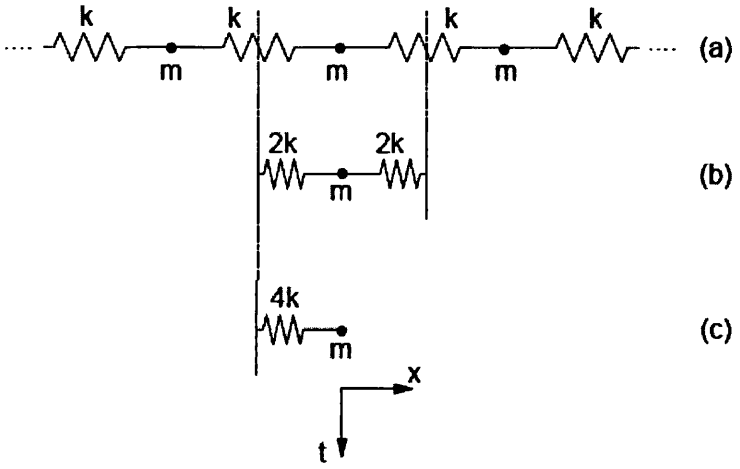

Figure 3.5: Multiple mass-spring system (Itasca, 1999).

For computational efficiency reasons the infinite series of point mass-spring system can be simplified as the system shown in Fig. 3.5 and the critical timestep for such system is:

$$t_{crit} = \frac{T}{\pi} = 2\sqrt{\frac{m}{4k}} = \sqrt{\frac{m}{k}} \tag{3.22}$$

For the rotational system, the same approach can be applied to obtain:

$$t_{crit} = \sqrt{\frac{I}{k_{rot}}} \tag{3.23}$$

Then the overall critical timestep for each calculation cycle is given by:

$$\Delta t = \min(\sqrt{m / k^{tran}}, \sqrt{I / k^{rot}}) \tag{3.24}$$

where m is particle mass; I is the moment of inertia of the particle; k^{tran} and k^{rot} are the translational and rotational stiffness.

3.3 Contact constitutive models

In order to simulate the complex mechanical behavior of a material, the constitutive model at each contact consists of three parts: a stiffness model, a slip model, and a bonding model. The stiffness model provides an elastic relation between the normal contact force and displacement. The slip model imposes a relation between shear and normal contact forces. The bonding model limits the total normal and shear forces that the contact can carry.

3.3.1 Contact-stiffness models

In the Particle Flow Code, two contact-stiffness models are provided: 1) linear model; 2) simplified Hertz-Mindlin model. In linear contact model the two entities in contact are

treated as two springs acting in series, therefore the normal stiffness and shear stiffness is given by Eqs. (3.25) and (3.26):

$$K^n = \frac{k_n{}^A k_n{}^B}{k_n{}^A + k_n{}^B} \tag{3.25}$$

$$k^s = \frac{k_s{}^A k_s{}^B}{k_s{}^A + k_s{}^B} \tag{3.26}$$

where k_j^A *and* k_j^B is the entity stiffness. The simplified Hertz-Mindlin model is a nonlinear model in which the contact stiffness is related to the entities' shear modulus G and Poisson's ratio v:

$$K^n = \left(\frac{2\langle G \rangle \sqrt{2\tilde{R}}}{3(1-\langle v \rangle)} \right) \sqrt{U^n} \tag{3.27}$$

$$K^s = \left(\frac{2\left(\langle G \rangle^2 3\left(1-\langle v \rangle\right)\tilde{R}\right)^{1/3}}{2-\langle v \rangle} \right) \left| F_i^n \right|^{1/3} \tag{3.28}$$

where U^n denotes the overlap, and $\left|F_i^n\right|$ is the magnitude of the normal contact force. The multipliers $\tilde{R}, \langle G \rangle$ *and* $\langle v \rangle$ depend on geometric and material properties of the entities in contact.

For ball-ball contact:

$$\tilde{R} = \frac{2R^{[A]}R^{[B]}}{R^{[A]} + R^{[B]}} \tag{3.29}$$

$$\langle G \rangle = \frac{1}{2}\left(G^{[A]} + G^{[B]}\right) \tag{3.30}$$

$$\langle v \rangle = \frac{1}{2}\left(v^{[A]} + v^{[B]}\right) \tag{3.31}$$

For ball-wall contact:

$$\tilde{R} = R^{[ball]} \tag{3.32}$$

$$\langle G \rangle = G^{[ball]} \tag{3.33}$$

$$\langle v \rangle = v^{[ball]} \tag{3.34}$$

$$F_i^s = \mu \left| F_i^n \right| \left(F_{\max}{}^s / F_i^n \right) \tag{3.35}$$

3.3.2 The slip model

The slip model is an intrinsic property of the two entities in contact. It does not provide normal tensile strength and allows slip to occur by limiting the shear force. This model is always active unless a contact bond model presents (refer to Section 3.3.3), in which the contact bond model behavior supersedes the slip model. The maximum allowable shear force is expressed as

$$F_{\max}^s = \mu \left| F_i^n \right| \tag{3.36}$$

where μ is the minimum friction coefficient of two entities in contact. The slip occurs when $\left| F_i^s \right| > F_{\max}^s$, and the magnitude of shear force F_i^s is equal to $F_{\max}^s$.

3.3.3 Bond model

The previous sections present basic formulations of the discrete element method, the interactions between particles specified in terms of contact laws which enforce the impenetrability of the particles, but no tensile resistance is introduced to the particles in contact. However, most of geomaterials exhibit a certain amount of cohesion/bonding effect between grains as shown in Fig.3.6. Also in order to simulate a material that is a continuum at the microscopic level, introduction of bonding effects between discrete element particles to represent the initial state is required. Such bonding effects can be

modelled by the Bond Particle Model (BPM) which has been widely applied to geotechnical applications.

Contact bond model

The contact bond model extends the conventional contact law for a bonded pair of particles such that it resists against the tensile elongation as well as compression by introducing bonding effect at contact point. It behaviors like a pair of elastic springs with constant normal and shear stiffness acting at the contact point. In the presence of a contact bond model, the shear contact force is limited by a predefined contact bond shear strength. The bond breakage occurs when either normal or shear contact force exceeds the contact bond strength. The constitutive behavior relating the normal and shear components of contact force and relative displacement is shown in Fig.3.6. Huang (Huang, 1999) and Diederichs (Diederichs, 1999) reproduced the rock constitutive behavior by utilizing the contact bond model. Diederichs investigates the role of bond tensile strength and damage accumulation prior to the peak strength at low confinement for Lac du Bonnet granite and points out that the effect of rotation may be significant after the deformation band formation.

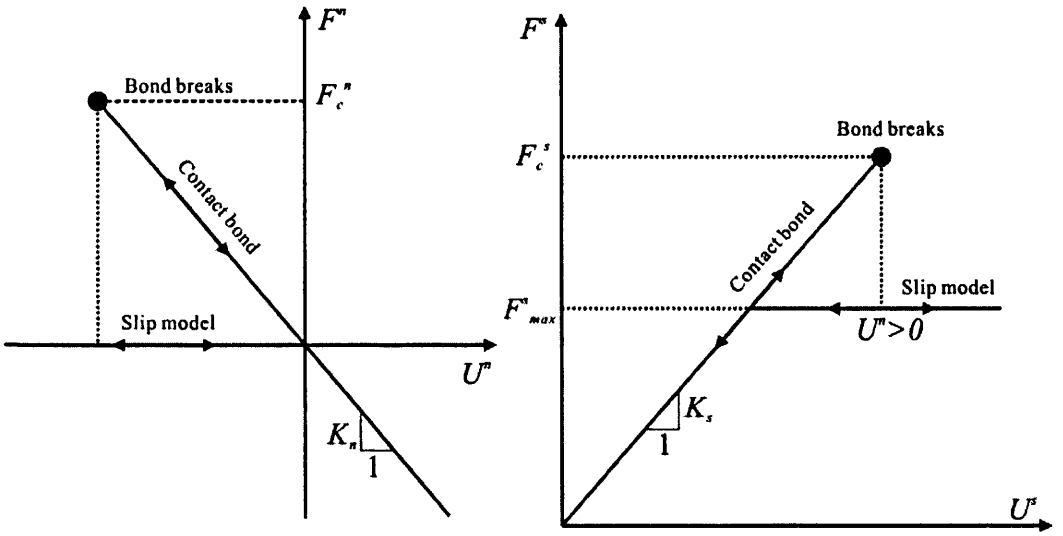

(a) Normal component of contact force (b) shear component of contact force

Figure 3.6: Schematic of contact bond model and slip model (Itasca, 1999).

Parallel bond model

One of the major drawbacks of contact bond model is that the moment and rolling resistance have not been taken into account. Wang and Mora (Wang and Mora, 2008) conducted the uniaxial compression tests with a pre-existing crack to reproduce the wing crack extension mechanism and they suggested that the failure mechanisms remains stable only when normal, shear and bending stiffness exist and particle rotation is permitted. Iwashita and Oda (Iwashita and Oda, 1998) introduced the rotational resistance between particles with an additional moment related slider and showed its effectiveness not only for improving the representation of the macroscopic stress strain relationship but also for reproducing the experimentally observed microstructural development. Jiang (Jiang *et al.*, 2007) also take into account the rotational resistance between particles but they assume a finite bond contact width evenly distributed with infinite basic elements in the normal and tangential directions to a contact bond.

Potyondy and Cundall (Potyondy and Cundall, 2004) proposed a model that considers the grains and bonds separately. The parallel bond inserts an additional cementatious material with finite area between two contact particles. This model can be envisioned as a beam-like material with a finite area connecting two particles centroid. By introducing such mechanism, resistance to bending moment or oppose rolling can be incorporated. Bond breakage is evaluated either by the maximum tensile or shear stress, which are obtained from the total force and moment acting on the bond. This model acts in parallel with the slip or contact bond model thus does not preclude the possibility of slip. Fig.3.7 illustrates the schematic of the grain contact model while Fig.3.8 denotes the contact and deformation modes of the parallel bond model.

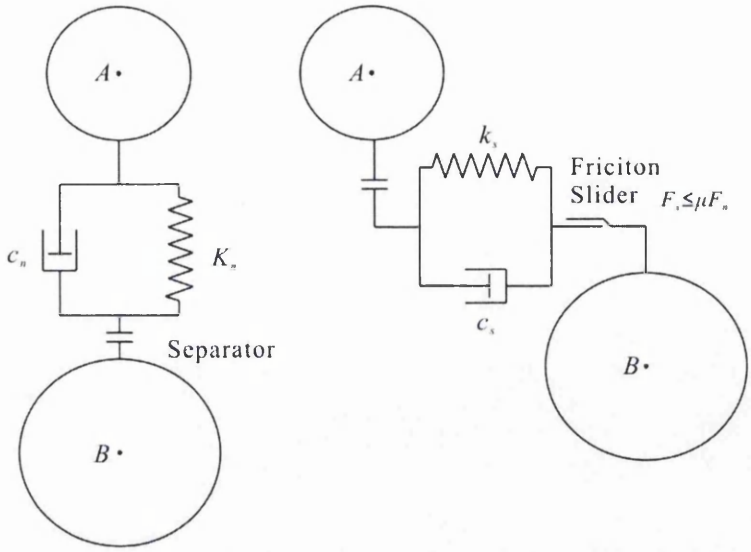

(a) Normal Direction (b) Tangential Direction

Figure 3.7: Schematic of the grain contact model.

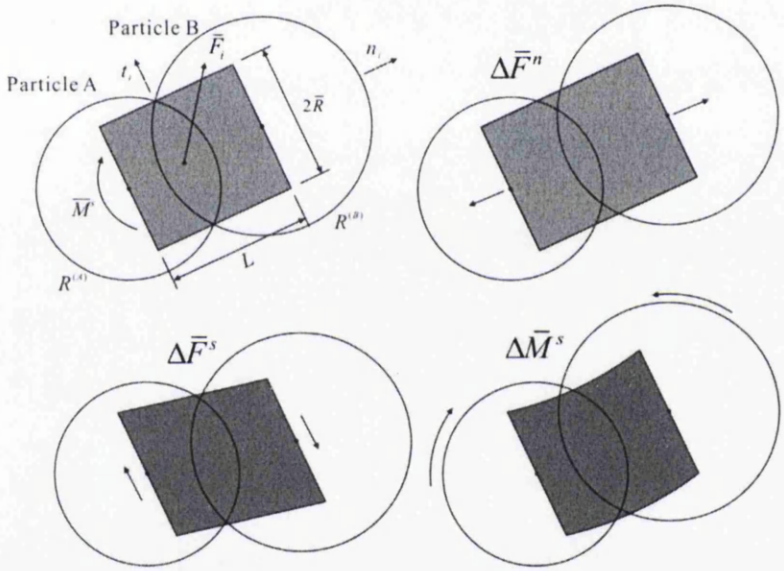

Figure 3.8: Parallel contact model and deformation modes.

The interaction laws for bonding behavior are

$$\begin{aligned} \Delta\bar{F}^n &= \bar{k}^n A \Delta U^n \\ \Delta\bar{F}^s &= -\bar{k}^s A \Delta U^s \\ \Delta\bar{M}^n &= -\bar{k}^s J \Delta\theta^n \\ \Delta\bar{M}^s &= -\bar{k}^n I \Delta\theta^s \end{aligned} \tag{3.37}$$

The modulus-stiffness scaling relations are

$$
\begin{aligned}
k_n &= \begin{cases} 2tE_c, & t=1, \quad \text{PFC2D} \\ 4RE_c, & \quad \text{PFC3D} \end{cases} \\
k_s &= \frac{k_n}{(k_n / k_s)} \\
\bar{k}_n &= \frac{\bar{E}_c}{R^{(A)} + R^{(B)}} \\
\bar{k}_s &= \frac{\bar{k}_n}{(\bar{k}_n / \bar{k}_s)}
\end{aligned}
\tag{3.38}
$$

where R is the particle radius and A, I and J are the area, second moment of area and polar moment of inertia of the beam-like element, respectively. These values are dependent on the inserted beam with $2\bar{R}$:

$$
\begin{aligned}
A &= \begin{cases} 2\bar{R}t, & t=1, \quad \text{PFC2D}, \\ \pi\bar{R}^2, & \quad \text{PFC3D}, \end{cases} \\
I &= \begin{cases} \frac{2}{3}\bar{R}^3 t, & t=1, \quad \text{PFC2D}, \\ \frac{1}{4}\pi\bar{R}^4, & \quad \text{PFC3D}, \end{cases} \\
J &= \begin{cases} NA & \text{PFC2D}, \\ \frac{1}{2}\pi\bar{R}^4, & \text{PFC3D}. \end{cases}
\end{aligned}
\tag{3.39}
$$

Hence, the bond radius $\bar{R}$ has a significant impact on the stress-displacement relationship at a microscopic level, and in the particle flow code package, it is defined by the expression:

$$
\bar{R} = \bar{\lambda} \min(R^{(A)} + R^{(B)}) \tag{3.40}
$$

where $R^{(A)}$ and $R^{(B)}$ are the bonded particle radii. The additional parameter $\bar{\lambda}$ is denoted as the radius coefficient and determines the ratio of the bond width to the minimum radius of the particles in contact.

Utilizing the beam theory in conjunction with a finite contact width allows the contact forces to be related to contact stresses. This leads to evaluation of the maximum tensile and shear stresses acting on the bond as follows:

$$\bar{\sigma}^{max} = \frac{-\bar{F}^n}{A} + \frac{|\bar{M}^s|\bar{R}}{I}$$
$$\bar{\tau}^{max} = \frac{|\bar{F}|^s}{A} + \frac{|\bar{M}^n|\bar{R}}{J} \qquad (3.41)$$

Softening model

Both contact and parallel bond model behaviour linear elastically and fracture of bonds is brittle and sudden, for this reason, those two bond models are ideally suited to model brittle materials such as rock. More sophisticated bond model required to simulation plastic or adhesive materials. One of many alternative models is displacement softening model and its bilinear behavior is shown in Figure 3.9.

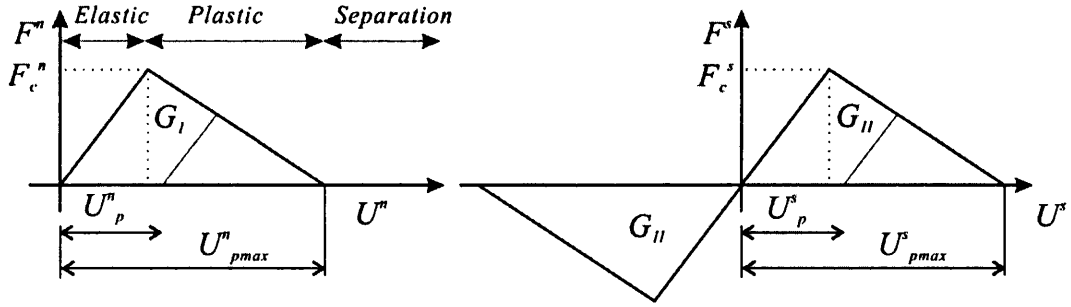

(a) Normal direction (b) Shear direction

Figure 3.9: Strength-softening curve.

The displacement softening model is similar to cohesive zone model in continuum mechanics. Before bond force reaches its peak value F_c displacement softening model behaves like contact bond and accumulate plastic deformation after peak value by linearly softening the bond strength. The area under local softening model is the fracture energy required to open the crack surface. The initial slope of the curve denotes material modulus.

If the contact is in tension, the contact strength, $F_{\max}$, is calculated from the two strength parameters ($F_c^n and\ F_c^s$) as a function of the current orientation of the contact force. It is assumed that contact strength varies as a linear function of the angle, α :

$$F_{\max} = (1 - \frac{2\alpha}{\pi}) \cdot F_c^n + \frac{2\alpha}{\pi} \cdot F_c^s \tag{3.42}$$

where α is the angle between the directions of the contact force and line segment connecting the centers of the two particles. The yielding of the bond in tension is determined by comparing the resultant contact force,i.e.,

$$F = \sqrt{F^{n2} + F^{s2}} \tag{3.43}$$

with the bond strength. The contact yields if the contact force is larger than the contact strength:

$$F > F_{\max} \tag{3.44}$$

In the case of yielding of contact bonds, the increment of contact displacement, ΔU^k can be decomposed into elastic and plastic contact displacement increments. The force increment, ΔF^k, is a function of the increment of the elastic displacement only:

$$\Delta F^k = K^k \Delta U_e^k \ (k = n, s) \tag{3.45}$$

The increment of the plastic displacement obeys the 'flow rule.' It is assumed that, if the normal force is tensile, the plastic displacement increment is always in the direction of the resultant contact force:

$$\Delta U_p = \sqrt{(\Delta U_p^n)^2 + (\Delta U_p^s)^2} \tag{3.46}$$

It the normal contact is compressive, the maximum contact shear force is defined by

the slip condition:

$$F^s_{\max} = \mu \left| F^n \right| + F^s_c \tag{3.47}$$

The contact strength are functions of the accumulated plastic displacements:

$$F^k_c(U_p / U_{p\max}) = F^k_c(1 - \frac{U_p}{U_{p\max}}) \quad where \ U_p = \sum \left| \Delta U_p \right| \tag{3.48}$$

3.4 Mechanical quantity measurement

Stress and strain are two essential continuum quantities, however, these two quantities do not exist at each point in a particle assembly because the discrete element approach computes only the contact forces and displacements at each contact. Stress and strain are very useful when investigating material behavior in the macro-scale. To transfer the forces and displacements information to the stress and strain in the continuum model, averaging procedures are necessary.

3.4.1 Stress measurement

In the context of continuum mechanics the average stress tensor $\bar{\sigma}_{ij}$ in a volume V is defined by:

$$\bar{\sigma}_{ij} = \frac{1}{V} \int \sigma_{ij} dV \tag{3.49}$$

For a discrete system the stress only exist in particles, thus the integral can be replaced by a sum over the numbers of particles (N_p) within the volume as

$$\bar{\sigma}_{ij} = \frac{1}{V} \sum_{N_p} \bar{\sigma}^p_{ij} V^p \tag{3.50}$$

where $\bar{\sigma}_{ij}^{p}$ denotes the average stress tensor in particle p which can be computed as

$$\bar{\sigma}_{ij}^{p} = \frac{1}{V^{p}} \int_{V^{p}} \sigma_{ij}^{p} dV^{p} \tag{3.51}$$

Any tensor S_{ij} can be expressed as Eq. (3.52), where notation $[,i]$ denotes differentiation with respect to x_i.

$$S_{ij} = \delta_{ik} S_{kj} = x_{i,k} S_{kj} = (x_i S_{kj})_{,k} - x_i S_{kj,k} \tag{3.52}$$

Applying Eq. (3.52) to Eq. (3.51) results in

$$\bar{\sigma}_{ij}^{p} = \frac{1}{V^{p}} \int_{V^{p}} \left[\left(x_i \bar{\sigma}_{ij}^{p} \right)_{,k} - x_i \bar{\sigma}_{ij,k}^{p} \right] dV^{p} \tag{3.53}$$

Applying the Gauss divergence theorem to the first term in the right hand side, and taking into the fact that the second term vanishes in the absence of body forces, lead to

$$\bar{\sigma}_{ij}^{p} = \frac{1}{V^{p}} \int_{S^{p}} \left(x_i \bar{\sigma}_{ij}^{p} \right) n_k dS^{p} = \frac{1}{V^{p}} \int_{S^{p}} x_i t_j^{p} dS^{p} \tag{3.54}$$

where S^{p} is the particle surface; n_k is the unit outward normal to the surface; t_j^{p} is the traction vector. Replacing the integral by a sum over the contacts (N_c) as

$$\bar{\sigma}_{ij}^{p} = -\frac{1}{V^{p}} \sum_{N_c} x_i^{c} F_j^{c} \tag{3.55}$$

where F_j^{c} is the contact force and x_i^{c} is the contact location which can be written as

$$x_i^{c} = x_i^{p} + \left| x_i^{c} - x_i^{p} \right| n_i^{(c,p)} \tag{3.56}$$

where x_i^p is the location of the particle centroid; and $n_i^{(c,p)}$ is the unit-normal vector directed from the particle centroid to the contact location. Substituting Eq. (3.56) to Eq. (3.55) and noting that

$$\sum_{N_c} F_j^c = 0 \tag{3.57}$$

for a particle in equilibrium, we obtain:

$$\bar{\sigma}_{ij}^p = -\frac{1}{V^p}\sum_{N_c}\left|x_i^c - x_i^p\right| n_i^{(c,p)} F_i^c \tag{3.58}$$

To apply the above procedure to the particle within the area defined by a measurement circle, a correction process is necessary to account the additional area of particles that is being neglected because the particle centroid is not within the measurement domain. The correction factor is based on the porosity of measurement circle (n) and assuming that a uniform stress field σ_0 exists within the measurement domain. The correct expression for the average stress $\bar{\sigma}$ is given by

$$\begin{aligned}\bar{\sigma} &= \frac{1}{V^m}\sum \bar{\sigma}^p V^p = \frac{1}{V^m}\bar{\sigma}^p \sum V^p \\ &= \sigma_0\left(\frac{\sum V^p}{V^m}\right) = \sigma_0(1-n)\end{aligned} \tag{3.59}$$

If only these particles centroid within the measure circle to be accounted, the *incorrect* average stress $\tilde{\sigma}$ is given by

$$\tilde{\sigma} = \frac{1}{V^m}\sum_{N_p} \bar{\sigma}^p V^p = \sigma_0\left(\frac{\sum_{N_p} V^p}{V^m}\right) \tag{3.60}$$

The relation between the correct and *incorrect* average stress is given by

$$\frac{\bar{\sigma}}{\tilde{\sigma}} = \left(\frac{1-n}{\sum_{N_p} V^p} \right) V^m \tag{3.61}$$

Eliminate $\tilde{\sigma}$ using Eq. (3.59) to obtain final corrected expression for the average stress

$$\bar{\sigma} = \left(\frac{1-n}{\sum_{N_p} V^p} \right) \sum_{Np} \bar{\sigma}^p V^p \tag{3.62}$$

The final expression used to compute the average stress tensor is found by substituting Eq. (3.58) into Eq. (3.62) to obtain

$$\bar{\sigma}_{ij} = -\left(\frac{1-n}{\sum_{N_p} V^p} \right) \sum_{N_p} \sum_{N_c} \left| x_i^c - x_i^p \right| n_i^{(c,p)} F_j^c \tag{3.63}$$

3.4.2 Strain measurement

Different approaches should be adopted to compute the local strain rate within a particle assembly. When considering the local stress of discrete assembly, the average stress within a volume can be expressed directly in terms of the contact forces, since the forces in the voids are zero. However, the velocities in the voids are nonzero. Therefore, the local strain rate is calculated by employing the best-fit and least-squares procedure.

The relation between displacements u_i at two adjacent points is described by the displacement gradient tensor α_{ij} and this tensor can be decomposed into a symmetric and an anti-symmetric tensor as Eq. (3.64)

$$du_i = u_{i,j} dx_j = \alpha_{ij} dx_j \tag{3.64}$$

$$\alpha_{ij} = e_{ij} - \omega_{ij}$$
$$e_{ij} = \frac{1}{2}\left(u_{i,j} - u_{j,i}\right) \quad \text{infinitesimal strain tensor} \tag{3.65}$$
$$\omega_{ij} = \frac{1}{2}\left(u_{j,i} - u_{i,j}\right) \quad \text{rotation tensor}$$

Similarly, the relation between velocities v_i is given by velocity gradient tensor $\dot{\alpha}_{ij}$

$$dv_i = v_{i,j}dx_j = \dot{\alpha}_{ij}dx_j \tag{3.66}$$

$$\dot{\alpha}_{ij} = \dot{e}_{ij} - \dot{\omega}_{ij}$$
$$\dot{e}_{ij} = \frac{1}{2}\left(v_{i,j} + v_{j,i}\right) \quad \text{rate-of-deformation tensor} \tag{3.67}$$
$$\dot{\omega}_{ij} = \frac{1}{2}\left(v_{j,i} - v_{i,j}\right) \quad \text{spin tensor}$$

The average velocity and position of the N_p particles contained in a certain domain can be expressed as follows:

$$\bar{V}_i = \frac{\sum_{N_p} V_i^p}{N_p}$$
$$\bar{V}_i = \frac{\sum_{N_p} x_i^p}{N_p} \tag{3.68}$$

For a particular particle the measured relative velocity values are given by

$$\tilde{V}_i^p = V_i^p - \bar{V}_i \tag{3.69}$$

The predicted relative velocity values $\tilde{v}_i^p$ can be obtained for a given $\dot{\alpha}_{ij}$

$$\tilde{v}_i^p = \dot{\alpha}_{ij}\tilde{x}_i^p$$
$$\tilde{x}_i^p = x_j^p - \bar{x}_i \tag{3.70}$$

A measure of the error in these predicted values is given by

$$z = \sum_{N_p} \left| \tilde{v}_i^p - \tilde{V}_i^p \right|^2 = \sum_{N_p} \left(\tilde{v}_i^p - \tilde{V}_i^p \right) \left(\tilde{v}_i^p - \tilde{V}_i^p \right) \tag{3.71}$$

To minimize this error the following condition must be satisfied

$$\frac{\partial z}{\partial \dot{\alpha}_{ij}} = 0 \tag{3.72}$$

Substituting Eqs. (3.70) into Eq. (3.71) and differentiating obtains

$$\begin{bmatrix} \sum_{N_p} \tilde{x}_1^p \tilde{x}_1^p & \sum_{N_p} \tilde{x}_2^p \tilde{x}_1^p \\ \sum_{N_p} \tilde{x}_1^p \tilde{x}_2^p & \sum_{N_p} \tilde{x}_2^p \tilde{x}_2^p \end{bmatrix} \begin{Bmatrix} \dot{\alpha}_{i1} \\ \dot{\alpha}_{i2} \end{Bmatrix} = \begin{Bmatrix} \sum_{N_p} \tilde{V}_i^p \tilde{x}_1^p \\ \sum_{N_p} \tilde{V}_i^p \tilde{x}_2^p \end{Bmatrix} \tag{3.73}$$

Then solving Eq. (3.73) to obtain the strain-rate tensor.

3.4.3 Energy measurement

Following energy terms can be traced within a discrete particle assembly:

1. Body work: total work done by all body forces including gravity loading and applied forces and moments:

$$E_b \leftarrow E_b + \sum_{N_p} \left((m g_i + F_i) \Delta U_i + M_3 \Delta \theta_3 \right) \tag{3.74}$$

where $N_p, m, g_i, F_i, M_3, \Delta U_i \; and \; \Delta\theta_3$ are respectively the number of particles, mass, gravitational acceleration vector, externally applied force, externally applied moment, computed displacement increment, and computed rotation increment.

2. Bond Energy: total strain energy stored in the parallel bonds:

$$E_{pb} = \frac{1}{2} \sum_{N_p} \left(\left| \bar{F}_i^n \right|^2 / \left(A \bar{K}^n \right) + \left| \bar{F}_i^s \right|^2 / \left(A \bar{K}^s \right) + \left| \bar{M}_3 \right|^2 / \left(I \bar{K}_n \right) \right) \tag{3.75}$$

where N_{pb} is the number of parallel bonds.

3. Boundary work: total accumulated work done by all boundaries:

$$E_w \leftarrow E_w + \sum_{N_w} \left(F_i \Delta U_i + M_3 \Delta \theta_3 \right) \tag{3.76}$$

where N_w is the number of boundary walls; F_i and M_3 are the resultant force and moment acting on the boundaries and assuming to remain constant throughout the timestep; and ΔU_i and $\Delta \theta_3$ are the applied displacement and rotation during the current timestep.

4. Friction work: total energy dissipated by frictional sliding at all contacts:

$$E_f \leftarrow E_f - \sum_{N_c} \left(\left\langle F_i^s \right\rangle \left(\Delta U_i^s \right)^{slip} \right) \tag{3.77}$$

where N_c is the number of contacts; and $\left\langle F_i^s \right\rangle$ and $\left\langle \Delta U_i^s \right\rangle^{slip}$ are the average shear force and the increment of slip displacement.

$$\begin{aligned} \left(\Delta U_i^s \right)^{slip} &= \Delta U_i^s - \left(\Delta U_i^s \right)^{elas} = \Delta U_i^s + \frac{\left(\Delta F_i^s \right)^{elas}}{k^s} \\ &= \Delta U_i^s + \frac{\left(F_i^s \right)^{(t+\Delta t)} - \left(F_i^s \right)^t}{k^s} \end{aligned} \tag{3.78}$$

5. Kinetic energy: total kinetic energy of all particles accounting for both translational and rotation motion.

$$E_k = \frac{1}{2} \sum_{N_b} \left(m_i V_i^2 + I_i \omega_i \cdot \omega_i \right) \tag{3.79}$$

6. Strain energy: total strain energy of the entire assembly stored at all contacts assuming a linear contact-stiffness model:

$$E_c = \frac{1}{2} \sum_{N_c} \left(\left| F_i^n \right|^2 / k^n + \left| F_i^s \right|^2 / k^s \right) \tag{3.80}$$

References

Bathe, K.J., Wilson, E.L., 1976. Numerical Methods in Finite Element Analysis Englewood Cliffs:Prentice_Hall.

Cundall, P.A., 1971. A Computer Model for Simulating Progressive Large Scale Movements in Blocky Rock Systems, Proceedings of the Symposium of the International Society of Rock Mechanics, Nancy, France, pp. Paper No. II-8.

Cundall, P.A., Strack, O.D.L., 1979. A discrete numerical model for granualar assemblies. Geotechnique 29, 47-56.

de Lemos, J.A.S.V., 1997. A distinct element model for dynamic analysis of jointed rock with application to dam foundations and fault motion. University Microfilms.

Diederichs, M.S., 1999. Instability of Hard Rockmasses: The Role of Tensile Damage And Relaxation. University of Waterloo.

Duran, J., 2000. Sands, powders, and grains: An introduction to the physics of granular materials. Springer, New York.

Ghaboussi, J., 1988. Fully deformable discrete element analysis using a finite element approach. Computers and Geotechnics 5, 175-195.

Hoomans, B.P.B., Kuipers, J.A.M., Briels, W.J., Van Swaaij, W.P.M., 1996. Discrete particle simulation of bubble and slug formation in a two-dimensional gas-fluidized bed: A hard-sphere approach. Chm. Eng. Sci 51(1), 99-108.

Huang, H.Y., 1999. Discrete element modeling of tool-rock interaction. American: University of Minnesota.

Itasca, 1999. PFC3D user's guide [M], Minneapolis: Minnesotta.

Iwashita, K., Oda, M., 1998. Rolling resistance at contacts in simulation of shear band development by dem. Journal of engineering Mechanics-asce 124, 285-292.

Jiang, M., YU, H.S., Leroueil, S., 2007. A simple and efficient approach to capturing bonding effect in naturally microstructued sand by discrete element method. International Journal for Numerical Methods in Engineering 69, 1158-1193.

Lorig, L., Brady, B., Cundall, P., 1986. Hybrid distinct element-boundary element analysis of jointed rock, International Journal of Rock Mechanics and Mining Sciences & Geomechanics Abstracts. Elsevier, pp. 303-312.

Munjiza, A., Owen, D., Bicanic, N., 1995. A combined finite-discrete element method in transient dynamics of fracturing solids. Engineering computations 12, 145-174.

O'Sullivan, C., 2011. Particle-Based Discrete Element Modeling: Geomechanics Perspective. International Journal of Geomechanics 11, 449–464.

PFC2D, 1999. Particle flow code in 2 dimensions. Itasca Consulting Group, Inc.

PFC3D, 1999. Particle flow code in 3 dimensions. Itasca Consulting Group, Inc.

Potyondy, D.O., Cundall, P.A., 2004. A bonded-particle model for rock. International Journal of Rock Mechanics and Mining Sciences 41, 1329-1364.

Wang, Y., Mora, P., 2008. Modeling Wing Crack Extension: Implications for the Ingredients of Discrete Element Model. Pure and Applied Geophysics 165, 609-620.

Willam, K., Pramono, E., Sture, S., 1987. Fundamental issues of smeared crack models, SEM-RILEM Int. Conf. on Fracture of Concrete and Rock, pp. 192-207.

Chapter 4

Discrete Element Modeling of Concrete –Preprocessor

Concrete is a composite material with a variety of heterogeneities and is generally treated as a typical cementatious granular material. It is usually considered as two-phase materials of consisting aggregate particles and cement mortar. Further research has revealed that there exists an interfacial transition zone (ITZ) between coarse aggregates and cement mortar. Therefore, concrete should be modeled as a three-phase material at meso-scale.

The heterogeneity of concrete manifests itself at various scales. At meso-scale, the presence of coarse aggregates influences the strength of concrete by developing a zone of weakness in the form of aggregate-matrix interface (Mungule and Raghuprasad, 2011). In order to capture the heterogeneous morphological features of concrete, it is essential to introduce a preprocessor in the numerical modeling to reproduce the aggregate structure in which the shape, size and distribution of the aggregate particles resemble real concrete material. It should be noted that the term 'aggregate' in this research denotes coarse aggregate (i.e., gravel, crushed stone and blast-furnace slag) with size over 4 mm as classified in the European Standard (British Standards Insitution, 2009). Also, the assumed spatial randomness can only

be correct in the overall sense and cannot capture the effect of random local material inhomogeneities on the localization of damage and failure. It is for these reasons that a direct simulation of the random microstructure of these materials is useful (Bažant *et al.*, 1990).

A preprocessor generally consists of two stages:

- Generation of mesoscopic geometric model: the geometric model of aggregate structure can be either randomly generated by utilizing various random aggregate structure generators or scanned from experimental specimen by using image processing technique. Determination of shape and size of aggregates, aggregate content and grading will also be involved.
- Projection of three-phased geometric model onto particle assembly: each particle is assigned to its corresponding phase according to coordinates of the particle center. Then the intrinsic mechanical properties are assigned for the simulation.

4.1 Single aggregate generators

In order to simulate the structure and components of the concrete material, a single aggregate should be generated first. In this study, the single aggregate generator algorithm is adopted following the concepts proposed by Gao and Liu for 2D and 3D random convex polygon or polyhedron aggregates (Gao and Liu, 2003; Liu and Gao, 2003). The benefits of this algorithm includes:

- Simplicity and computational efficiency
- Homology and unitarity between two and three dimensional random aggregates generation algorithms

4.1.1 Area-based and volume-based methods

Area-based and volume-based methods discussed in this section have been adopted by many other researchers as a contact detection scheme. It can also be applied to calculate the area or volume of any arbitrary polygon or polyhedron.

a) Area-based method (2D)

As shown in Fig.4.1, a random convex polygon $a_1 \_ a_n$ which its vertices a_i *and* a_{i+1} with coordinates (x_i, y_i) and (x_{i+1}, y_{i+1}). For any in plane point $P(x, y)$, the area S_i for the triangle Pa_ia_{i+1} can be obtained as:

$$S_i = \frac{1}{2}\begin{vmatrix} x & y & 1 \\ x_i & y_i & 1 \\ x_{i+1} & y_{i+1} & 1 \end{vmatrix}, \begin{matrix} (P,i,i+1) \text{ in counterclockwise order} \\ (P,i,i+1) \text{ in counterclockwise order} \end{matrix} \qquad (4.1)$$

If $S_i > 0 (i = 0,1,\cdots n)$ then point P is inside the polygon (Fig.4.1.a); if at least one $S_i = 0$ then point P is on the edge of the polygon; if any $S_i < 0$ then point P is outside the polygon.

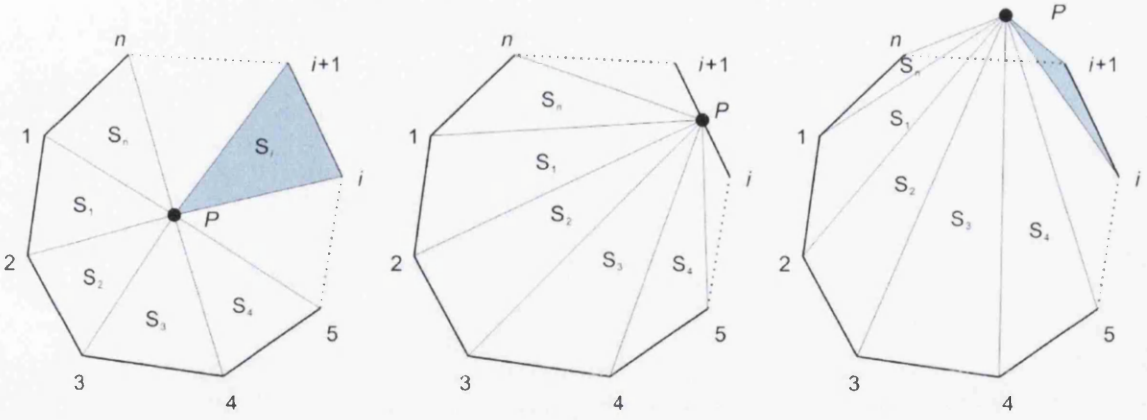

a) Point *P* inside polygon b) Point *P* on the edge c) Point *P* outside polygon

Figure 4.1: Illustration of area-based overlap detection.

b) Volume-based method (3D)

Let $a_1 \_ a_n$ represents a convex polyhedron with triangular faces and the vertices a_i, a_{i+1} and a_{i+2} with coordinates $(x_i, y_i, z_i), (x_{i+1}, y_{i+1}, z_{i+1})$ *and* $(x_{i+1}, y_{i+1}, z_{i+2})$, $P(x, y)$ is an arbitrary point in space. Then the volume V_i of the tetrahedron $Pa_i a_{i+1} a_{i+2}$ can be obtained as:

$$V_i = \frac{1}{6}\begin{vmatrix} x & y & z & 1 \\ x_i & y_i & z_i & 1 \\ x_{i+1} & y_{i+1} & z_{i+1} & 1 \\ x_{i+2} & y_{i+2} & z_{i+2} & 1 \end{vmatrix}, (i, i+1 \, and \, i+2) \text{ in countercloclwise order} \qquad (4.2)$$

If $V_i > 0 (i = 0,1,\cdots n)$ then point P is inside the polyhedron; if at least one $V_i = 0$ then point P is on the edge of the polyhedron; if any $V_i < 0$ then point P is outside the polyhedron.

4.1.2 Growth of single convex polygon aggregate

In order to generate a random polygon aggregate, a seed aggregate with either triangular or quadrilateral shape is generated first. The seed aggregate governs the dimensions and geometrical outcomes of final polygon aggregate. The random number is generated by adopting multiplicative congruential method originally developed by Lehmer (Lehmer, 1951; Taussky and Todd, 1956). It is one of the most wildly used methods to generate pseudorandom numbers because they are easily implemented and fast. A general formula of a random number generator of this type is:

$$x_{n+1} = a x_n (\mathrm{mod} M) \qquad (4.3)$$

where the modulus M is a prime number, the multiplier a is an element of high multiplicative order modulo M, and the seed x_0 is coprime to M.

A set of pseudorandom numbers uniformly distributed between 0 and 1 is returned by calling the library function **rand(seed),** then random numbers between a and b are obtained via Eq.4.4.

$$X' = a + (b - a)X \tag{4.4}$$

The generation of convex polygon aggregates is shown in Fig.4.2 and can be described as following:

- Generation of auxiliary circles that control the size of the seed aggregate: Different quantity and size of the auxiliary circles are generated according to required aggregate grading. The aggregate size can be approximated by the diameters of each auxiliary circle.
- Formation of triangular or quadrilateral seed aggregate: divide the each auxiliary circle into three or four equal curves then randomly pick a point from each curve to be a vertex of triangular or quadrilateral seed aggregate. Monitor and revise shape of the triangles or quadrangles to avoid sharp angles.

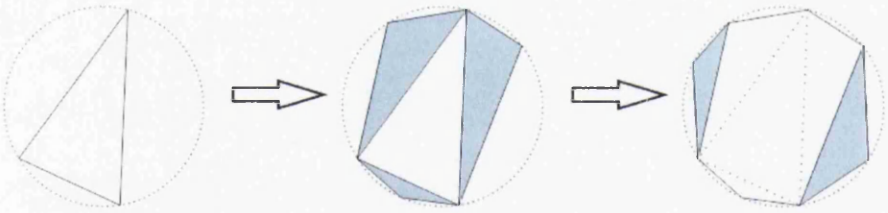

(a) Growth of convex polygon aggregate from triangle seed

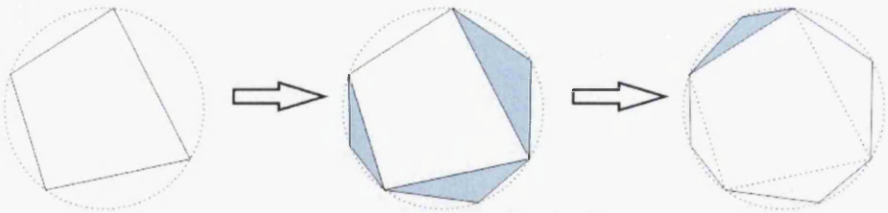

(b) Growth of convex polygon aggregate from quadrilateral seed

Figure 4.2: Growth of convex polygon aggregate from seed aggregate.

- Formation of polygon aggregates by extension of seed aggregates: The growth process is shown in Figs.4.2a and 4.2b. As shown in Fig.4.3, point P is a new vertex and a_iP and Pa_{i+1} are new edges. Conditions are applied to extend the seed polygon such as: at least one of the edges of polygon is greater than the prescribed maximum limited length L_{max} ; new edges must be greater than the prescribed minimum limited length L_{min} ($L_1 > L_{min}$ *and* $L_2 > L_{min}$); the direction of extension is along the outward normal. In order to maintain a convex polygon, the area of each triangle formed by this vertex and each aggregate edge apart from edge a_ia_{i+1} must be positive. The area is calculated by applying Eq.4.1 and all vertices in counterclockwise order. As the previous polygon is already convex, the calculation can be reduced to that the areas of two triangles formed by the new vertex and edge a_ia_{i+1}'s two neighboring edges are positive ($S_{\Delta Pa_{i-1}a_i} > 0$ *and* $S_{\Delta Pa_{i+1}a_{i+2}} > 0$).

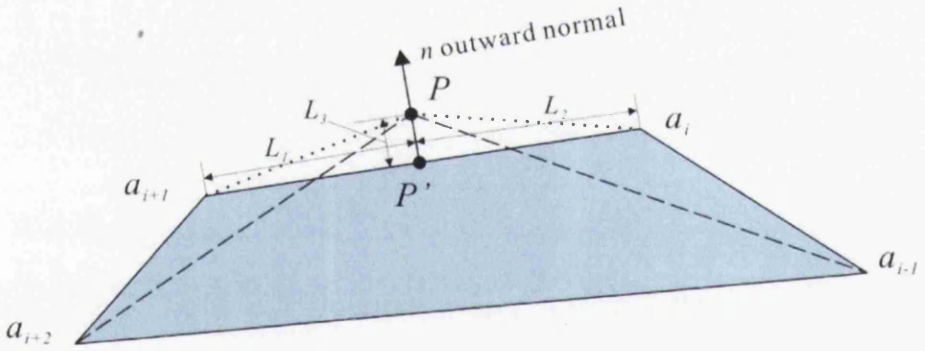

Figure 4.3: Formation of a new vertex for polygon aggregate.

4.1.3 Growth of convex polyhedron aggregates

Similar to growth of convex polygon aggregates, the generation of convex polyhedron starts from a seed aggregate. The seed aggregate is an arbitrary convex octahedron with triangular faces as shown in Fig.4.4. The growth of polyhedron always starts from the longest edge.

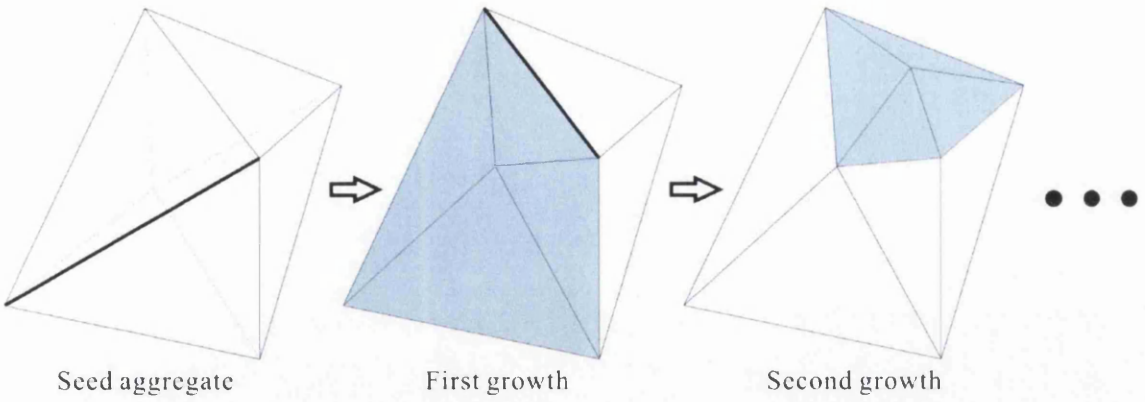

Figure 4.4: Growth of convex polyhedron aggregate from seed aggregate.

As illustrated in Fig.4.5, point a is a new randomly generated vertex from the common edge bd shared by triangular face m and n. The projection of point a on the edge bd denoted as point A is randomly generated in the same manner as growth of polygon aggregate. Then direction vector V_a is obtained by adding two unit outward normal V_m *and* V_n at the point a. The position of point a is obtained randomly along the direction vector V_a. To maintain a convex polyhedron, the volume V_k^a calculated from Eq.4.2 must be negative, where the index k denotes all triangular faces of the polyhedron apart from face m *and* n.

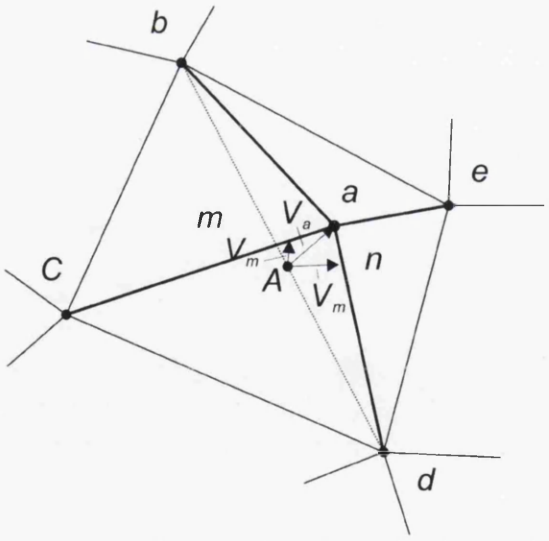

Figure 4.5: Formation of a new vertex for polyhedron aggregate.

4.2 Aggregate disposition procedure and overlap detection algorithm

In order to reproduce the aggregate structure of a particular specimen, the aggregate disposition procedure must satisfy the following requirements:

- Randomness of the aggregate distribution
- Reasonable aggregate grading
- Compatible and sufficiently high aggregate content

In this study, a convex aggregates disposition procedure base on take-and-place philosophy is adopted to optimize the computational cost and the maximum aggregate content. The overlap detection algorithm, such as area-based and volume-based methods, is computational expensive. Therefore, a more efficient algorithm, grid-based overlap detection algorithm, is developed and with minor modification the same concept can be extended to three dimensional applications. The algorithm utilizes a set of dense and uniform background grid of the disposition domain to detect the overlaps and a status matrix M_{ij} to store information at the each node. This algorithm is capable of generating both single-size and multi-size graded aggregate structure and the minimum and maximum value of each aggregate size range can be easily controlled. A pre-described grading curve and aggregate volume fraction can also be fitted and achieved precisely.

4.2.1 Background grid generation

Consider a $L \times W$ rectangular disposition domain as shown is Fig.4.6, and place a $n \times m$ uniform background grid to this domain. A status matrix $M\,(m \times n)$ is adopted to restore the status information of each node at all time during the disposition. The value of each node indicates that if this spatial location is occupied by aggregates.

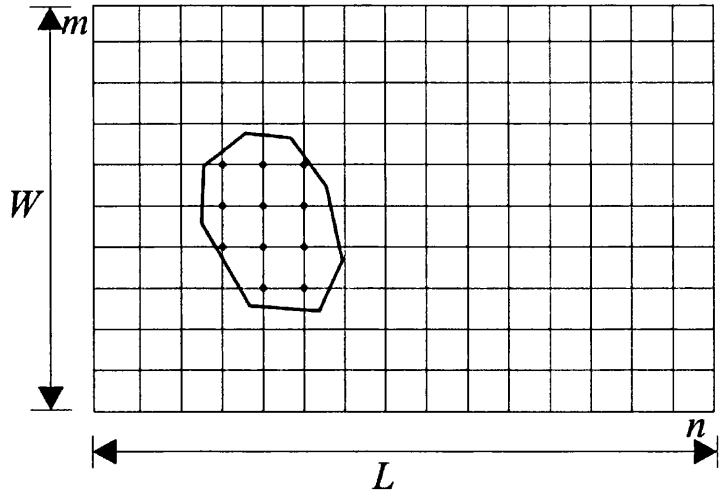

Figure 4.6: Schematic diagram of discretization of disposition domain into grid.

At the beginning of disposition, all elements of status matrix M_{ij} is initialized to 0 which indicates there is no aggregate in the disposition domain. As a new aggregate is placed and settled in the disposition domain, the status matrix is upgraded. As shown in Fig.4.6, the value of status matrix elements M_{ij} corresponding to the grid nodes within the aggregate is assign to 1. The status matrix keeps updated until the disposition is completed.

$$M_{ij} = \begin{cases} 0 & \textit{outside aggregates} \\ 1 & \textit{within an aggregate} \end{cases} \quad (0 < i \le m, 0 < j \le n) \tag{4.5}$$

A series of numerical simulation has been carried out to determine the optimum grid cell size. Our study suggests that the optimum grid cell size should be chosen at around 1/10 of the minimum aggregate diameter $D_{\min}^{agg}$ to 1/5 of the minimum aggregate diameter. Thus the number of rows and columns of status matrix should be chosen as follows:

$$\begin{aligned} 5W / D_{\min}^{agg} < m < 10W / D_{\min}^{agg} \\ 5L / D_{\min}^{agg} < n < 10L / D_{\min}^{agg} \end{aligned} \tag{4.6}$$

With minor modification the same theory can be extended to three-dimensional applications.

4.2.2 Grid-based aggregate overlap detection algorithm

Following the algorithms described in section 4.1.2, convex polygonal or polyhedral aggregates can been generated and stored in an aggregate database. A robust and effective algorithm to detect overlaps between convex aggregates is essential. As shown in Fig.4.7, the bold solid lines illustrate the settled aggregates and thin solid lines represent the aggregate to be deposited, the shaded areas denote the overlapping areas between aggregates and black dots on the grid lines correspond to status matrix elements with value 1. All the vertices, the centroid of polygon and the midpoints between them are defined as characteristic points.

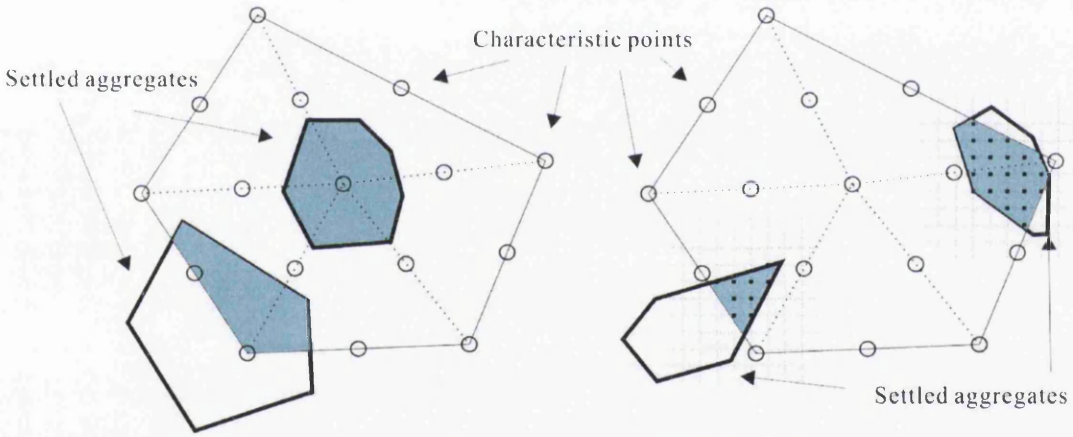

a) Initial determination-regular overlaps b) Detailed determination-complex overlaps

Figure 4.7: Aggregate characteristic points and overlap determination.

The overlaps between aggregates can be classified into two types: (1) Regular overlaps as shown in Fig.4.7a, where at least one characteristic point is included in the overlapping areas; (2) Complex overlaps as shown in Fig.4.7.b, where no characteristic point can be found in the overlapping areas. The algorithm is adopted to detect these two groups of overlaps is different from each other as computationally the regular overlaps are easier to deal with when compared to the complex overlaps.

Therefore, the detection algorithm is composed of two stages, namely initial determination and detailed determination.

Initial determination: after placing an aggregate at a random position in the disposition domain, the spatial locations of characteristic points can be obtained by the known vertices coordinates. Then associate each characteristic point with its nearest node and restore the corresponding value from the status matrix, if it is equal to 1 then it overlaps with at least one of the settled aggregate engaged, the aggregate is replaced to another random location in the disposition domain. If all corresponding elements in the status matrix are 0 then a successful initial disposition is obtained and it can proceed to the detail determination.

Detail determination: As shown in Fig.4.7b, characteristic points could not be detected in the overlapping area. Upgrade of the status matrix in the whole disposition domain is necessary. During the upgrade process, complex overlaps can be determinate if any status matrix element M_{ij} has already been assigned to 1 (as those black dots in Fig.4.7b, indicating the common grid points between settled aggregate and depositing aggregate). In this case, terminate detail determination and any update of status matrix elements will be abandoned. Otherwise a successful disposition is reached and the updated status matrix is saved.

One of the major benefits of this algorithm is that for most cases overlaps can be detected by only performing the initial determination and the complex overlap rarely appears. By taking this advantage the computation cost can be reduced significantly. Moreover, the detailed determination stage only requires calculations and updates of corresponding matrix elements of grids that surrounding the current aggregate.

4.2.3 Disposition algorithm according to size range

The algorithm is designed to produce both single-size graded or multi-size graded aggregate structures. Multi-size graded concrete is composed of a number of

aggregate size ranges and each size range occupies a certain percentage of the total aggregate volume. For a multi-size graded aggregate structure, in order to achieve a maximum aggregate volume fraction, the disposition starts with placing aggregate from the largest size range. The overall disposition algorithm can be described as follows and the flow chart is shown in Fig.4.8.

Stage 1: Generate random convex aggregate and store them into aggregate database. Discretize the disposition domain into grid and create a status matrix.

Stage 2: Take an aggregate from database which within the current size range and place the aggregate into random position within the disposition domain. Detect the possible overlap as described in section 4.2.2. If overlaps with previous aggregates are encountered, then relocate the aggregate in the translational direction and perform overlap detection again. Update the status matrix when aggregate disposition successful.

Stage 3: Calculate the aggregated volume fraction for the current size range, if the required aggregate volume fraction is not satisfied, repeat stage two. Otherwise, carry on disposition for the next size range.

Stage 4: Repeat the last three stages until the required aggregate volume fraction for all size ranges is satisfied.

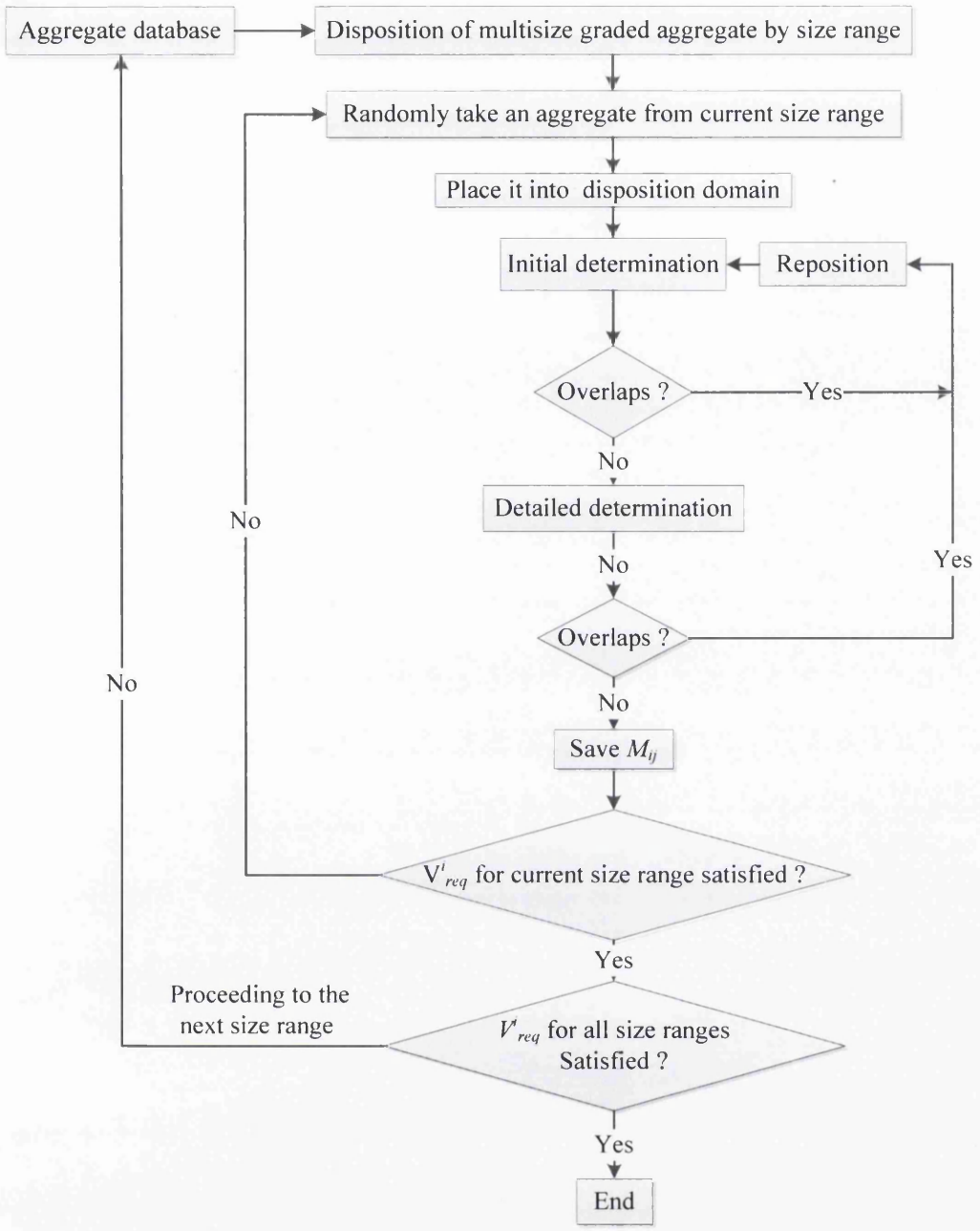

Figure 4.8: Disposition algorithm flow chart

4.3 Geometric model examples

The distribution of the diameters of aggregates in concrete mix space can be described as grading curve and Fuller curve has been widely adopted to achieve the optimum density gradation and strength. Their basic equation is:

$$P = \left(\frac{d}{D}\right)^n \tag{4.7}$$

where P is the percentage that finer than the sieve; d is the aggregate size being considered; D is the maximum aggregate size to be used; $n$is a parameter which adjusts the curve for fineness or coarseness (the maximum particle density $n \approx 0.5$)

However, in order to obtained a two-dimensional grading curve, an assumption has to be made for the distribution of the diameters of the intersection circles in a cross-section of a concrete body. On the basis of probability and statistics considerations, Walraven (Walraven and Reinhardt, 1981) derived a transformation formula from the Fuller aggregate size distribution below, representing the probability P_c that an arbitrary point in the concrete body, lying in an intersection plane, is located in an intersection circle with a diameter $D < D_0$:

$$P_c(D < D_0) = P_k\left[1.455\left(\frac{D_0}{D_{\max}}\right)^{0.5} - 0.5\left(\frac{D_0}{D_{\max}}\right)^{2} + 0.036\left(\frac{D_0}{D_{\max}}\right)^{4} + 0.006\left(\frac{D_0}{D_{\max}}\right)^{6} + 0.002\left(\frac{D_0}{D_{\max}}\right)^{8} + 0.001\left(\frac{D_0}{D_{\max}}\right)^{10}\right] \tag{4.8}$$

where $D_{\max}$ is the maximum aggregate diameter; P_k is the volume fraction of the aggregate. Subsisting volume fraction P_k, upper and lower limit of each aggregate size range into Eq.4.8 to computer the probability P_c of each size range appearing in an intersection plane, then two-dimensional grading curve can be obtained.

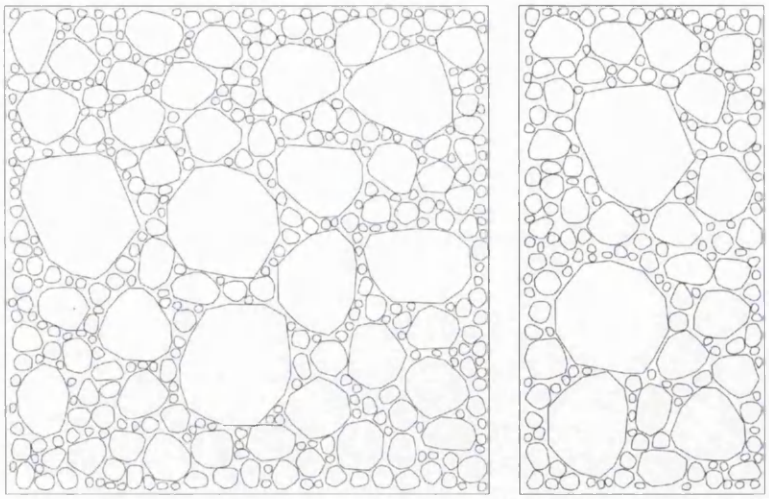

a) Square specimen b) Rectangular specimen

Figure 4.9: Two-dimensional aggregate structure geometric model.

Figs.4.9 and 4.10 illustrate the two-dimensional and three-dimensional aggregate structure geometric models generated by following the above algorithms. Up to 80% of aggregate volume fraction can be achieved in two-dimensional applications while up to 60% of volume fraction can be achieved in three-dimensional specimens.

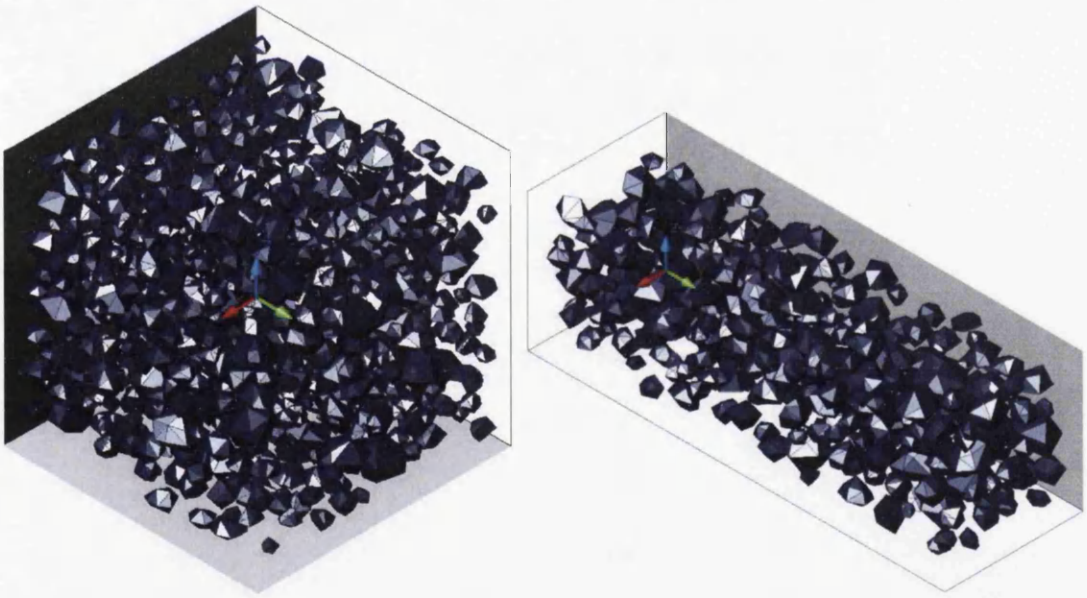

Figure 4.10: Three-dimensional aggregate structure geometric model.

4.3.1 Three-phase composition recognition for particle flow code

After discretizing the concrete as a rigid circular or spherical particle assembly that are bonded at their contact points and reproducing the aggregated structure of concrete material in statically sense, the particle assembly is projected on the top of the generated aggregate structure, different micro-parameters (i.e. strengths and stiffnesses) are assigned to the respective particle elements.

Firstly, the particle elements are distinguished as either rock element or matrix element according to their spatial locations; then the bond properties and contact model for each contact is distinguished by the category that the pair of particles in contact belong to. Finally, different values of micro-parameter and bond models can be assigned to the respective particles and bonds.

Assuming an arbitrary particle element with its centroid located at (x_i, y_i), if the value of corresponding element in the status matrix M_{ij} is equal to 1 (black dots in Fig.4.11) then the particle is classified as rock element, otherwise the particle is categorized as matrix element. Two rock element grains or two matrix element grains in contact form a rock bond or a matrix bond (black and green solid lines in Fig.4.11), while a rock element grain and a matrix element grain in contact form an interface bond (highlighted as red solid lines in Fig.4.11).

Fig.4.12 displays a three-phased cubic specimen that is sliced by a plane at its midpoint. The red colored particles represent the aggregate elements while the blue particles denote matrix elements. Fig.4.13 illustrates each phase within a two-dimensional three-phased discrete element model in detail.

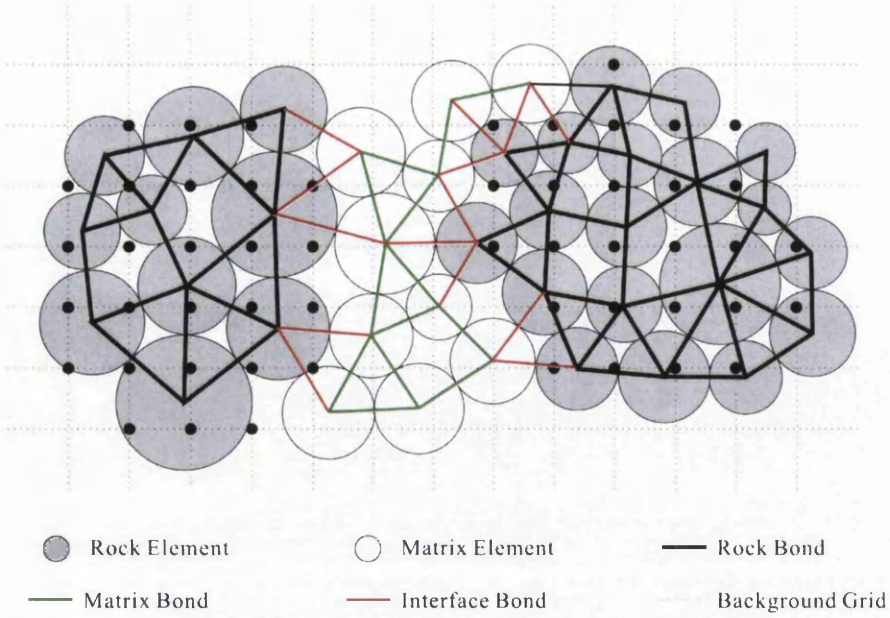

Figure 4.11: three-phase composition recognition for particle flow code.

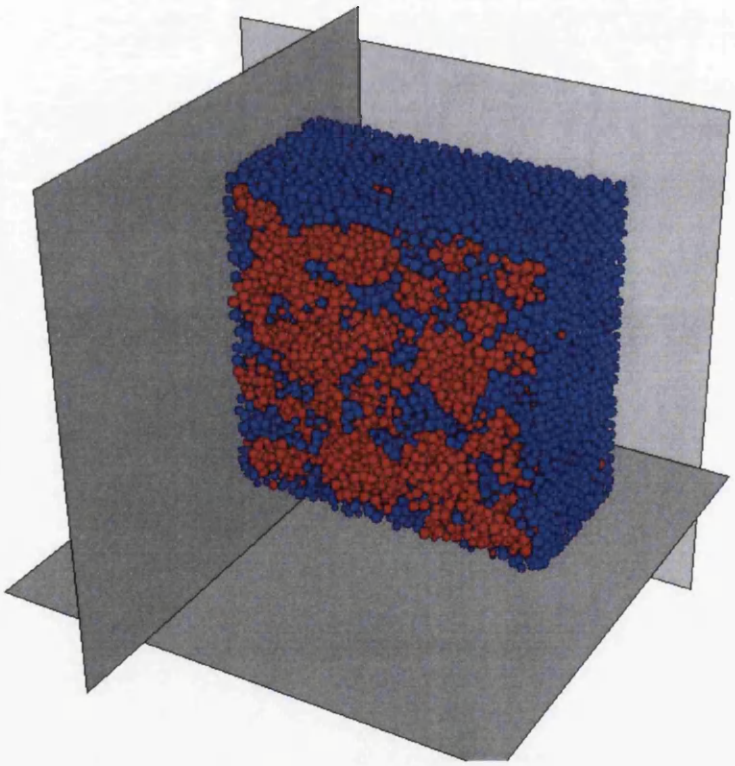

Figure 4.12: Three-dimensional three phased DEM model.

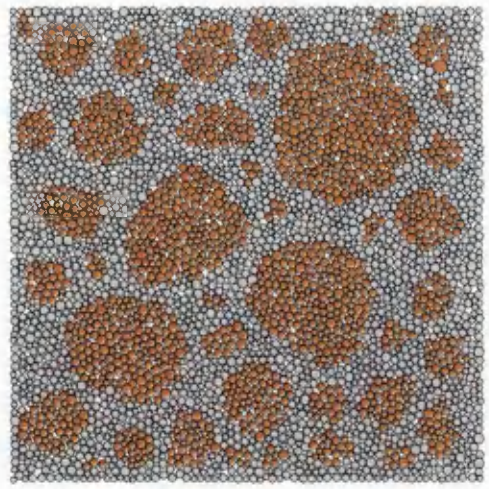

a) Three phased system

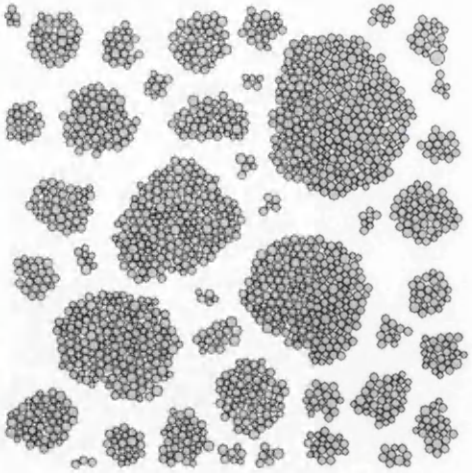

b) Aggregate element

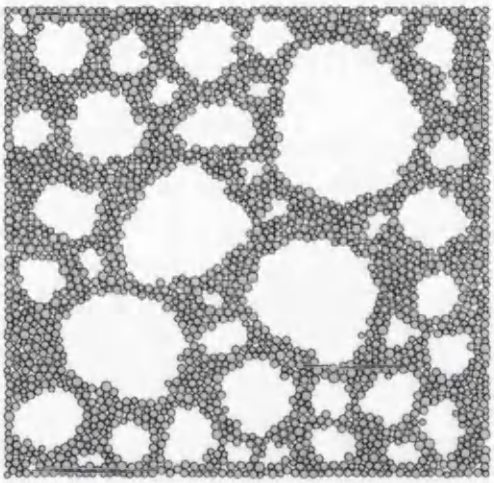

c) Matrix element

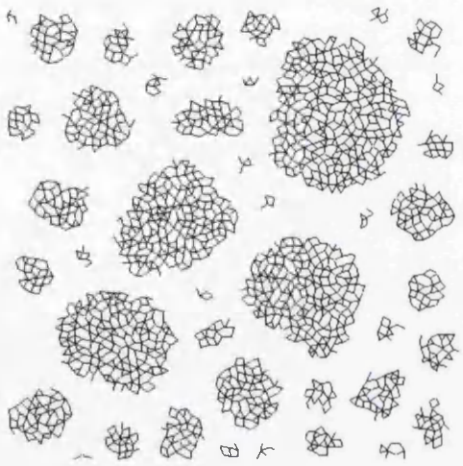

d) Aggregate contact

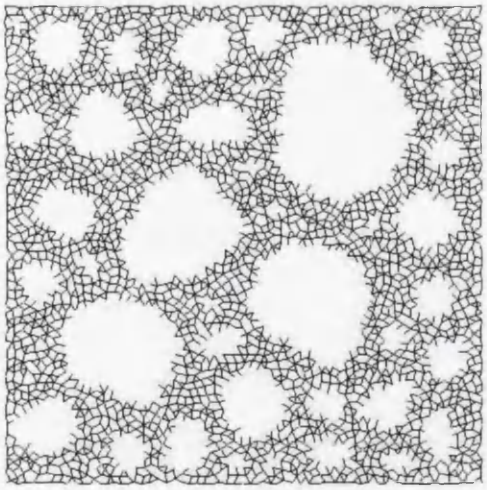

e) Matrix contact

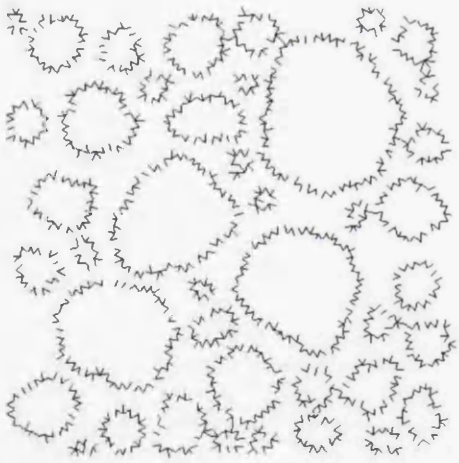

f) Interface contact

Figure 4.13: Two-dimensional DEM model of particles and contacts for each phase.

4.3.2 Effect of the degree of discretization

As shown in Figs.4.12 and 4.13, more or less detail may be lost when the size of the particles varies. Due to the computational limitations, a lower cut-off for the minimum particle size must be made. Therefore, chosen an appropriate degree of discretization in order to balance the results accuracy and computational efficient is significant. The ratio L/R, where L is the specimen characteristic length and R is particle average radius, is usually chosen as a measure of the degree of discretization.

A $100mm \times 100mm$ square specimen and a $100mm \times 100mm \times 100mm$ cubic specimen have been generated in order to study the effect of degree of discretization on the phase fraction. In the two dimensional analysis, the particle radius is uniformly distributed from the given minimum radius to the maximum radius and the radius ratio between both maximum and minimum particle radii is set to 1.66. On the other hand, the radius ratio is set to 1 which implies all particles have an identical radius. Fig.4.14 shows the variation of the different phases, 'aggregate', 'matrix' and 'interface', as a function of the degree of discretization.

From the results, we can see that for both two-dimensional and three-dimensional cases, the degree of discretization has a significant influence on the fraction of each phase. The fraction of aggregate particle and matrix particle remain almost constant as the degree of discretization varies. The slightly discrepancy is caused by the instability of low degree of discretization. The fraction of interface bond decreases as the degree of discretization increases and the fraction of pure aggregate and matrix bond increases. It can be expected that fraction of each phase will converge to a certain value where the degree of discretization becomes large enough.

Since different values of micro-parameter and bond models will be assigned to each phase, attention should be paid to the selection of specimen size and particle radius. It has been noted that when the degree of discretization is low, the numerical results

become unstable. Further discuss regarding the effect of degree of discretization will be conducted in the later chapters.

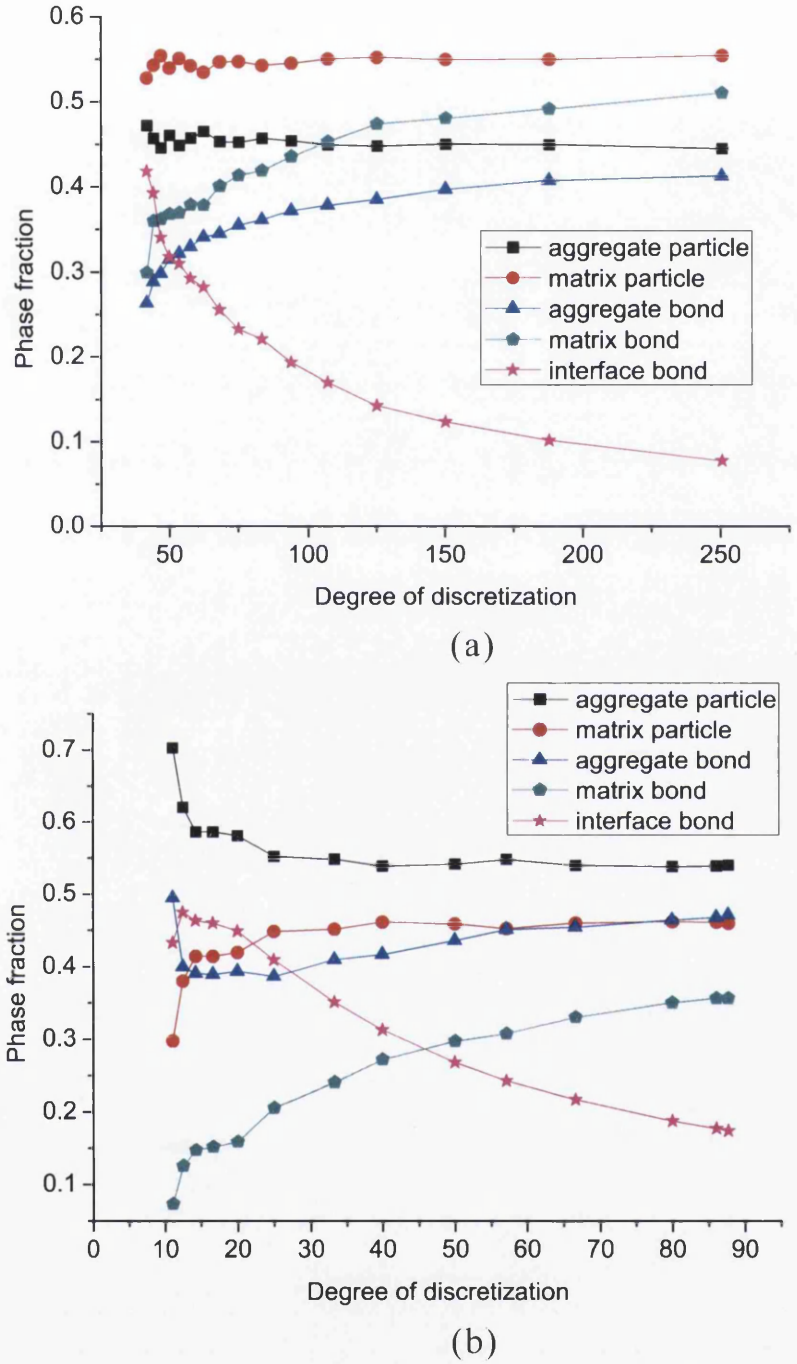

Figure 4.14: Phase fraction verse degree of discretization.

4.4 Numerical tests

A number of numerical tests are conducted to demonstrate the efficiency of this algorithm; and to perform a parametric study of the algorithm itself. The problem domains are chosen to be square (2D) and cubic (3D). Aggregate structures of both specimens are multi-size graded and include four size ranges and the upper and lower limits for each aggregate size range are shown in table 2.1. The area or volume fraction ratio between the different size ranges is 2:2:3:3. All the results are obtained on an Intel (R) Core (TM) i5-2410M CPU @ 2.30GHz with 4GB RAM.

Table 4.1 Upper and lower limits for each aggregate size range

Size range (mm)							
1		2		3		4	
Minimum	Maximum	Minimum	Maximum	Minimum	Maximum	Minimum	Maximum
4	8	8	16	16	32	32	64

First, the CPU costs for the random convex aggregate generator algorithm is study. The number of aggregates generated is controlled by specifying the required area or volume for each size range. The numerical results are shown in Figs.4.15 and 4.16.

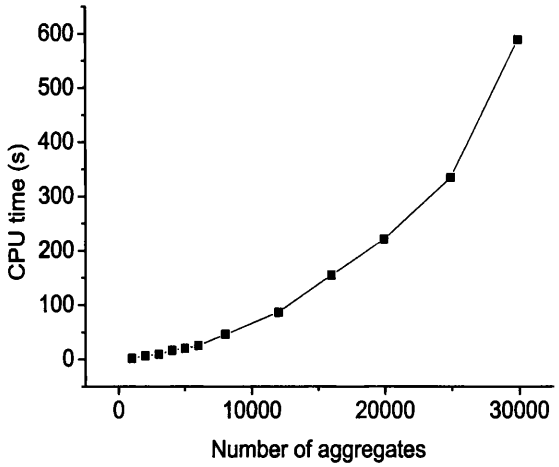

Figure 4.15: CPU time verse number of aggregates for two-dimensional case.

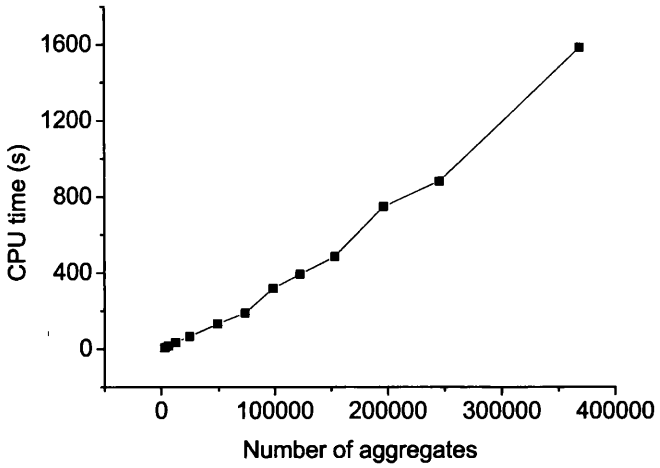

Figure 4.16: CPU time verse number of aggregates for three-dimensional case.

As expected the algorithm is sensitive to the number of aggregate required. A larger number of aggregate leads to a higher CPU time. Regression analysis indicates that the tendency of two-dimensional and three-dimensional curves can be described as third and second order polynomial functions respectively.

This algorithm is capable of achieving an aggregate volume fraction up to 80% and 60 % for two and three dimensional application respectively. However, the probability of successful disposition and CPU costs are affected by the required aggregate volume fraction. A set of numerical tests are conducted to demonstrate the aggregate volume fraction influences on probability of successful disposition. The disposition procedure is performed 50 times for each selected aggregate area or volume fraction. The results are illustrated in Figs.4.17 and 4.18.

From Fig.4.17, we can see that 100% success rate can be guaranteed when the aggregate area fraction is less than 70%. Success rate starts decreasing when aggregate area fraction reaches 70% benchmark and falls dramatically beyond 80% of the targeted maximum aggregate area fraction. Similar results can be observed from three-dimensional disposition outcomes. Success rate begins to reduce at 50% and descends sharply beyond 60% of the maximum achievable aggregate volume fraction.

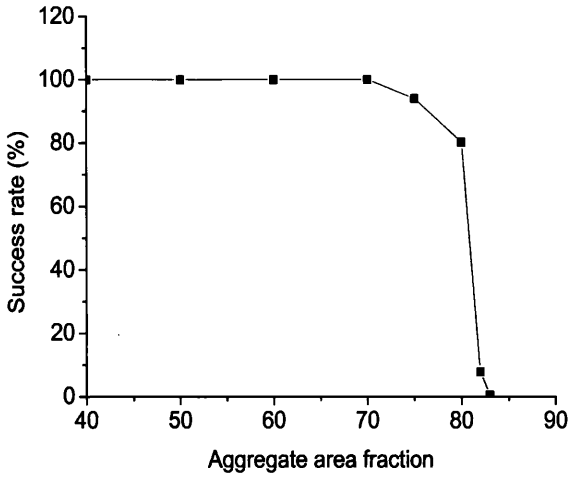

Figure 4.17: Success rate verse aggregate area fraction.

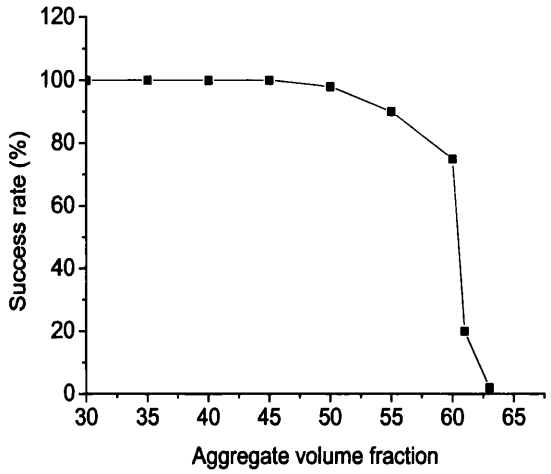

Figure 4.18: Success rate verse aggregate volume fraction.

Different sized specimens have been generated to investigate the CPU costs of deposition algorithm at various aggregate area or volume fractions. Three cubic specimens with edge length 300 *mm*, 400 *mm* and 500 *mm* have been investigated. CPU costs have been recorded at the chosen aggregate area fraction (40%, 50%, 60%, 70% and 80%). The same approach applied to three-dimensional CPU costs analyses. Two different sized specimens (100 *mm* and 150 *mm*) and six volume fraction points for each specimen have been inspected. The results are shown in Figs.4.19 and 4.20.

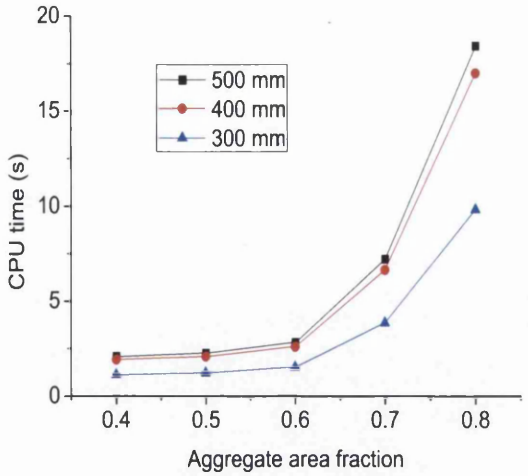

Figure 4.19: Deposition CPU costs verse aggregate area fraction.

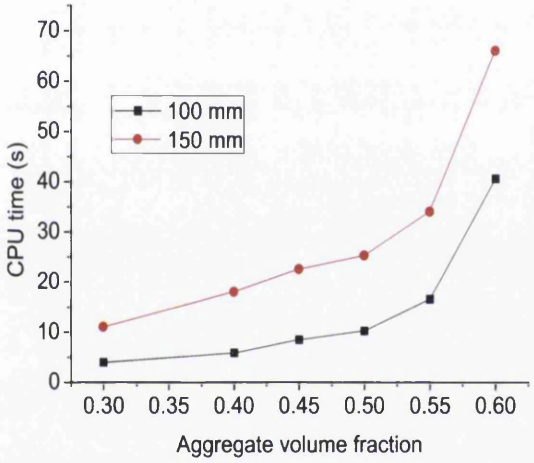

Figure 4.20: Deposition CPU costs verse aggregate volume fraction.

The results above indicate that the CPU time required for the disposition procedure is affected by both designed aggregate fraction and specimen size. Three dimensional applications require much more computation resources than two dimensional cases although similar results can be found. The CPU costs increases as the required aggregate fraction and specimen size increase since more aggregates need to be placed.

4.5 Conclusions

In this chapter a preprocessing procedure for discrete element modeling of three-phased concrete material has been reviewed. The preprocessor was capable of producing up to 80% (2D) and 60% (3D) aggregate fraction specimens. The multi-size graded concrete aggregate structure also can be well obtained. Numerical examples and parametric studies have proven the algorithm was computationally efficient and effective.

The preprocessor adopted the 'take-and-place' approach and could be subdivided into three stages: aggregate generator, aggregate disposition and phase recognition. Status matrix played a major role throughout different stages and by integrating with domain background grids the computational time could be significantly reduced. The phase recognition was a straight forward approach as hardly any calculation is required. However, the fraction of each phase was affected by the degree of discretization of discrete element model. The fraction of the weakest link interfacial zone decreases as the degree of discretization increases. Since different values of micro-parameter and bond models will be assigned to each phase, attention should be paid to the selection of specimen size and particle radius.

Parametric studies of the algorithm itself indicated that the CPU time for both aggregate generator and disposition procedure were governed by the number of aggregates. High disposition success rates can be guaranteed before the maximum aggregate fraction is achieved.

When compared with other similar purposed algorithms, the clear advantages of the proposed algorithm include:

- Higher aggregate fraction achieved.
- More realistic aggregate distribution by utilizing multi-size graded disposition.
- Lower computational costs.

References

Bažant, Z., Tabbara, M., Kazemi, M., Pijaudier - Cabot, G., 1990. Random particle model for fracture of aggregate or fiber composites. Journal of Engineering Mechanics 116, 1686–1705.

Beddow, J.K., Meloy, T., 1980. Testing and characterization of powders and fine particles, London: Heyden.

British Standards Insitution, 2009. PD 6682-1:2009 Aggregates for concrete. Guidance on the use of BS EN 12620. British Standards Insitution, London.

De Schutter, G., Taerwe, L., 1993. Random particle model for concrete based on Delaunay triangulation. Materials and Structures 26, 67-73.

Gao, Z.G., Liu, G.T., 2003. Two-dimentional random aggregate structure for concrete. JOURNAL OF TSINGHUA UNIVERSITY(SCIENCE AND TECHNOLOGY) 43, 710-714.

Häfner, S., Eckardt, S., Luther, T., Könke, C., 2006. Mesoscale modeling of concrete: Geometry and numerics. Computers & Structures 84, 450-461.

Kim, H., Buttlar, W.G., 2009. Discrete fracture modeling of asphalt concrete. International Journal of Solids and Structures 46, 2593-2604.

Lehmer, D.H., 1951. Mathematical methods in large-scale computing units, Proceedings of a Second Symposium on Large-Scale Digital Calculating Machinery, 1949. Harvard University Press, Cambridge, Mass., pp. 141--146.

Leite, J.P.B., Slowik, V., Mihashi, H., 2004. Computer simulation of fracture processes of concrete using mesolevel models of lattice structures. Cement and Concrete Research 34, 1025-1033.

Liu, G.T., Gao, Z.G., 2003. Random 3-D aggregate structure for concrete. J Tsinghua Univ (Sci Tech) 43, 1120-1123.

Mungule, M., Raghuprasad, B.K., 2011. Meso-scale studies in fracture of concrete: A numerical simulation. Computers & Structures 89, 912-920.

Schalangen, E., J.G.M. van Mier, 1994. Simple lattice model for numerical simulation of fracture of concrete materials and structures. Materials and Structures 25, 534-542.

Schorn, H., Rode, U., 1991. Numericalsimulation of crackpropagation from microcracking to fracture. Cement and Concrete Composites 13, 87-94.

Tang, X., Zhang, C., Shi, J., 2009. A multiphase mesostructure mechanics approach to

the study of the fracture-damage behavior of concrete. Science in China Series E: Technological Sciences 51, 8-24.

Taussky, O., Todd, J., 1956. Generation and testing of pseudo-random numbers, Symposium on Monte Carlo methods, University of Florida, 1954. John Wiley and Sons, Inc., New York, pp. 15--28.

Vervuurt, A., 1997. Interface fracture in Concrete. TU Delft.

Walraven, J.C., Reinhardt, H.W., 1981. Theory and Experiments on the Mechanical Behaviour of Cracks in Plain and Reinforced Concrete Subjected to Shear Loading. Stevin-Laboratory of the Department of Civil Engineering.

Wang, Z.M., Kwan, A.K.H., Chan, H.C., 1999. Mesoscopic study of concrete I: generation of randomaggregate structure and finite element mesh. Computers & Structures 70, 533-544.

Wittmann, F.H., Roelfstra, P.E., Sadouki, H., 1985. Simulation and analysis of compositestructures. Materials Science and Engineering 68, 239-248.

Yang, W.G., Xiang, H.J., 2012. A new approach for the simulation of cementitious materials. Journal of Mechanical Science and Technology 26, 45-51.

Chapter 5

Parametric study of parallel bonded DE model in compression – Experimental and specimen geometric and physical parameters

In this research, the particle based discrete element approach adopted utilizes a collection of rigid particles which are bonded together at their contact points to simulate the behaviour of concrete material. However, unlike the continuum approach, such as FEM, input parameters for the discrete particle assembly are unknown in advance. The discrete element model is impressionable to the input micro-parameters values and accurate results only can be obtained if the correct relationship between micro-parameters and macro-properties are specified. To determinate the proper input micro-parameters becomes one of the main challenges in the field of particle approaches.

Despite the previous research done in the field of parameter calibration, most studies have been carried out to evaluate the Young's modulus, Poisson's ratio and ultimate strength for application of rock (Fakhimi and Villegas, 2006; Yang *et al.*, 2006; Yoon, 2007). Limited information is available regarding effects of specimen size and geometry, test conditions and micro-parameters on the failure and post-peak characteristic of concrete material. In the literature available, to the best knowledge of

author, 3D micro-parameters study and comparison with 2D parameter calibration have not been reported.

The next two chapters aim to investigate the effects of constitutive and physical parameters on the macro response of synthetic material. The brittle contact and bond model is adopted in this research rather than the softening model as Van Mier (Van Mier, 2004) suggested that adopting the softening contact model may hide important features if the main interest is to study fracture mechanisms. The parallel bond model as originally proposed by Potyondy and Cundall (Potyondy and Cundall, 2004) is used to glue particles together. Then uniaxial compression test is performed to investigate effect of each parameter.

The parametric study is carried out by utilizing widely used commercial software particle flow code (PFC2D/3D). Both two and three dimensional simulations are performed simultaneously to enable comparison study of possible different relations between micro-parameters and macro-properties. It should be noted that the two dimensional elastic constants are obtained by assuming the plane strain condition.

In this chapter, effects of experimental and specimen geometric and physical parameters (loading velocity, degree of discretisation and particle size distribution) are investigated by performing a series of numerical uniaxial compressive tests.

5.1 Parameters and dimensional analysis

Due to the lack of a complete theory, if it is possible, to predict the macro response of particle assembly, Huang (Huang, 1999) and Yang (Yang *et al.*, 2006) proposed scaling law between micro-parameters and macro-properties for contact bond and parallel bond model respectively using PFC2D. The determination of scaling law consists of dimensional analysis and performing numerical simulations of laboratory test.

Huang characterized a discrete particle assembly with contact bonds into two groups at micro-scale: Specimen geometric and physical parameters, i.e. average disc radius, density $\rho[FL^{-1}T^2]$ and porosity n, and constitutive parameters, i.e. normal stiffness $K_n[FL^{-2}]$, normal strength $T_n[FL^{-1}]$, shear stiffness $K_s[FL^{-2}]$, shear strength $T_s[FL^{-1}]$ and friction coefficient μ. By assuming quasi-static loading condition and simulation with large degree of discretization, the set of numbers governing the elastic constants and failure of the specimen under uniaxial loading reduces to:

$$\begin{aligned} E &= K_n \Phi_E\left(\frac{K_s}{K_n}, n\right) \\ \nu &= \Phi_\nu\left(\frac{K_s}{K_n}, n\right) \\ \sigma_c &= T_n \Phi_c\left\{\frac{K_n R}{T_n}, \frac{T_s}{T_n}, \mu, \frac{K_s}{K_n}, n\right\} \end{aligned} \tag{5.1}$$

Yang (Yang *et al.*, 2006) argues that the particle assembly porosity n is not an appropriate index to represent the particle size distribution. As the porosity of particle assembly generated in particle flow code is independent of particle size distributions. Indeed, the particle size distribution is controlled by specifying the upper and lower particle radius ($R_{\max}$ *and* $R_{\min}$) then particle size distributed uniformly over the specified range, therefore, particle radius ratio $(R_{\max}/R_{\min})$ is more appropriate parameter to represent particle size distribution effect.

Size effect will eventually diminish when model degree of discretization becomes sufficiently large. However, the particle size of DEM model cannot be chosen too small due to the limitation of computation cost. Additionally, specimen cracks are represented by the breakage of particle bonds, initiation and propagation of cracks and final damage pattern exhibit clear size dependence. In order to determine the optimum model resolution, investigation on the particle and specimen size effect is conducted by

considering L/R (L is specimen characteristic length and R is average particle radius) as a measurement of degree of discretization.

Comparing to contact bond model, more micro constitutive parameters are involved in a parallel bond model, i.e. bond normal and shear stiffness $\bar{k}_n$ and $\bar{k}_s$ $[F/L^3]$, bond normal and shear strength $\bar{\sigma}_c$, $\bar{\tau}_c$ $[F/L^2]$, and bond radius $\bar{R}$ $[L]$. Modulus-stiffness scaling relations described in Eq.3.38 relate the grain and bond normal and shear stiffness to grain and bond contact modulus E_c and $\bar{E}_c$ (F/L^{-2}). Bond modulus and stiffness ratio are often set equal to grain modulus and stiffness to simplify calibration process (Lei, 2003; Potyondy and Cundall, 2004). Their works have demonstrated that this simplification was an efficient approach to reproduce the behaviour of rock-like material. The bond width $\bar{R}$ has a significant effect on the stress-displacement relationship at a macroscopic level, and the bond radius is defined by radius multiplier ($\bar{\lambda}$) as in Eq.3.40.

Another difference between contact bond and parallel bond arises from the effect of particle friction. Unlike contact bond model where the particle friction affects only post-peak response (Potyondy and Cundall, 2004) . Once a contact bond between two touching particles breaks, then slip model is activated and the slip model is only governed by particle friction. The parallel-bond model, on the other hand, slip model is active in conjunction with the bond model. For this reason the friction effect in parallel bond model increases the shear resistance relative to the contact bond and may also prevent microshear failure.

Based upon the contact model and loading path we adopted in this study, prior to any bond failure, the set of parameters involved in the response of the synthetic material are $\left\{k_n, k_s, R, \frac{R_{\max}}{R_{\min}}, \rho, L, V, \bar{\lambda}, \mu\right\}$ .After dimensional analysis and assuming quasi-static loading condition, the following scaling law for material elastic constants can be obtained:

$$E = E_c \Phi_E \left(\frac{k_n}{k_s}, \frac{L}{R}, \frac{R_{\max}}{R_{\min}}, \mu, \bar{\lambda}\right) \tag{5.2}$$

$$\nu = \Phi_\nu \left(\frac{k_n}{k_s}, \frac{L}{R}, \frac{R_{\max}}{R_{\min}}, \mu, \bar{\lambda}\right) \tag{5.3}$$

The failure of particle assembly is controlled by $\left\{k_n, k_s, \bar{\tau}_{b,m}, \bar{\sigma}_{b,m}, \mu, R, \frac{R_{\max}}{R_{\min}}, \rho, L, V, \bar{\lambda}\right\}$ and scaling law for compressive strength is illustrated as following:

$$\sigma_c = \sigma_{b,m} \Phi_c \left(\frac{E_c}{\sigma_{b,m}}, \frac{\tau_{b,m}}{\sigma_{b,m}}, \mu, \frac{k_n}{k_s}, \frac{L}{R}, \frac{R_{\max}}{R_{\min}}, \bar{\lambda}\right) \tag{5.4}$$

5.2 Numerical test of uniaxial compression and selection of benchmark parameters

By far the most common laboratory test carried out on concrete is the uniaxial compressive test because it is easy and inexpensive to perform.

Figure 5.1: Uniaxial compression test model set-up and specimen dimension.

Figure 5.1 shows the model setup for uniaxial compression test and discrete element discretisation. The loading platens are modeled as rigid wall segments and the top and

bottom platens move towards each other at the identical velocity. The loading velocity must be low enough to satisfy the quasi-static condition. Detailed discussion of the dynamic influence caused by large strain rate is conducted in section 5.3. The model is heavily damped by setting a large damping coefficient equal to 0.7. Stiffness of the loading platens is defined as a fraction of the average particle stiffness. The loading platens are accelerated from 0 to their final velocity in a controlled fashion in order to produce a stable microproperties response. The specimens are represented by a random packing of non-uniform-sized circular or spherical particles that are bonded together at their contact points by parallel bond and porosity of this particle assemblies generated in particle flow code are 16% and 36%.

Table 5.1 indicates microparameters selected to match macroproperties of concrete. Those mircoparameters are chosen to be the reference data and when investigating effects of specific parameters, only the investigated parameter is changed while others keep unchanged.

Table 5.1: Reference Micro-parameters for calibration.

Parameters	Symbol	2D	3D
Specimen length (mm)	L	200	100
Specimen width (mm)	W	100	100
Specimen height (mm)	H	0	100
Wall friction coefficient	μ_w	0	0
Minimum particle size (mm)	$R_{\min}$	0.631	2
Particle size ratio	$R_{\max} / R_{\min}$	1.66	1.66
Particle density (kg/m^3)	ρ	2400	2400
Particle contact modulus (GPa)	E_c	20	19
Particle stiffness ratio	k_n / k_s	2	1.4
Particle friction coefficient	μ	0.5	0.5
Parallel-bond radius multiplier	$\bar{\lambda}$	1	1
Parallel-bond modulus (GPa)	$\bar{E}_c$	20	19
Parallel-bond stiffness ratio	$\bar{k}_n / \bar{k}_s$	2	1.4
Parallel-bond normal strength, mean (MPa)	$\sigma_{b,m}$	18	27
Parallel-bond normal strength, standard deviation (MPa)	$\sigma_{b,std}$	2	4
Parallel-bond shear strength, mean (MPa)	$\tau_{b,m}$	36	54
Parallel-bond shear strength, standard deviation (MPa)	$\tau_{b,std}$	4	8

5.3 Effect of experimental parameter (loading velocity)

In order to obtained quasi-static loading condition, determination of the appropriate loading velocity is critical. Strain rate, defined as the rate of change in strain with respect to time, is commonly used when material is subject to dynamic load. In a conventional displacement-controlled experiment, the strain rate is defined as the ratio of the velocity of the loading platen and the specimen height along the loading direction:

$$\dot{\varepsilon} = \frac{v_p}{2H} \tag{5.5}$$

Bischoff and Perry (Bischoff and Perry, 1995) studied the dynamic behavior of plain concrete by performing uniaxial compression tests and summarized regimes of strain rate as Figure 5.2.

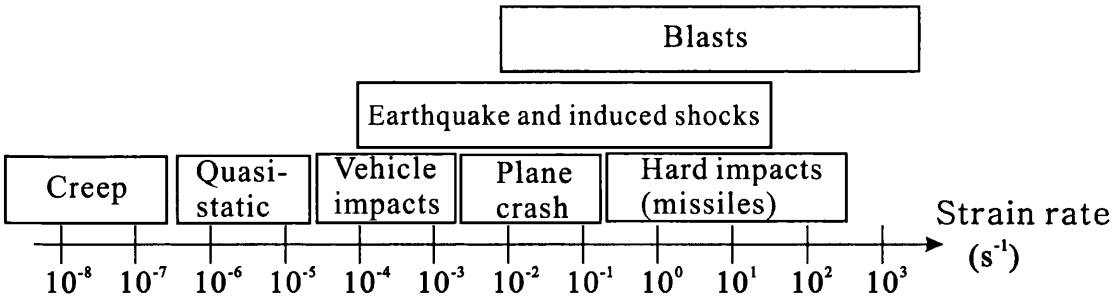

Figure 5.2: Regimes of strain rate (Bischoff, 1991).

When concrete material is subjected to high strain rates, the apparent strength of concrete can increase significantly. The dynamic increase factor (DIF), i.e. the ratio of the dynamic to static strength, is normally reported as a function of strain rate. For concrete, the dynamic increase factor can be more than 2 in compression, and more than 6 in tension. The DIF formulation for concrete in compression has widely been accepted by most researchers, and is presented by the CEB Model Code (Comité Euro-International du Béton, 1993). Direct applications in numerical analysis (Bischoff, 1991; Fu, December 1991; Malvar, December 1997; Williams, March-April 1994) have showed that it was an accurate representation of actual behaviour. The formulation is given as follows:

$$\frac{f_c}{f_{cs}} = \begin{cases} \left(\dfrac{\dot{\varepsilon}}{\dot{\varepsilon}_s}\right)^{1.026\alpha} & \dot{\varepsilon} \le 30s^{-1} \\ \gamma_s \left(\dot{\varepsilon}\right)^{\frac{1}{3}} & \dot{\varepsilon} > 30s^{-1} \end{cases} \tag{5.6}$$

where f_c = dynamic compressive strength at $\dot{\varepsilon}$

f_{cs} = static compressive strength at $\dot{\varepsilon}_s$

f_c / f_{cs} = compressive strength dynamic increase factor (DIF)

$\dot{\varepsilon}$ = strain rate in the range of $30 \times 10^{-6} s^{-1}$ to $300\ s^{-1}$

$\dot{\varepsilon}_s = 30 \times 10^{-6}\ s^{-1}$ (static strain rate)

$\log \gamma_s = 6.156\ \alpha^{-2}$

$\alpha = 1/(5+9\ f_{cs} / f_{co})$

$f_{co} = 10$Mpa

As prescribed displacement loading is adopted in this research, the influence of the loading velocities is performed by comparing the stress strain curves and the distribution of the contact force chain obtained at different strain rates.

5.3.1 Stress-strain curve

The results in Figure 5.3 show that the uniaxial compressive strength increases as the strain rate increases. Static compressive strength can be reproduced when the strain rate is less than 0.1 which corresponds to the wall velocity 0.01 m/s. When the strain rate is as low as 0.01/s, the macro-failure of synthetic material occurs immediately beyond the peak stress, resulting in a brittle failure process. Increasing the strain rate the failure becomes more ductile. It is found that, as the strain rate decreases the specimen behaviors more close to the local constitutive law for the individual bonds. It is reasonable to argue that the ideal static loading condition can be obtained under strain rate value 0.1/s.

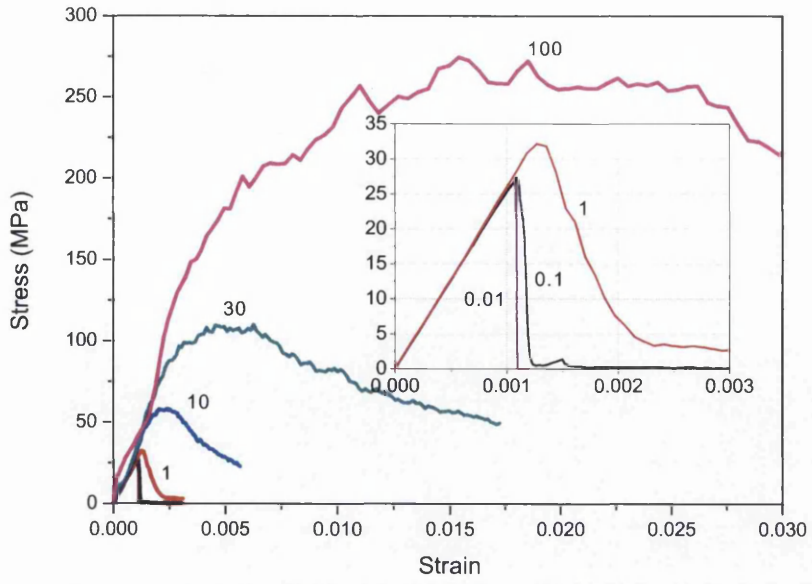

Figure 5.3: Simulation stress strain curve at different strain rate.

5.3.2 Contact force fabric

In the discrete element approach the concept of the force fabric at the macro-level is a transmission path of the external load in the specimen. At meso-level it is a chain structure created by connecting contact force between particles in contact. As shown in Figure 5.4, the black lines denote the contact forces between particles and the thickness of the line represents magnitude of contact force.

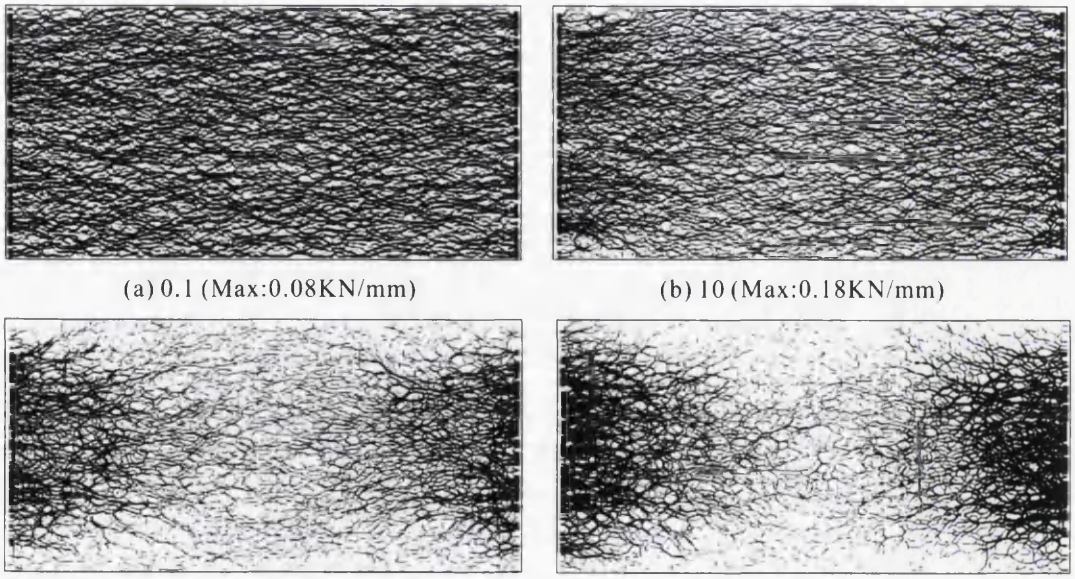

(a) 0.1 (Max:0.08KN/mm) (b) 10 (Max:0.18KN/mm)

(c) 30 (Max:0.64KN/mm) (d) 100 (Max:1.52KN/mm)

Figure 5.4: Contact force chain at different strain rate.

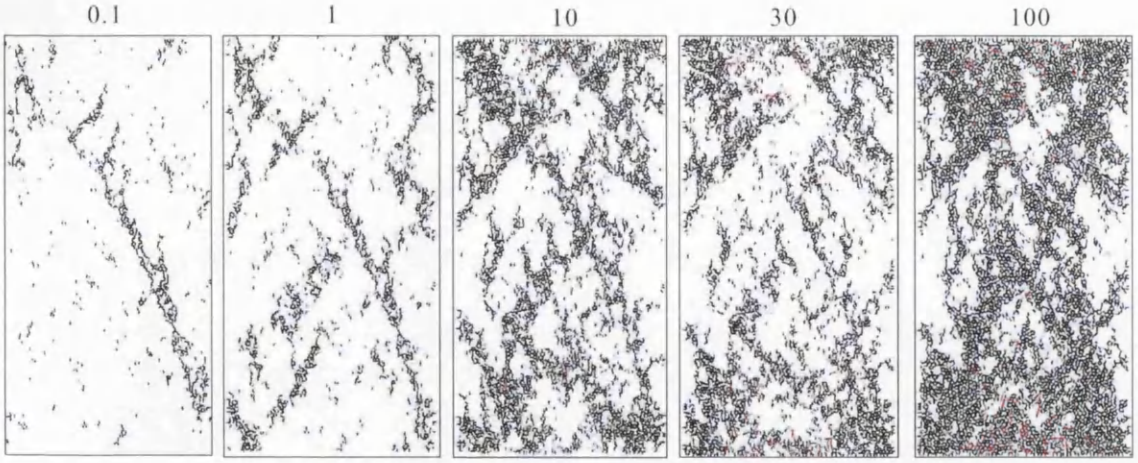

Figure 5.5: Cracks distribution at peak stress for different strain rate.

As the strain rate increases the maximum force increases. When the strain rate is lower than 0.1/s, the maximum force remains constant. When the strain rate value exceeds 10/s the maximum contact force increases dramatically. The force chain distribution becomes increasingly nonuniform with the increased strain rate and the damage is eventually highly localized at the two ends of specimen, as in Figure 5.5.

5.3.3 Dynamic increase factor

It can be predicted that the dynamic behavior of model material exhibits particle size dependence, as the size of time step is related to the minimum particle radius in the system. Three different models consisting of 7589, 1994 and 511 particles are generated then each specimen is loading under strain rate varying from 0.01/s to 100/s. The resultant dynamic increase factor (D.I.F.) observed is shown in Figure 5.6.

Higher dynamic increase factors are found when finer model resolutions are used. Comparing to the value obtained from the empirical CEB formula, the model dynamic increase factor is slightly lower in the range of 0.01/s to 0.1/s. In the range of 1/s to 10^2/s, the coarse model appears to be more close to the CEB formulation and experimental data (Malvern *et al.*, 1985).

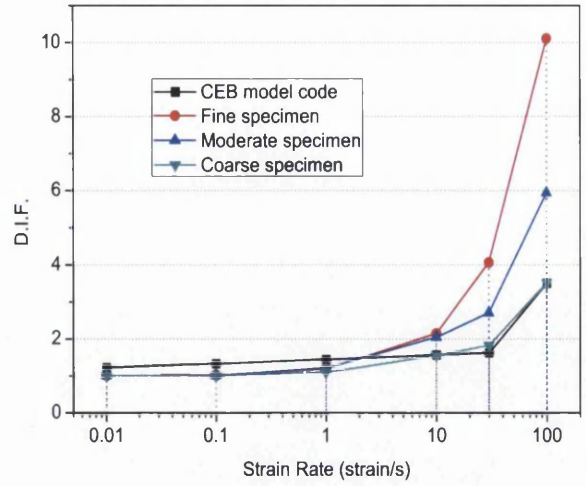

Figure 5.6: Dependence of dynamic increase factor on model resolution.

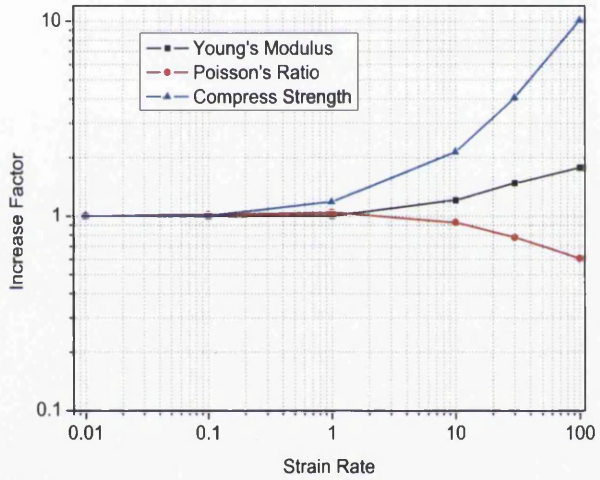

Figure 5.7: Variation of material deformability for different strain rate.

Figure 5.7 indicates that not only the compressive strength of model material increases with increase strain rate, both Young's modulus and the Poisson's ratio vary significantly but at lower intensity than the compressive strength which is in good agreement with experimental findings by Bischoff (Bischoff, 1991). Up to 80% increase of Young's modulus and 40 % decrease of the Poisson's ratio can be found. The major turning point is around strain rate 1/s.

Figure 5.8 demonstrates the different intensity of rate dependence for 2D and 3D models obtained by keeping the model resolution at a constant level. All three measured material properties of 2D models exhibit more intense rate dependence than 3D models

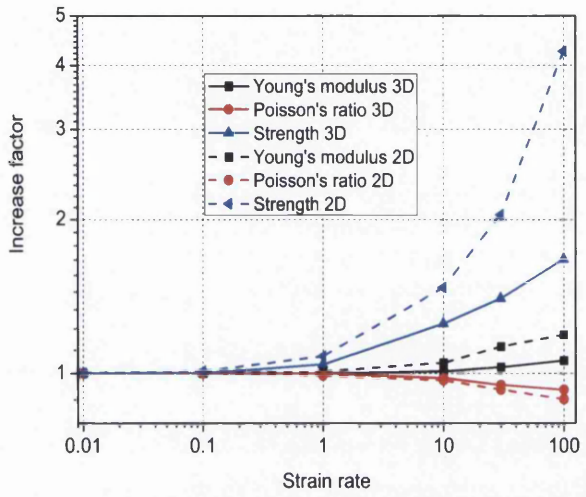

Figure 5.8: Comparison of increase factors between 2D and 3D model.

Based upon the above analysis, extensive calibration and attention must be paid when utilizing PFC to perform dynamic simulation. Our attention mainly focus on finding an appropriate loading velocity to obtain static behavior and all three results indicate that when the strain rate value is as low as 0.1/s the measured macro-properties change as little as 2%, therefore, in this research strain rate 0.1/s is adopted which in our case the opposite wall move towards each other at 0.01m/s.

5.4 Effect of specimen geometric and physical parameters

5.4.1 Degree of discretisation

Huang (Huang, 1999) utilized commercial software PFC^{2D} (particle flow code) to study the scaling-law between micro-parameters and macro-properties of contact-bond model. The ratio L/R was used as a measure of the degree of discretization and

concluded that the particle size has little effects on the macro material response during uniaxial compression test while L/R is large enough.

Yang(Yang *et al.*, 2006) performed similar analysis by adopting parallel bond and argue that when L/R smaller then 80, the Young's modulus and Poisson's ratio are effected significantly but the compressive strength is hardly affected.

Nardin (Nardin A, 2005) obtained a similar scaling-law using self-defined bonding model and found that uniaxial compressive strength increases when L/R is small.

Potyondy (Potyondy and Cundall, 2004) also performed particle size effect analysis by simulating biaxial and triaxial tests at confinements of 0.1 and 10 MPa. The Poisson's ratio and compressive strength appeared to be independent of particle size and Young's modulus increased slightly (less than 5 %) as particle size decreased. However in the literature only a small L/R range (11, 22, 44, 88 for biaxial tests) has been covered in the their study.

Koyama and Jing (Koyama and Jing, 2007) scrutinized the particle size effect utilizing a stochastic representative elementary volume (REV) of particle assemblies in a statistical manner. According to their research, there are certain thresholds of both particle size and particle size distribution that are material dependent, hence care should be paid to determine a suitable particle size and its distribution.

All above mentioned researcher were based on two dimensional simulation of the rock material. The characteristic behaviors of three dimensional models could be different (e.g. one extra dimension increases anisotropy of numerical model).In this study, two and three dimensional investigations of effect of model resolution on material elastic constants and ultimate strength are carried out simultaneously over a wide range of L/R(20-240 for 2D and 10-90 for 3D). Both approaches to vary the ratio L/R, changing specimen size (Case I) and particle size (Case II), are considered. By changing the random seed, 20 randomly packed particle assemblies for each specimen

are under investigation. Particle radii are distributed uniformly from the selected minimum to maximum value. Table 5.2 and Table 5.3 show the specimen dimensions and particle radii have been studied to investigate the effect of discretisation. It is expected that as the particle size continues to decrease, the coefficient of variation will converge. These values should be a true measure of the effect of both packing and strength heterogeneities.

Table 5.2: Geometric and physical parameters for different L/R PFC2D.

Case I - Varying Sample Size					Case II – Varying Particle Radius				
Height (H)	Width (L)	L/R	R_{min}	No. of particles	Height (H)	Width (L)	L/R	R_{min}	No. of particles
65.57	32.79	20	1.25	207	200.00	100.00	20	3.840	205
131.15	65.57	40	1.25	831	200.00	100.00	40	1.910	829
200.00	100.00	61	1.25	1934	200.00	100.00	60	1.270	1879
262.30	131.15	80	1.25	3327	200.00	100.00	80	0.949	3355
327.87	163.93	100	1.25	5199	200.00	100.00	100	0.758	5262
393.44	196.72	120	1.25	7487	200.00	100.00	121	0.631	7600
459.02	229.51	140	1.25	10191	200.00	100.00	141	0.540	10370
590.16	295.08	180	1.25	16843	200.00	100.00	181	0.419	17211
655.74	327.87	200	1.25	20807	200.00	100.00	200	0.380	20935
786.89	393.44	240	1.25	29950	200.00	100.00	237	0.321	29339

Table 5.3: Geometric and physical parameter for different L/R PFC3D.

Case I - Varying Sample Size				Case II - Varying Particle Size		
No.	Side length	L/R	No. of particles	L/R	R_{min}	No. of particles
1	32	12	270	10	8	128
2	64	25	2161	20	4	1030
3	100	38	8244	31	2.5	4221
4	125	48	16103	39	2	8244
5	163	63	35706	51	1.5	19543
6	200	77	65958	62	1.25	33770
7	280	89	101235	77	1	65958
8	-	-	-	87	0.8	93685

Note: Particle size ratio value 1.66 for all specimens. Minimum radius is fixed to 2 mm for case I and specimen side length is fixed to 100mm for case II.

PFC2D material response

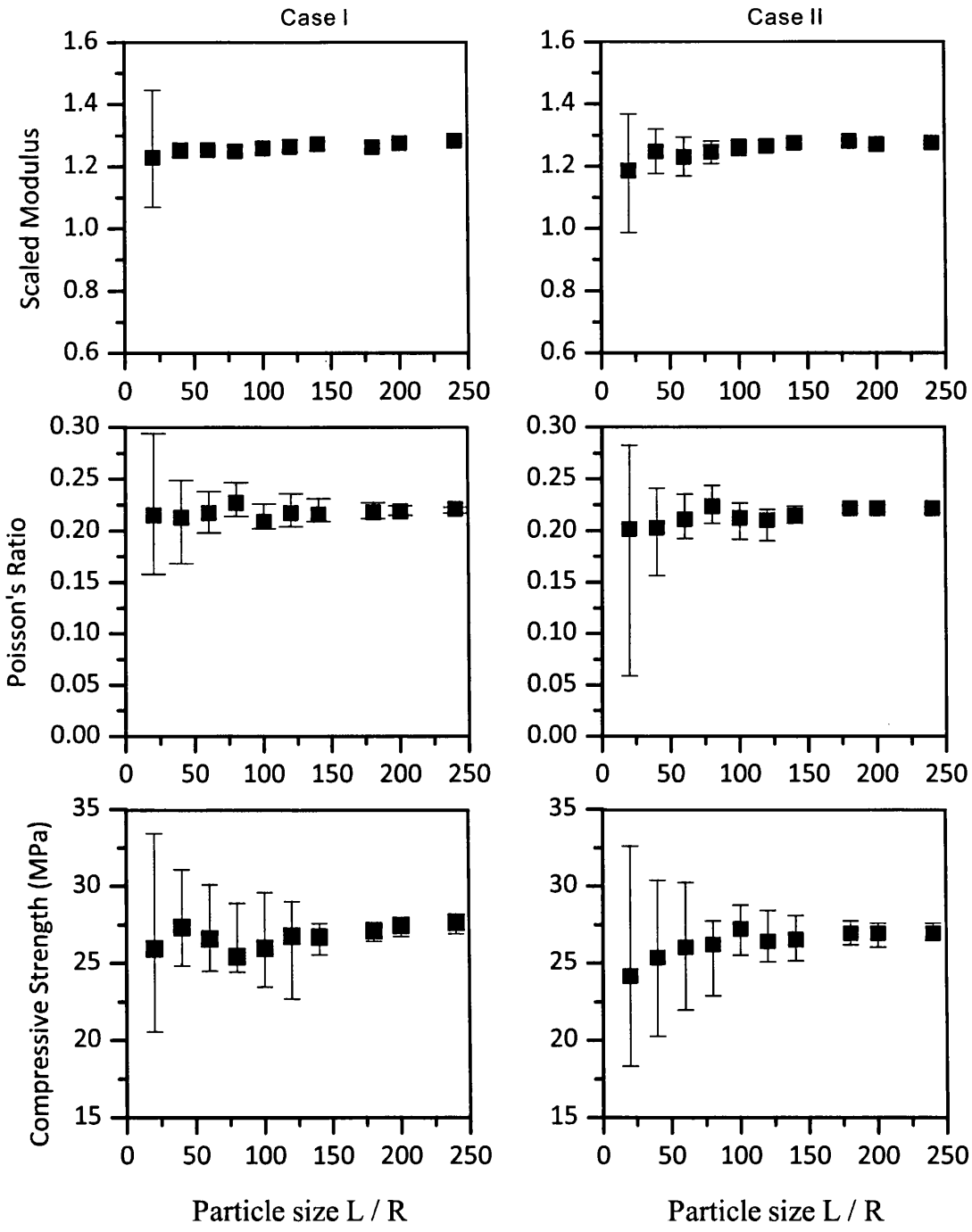

Figure 5.9: Effect of specimen size PFC2D

Results are shown in Figure 5.9 in which black square dots represent the mean value and upper and lower error bars denote the minimum and maximum value obtained from 20 samples. Similar results have been obtained from both case studies and the results indicate that the elastic constants appear to be independent of particle size. The mean

values of Young's modulus increase slightly as the degree of discretisation increases (4% and 8%). Potyondy (Potyondy and Cundall, 2004) also found the same result and concluded that this slight increase in Young's modulus may be an artifact of having too few data points to obtain a true measure of the mean values. No obvious trend can be concluded for the mean value of Poisson's ratio. The mean uniaxial compressive strength increases slightly as the particle size decreases but no clear statement can be made to describe its trend.

The variance study in Figure 5.10 indicates that smaller *L/R* ratio leads to larger respective variation. The Poisson's ratio and compressive strength are very sensitive to the degree of discretization. Therefore, in order to obtained reliable results (expectable error of 5%) in a computational efficient manner, specimen with L/R ratio larger 120 is recommended (by varying particle radius). To analysis the randomness of simulation results, Koyama and Jiang studies (Jiang *et al.*, 2010; Koyama and Jing, 2007) performed frequency distribution analysis on three macroproperties and concluded that the macro-mechanical properties were fitted to normal distribution. However, based on the results obtained from our studies, no obvious distribution trends can be concluded.

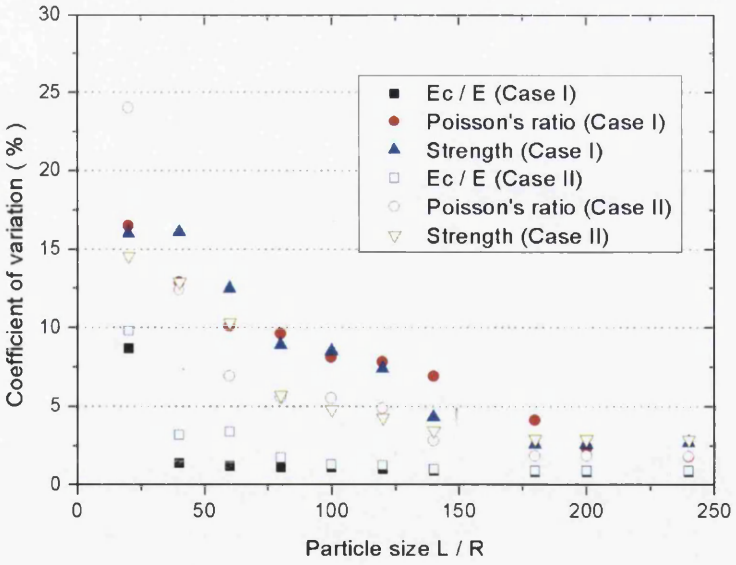

Figure 5.10: Coefficient of variation at different degree of discretization for PFC2D.

Further 2D parametric study will be performed on a rectangular specimen with fixed dimensions ($100mm \times 200mm$) and the minimum particle radius is equal to 0.631 mm which produces an L/R value equal to 120.

PFC3D material response

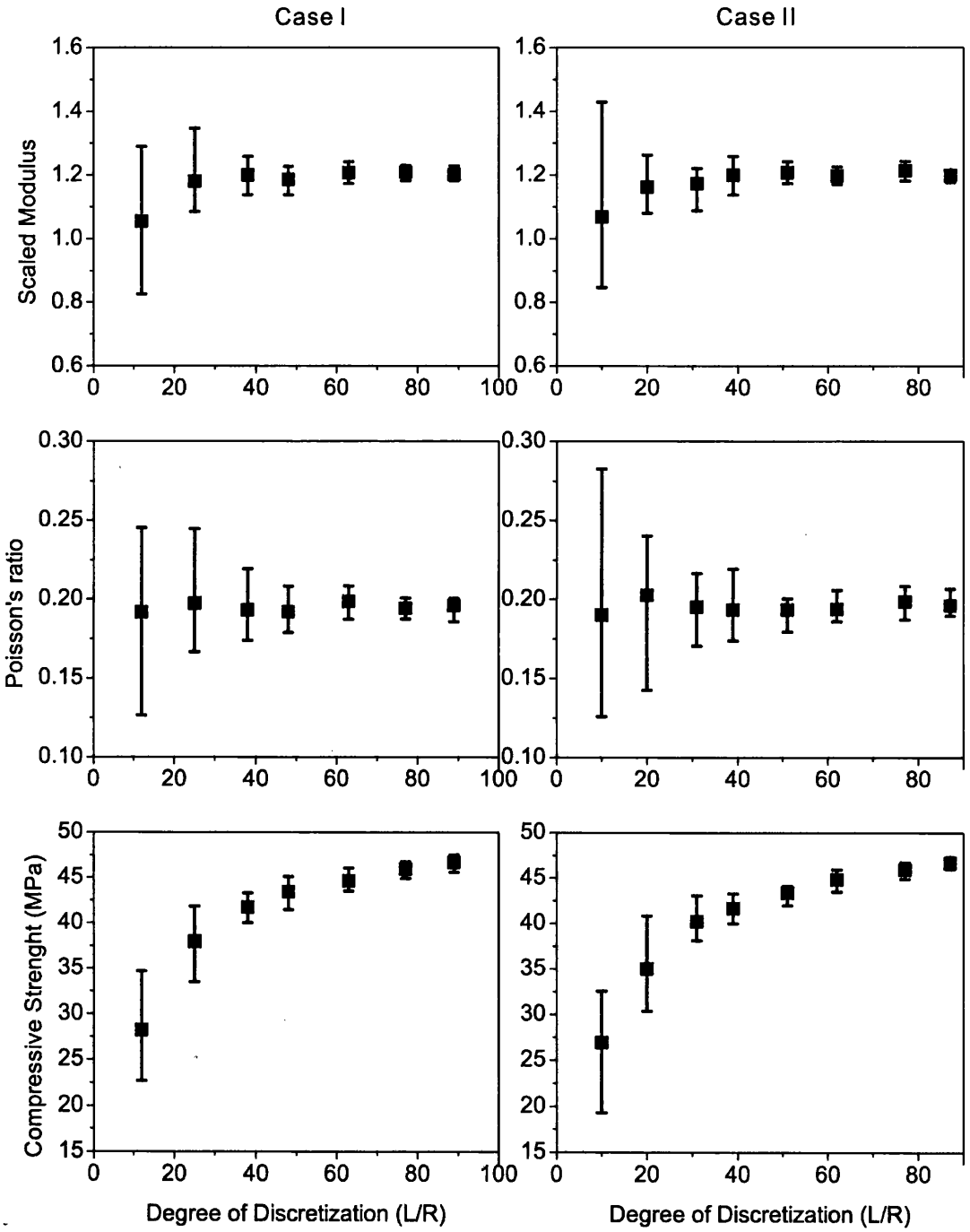

Figure 5.11: Effect of specimen size PFC3D.

Similar to the PFC2D materials response, the Poisson's ratio from the PFC3D simulation also appears to be independent of particle and sample size. Coefficient of variation of three macro-properties decreases with the increase of *L/R* and an acceptable variation appears when the L/R ratio is larger than 50. The Poisson's ratio is more sensitive to packing randomness than the other two macro-properties, Young's modulus and compressive strength obtained from 20 specimens hardly vary when *L/R* ratio is beyond 30.

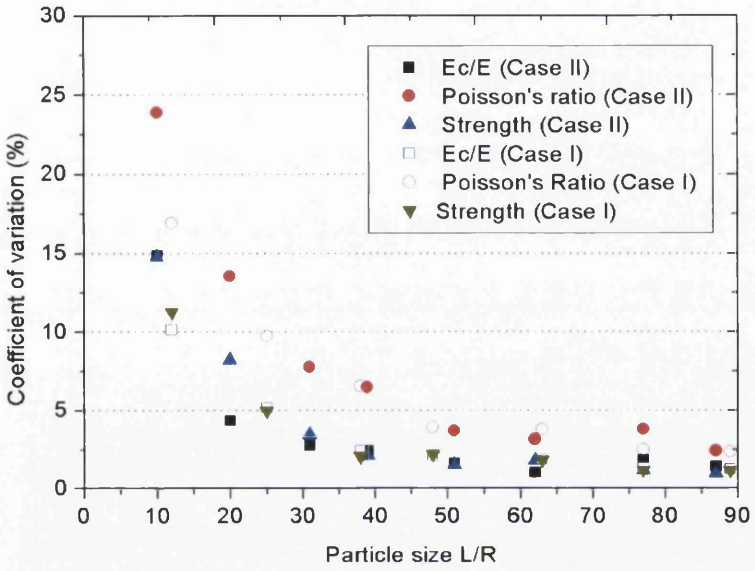

Figure 5.12: Coefficient of variation at different degree of discretization for PFC3D.

Unlike PFC2D results, the Young's modulus and uniaxial compressive strength exhibit clear size dependence. The Young's modulus increases as the *L/R* increases. 14% difference can be observed between the maximum and minimum scaled modulus and the peak value is found when *L/R* equals 77 for both cases. The most significant increase is noticed when the *L/R* increase from 10 to 20. The size dependence of Young's modulus is reflected in the modulus-stiffness scaling relation Eq.3.38 in terms of particle and bond strengths.

The unconfined compressive strength of PFC3D model increases significantly with the increase of model resolution. From the results, we can see that the compressive strength

is converging but the final convergence values could not be obtained. Up to one hundred thousand particles ($L/R=89$) have been used in the simulation, the run-time of each model becomes extremely costly, and eventually is beyond the simulation capability of particle flow code. Potyondy (Potyondy and Cundall, 2004) discovered this size dependence of compressive strength and the reason for this size effect is remained unknown. One possible explanation is provided by Wong (Wong *et al.*, 2006) which states that microstructural strength heterogeneity increases with the increase of grain size, and plays a key role in lowering the uniaxial compressive strength, which contributes to the overall decrease of strength with the increase of grain size. To verify this explanation we repeat the degree of discretization study and reduced the heterogeneity effect by setting the standard deviation of bond strength to zero.

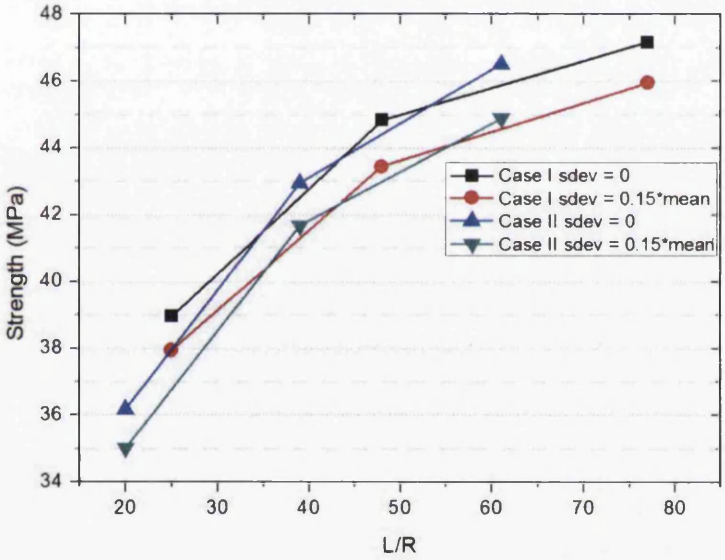

Figure 5.13: Effect of heterogeneity of bond strength on macroscopic strength.

Figure 5.13 indicates that despite the heterogeneity of the strength is reduced, the macroscopic material strength increases with the increase of L/R ratio. Both cases draw the same conclusions where the identical growth rate of compressive strength is obtained and the coefficients of variation of macro properties remains unaffected.

Taking the specimen size effect further, specimens with different geometric shapes are generated to investigate the possible variation of macro responses. Three PFC2D

specimens ($100\times100, 100\times150$ *and* 100×200) and four PFC3D specimens ($100\times100\times100$ and $100\times100\times200$ cylinder and parallelepiped) with constant L/R ratio have been investigated. However, no significant variation can be observed.

5.4.2 Particle size distribution

The randomness of particle size distribution in particle flow code is governed by minimum particle radius, particle size ratio and random seed. To determinate the influence of particle radius ratio, PFC2D and PFC3D models with the particle size ratio value range from 1.25 to 5.0 were tested. The particle assembly becomes more heterogeneous as the particle size ratio increases as shown in Figure 5.14. Porosity of each specimen remains unchanged to avoid any unnecessary disturbance.

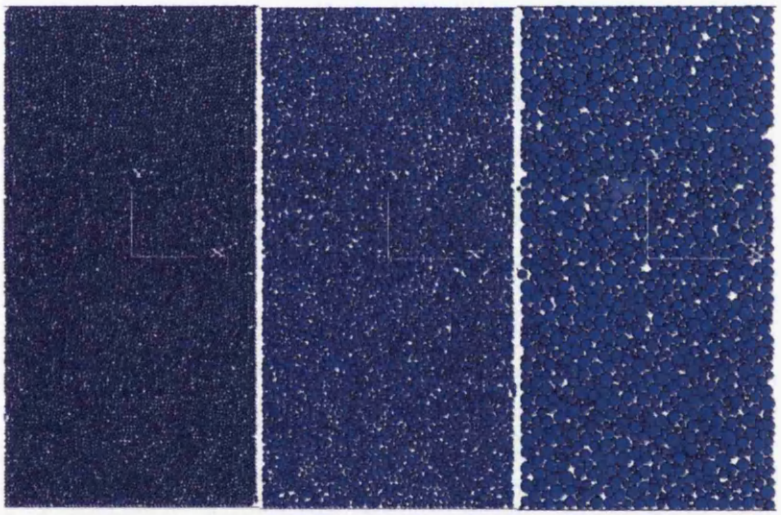

Figure 5.14: PFC2D packing pattern with different radius ratios.

Fig5.15 suggests that the scaled modulus and uniaxial compressive strength of the 2D model decrease when the particle radius ratio varies from 1 to 2, and then remain almost unchanged. The macroproperties of PFC3D material are more sensitive to the change of the particle radius ratio and up to 21% reduction is observed in compressive strength. The mean value of the Poisson's ratio of both 2D and 3D model oscillates with the increase of particle radius ratio. However, no clear statement can be made for the mean

value of Poisson's ratio. The calculated coefficients of the variation of three major macroproperties increase with the radius ratio as the specimen becomes more heterogeneous. In order to achieve an acceptable coefficient of variation of 5%, the radius ratio ranging between 1 and 2 is recommended.

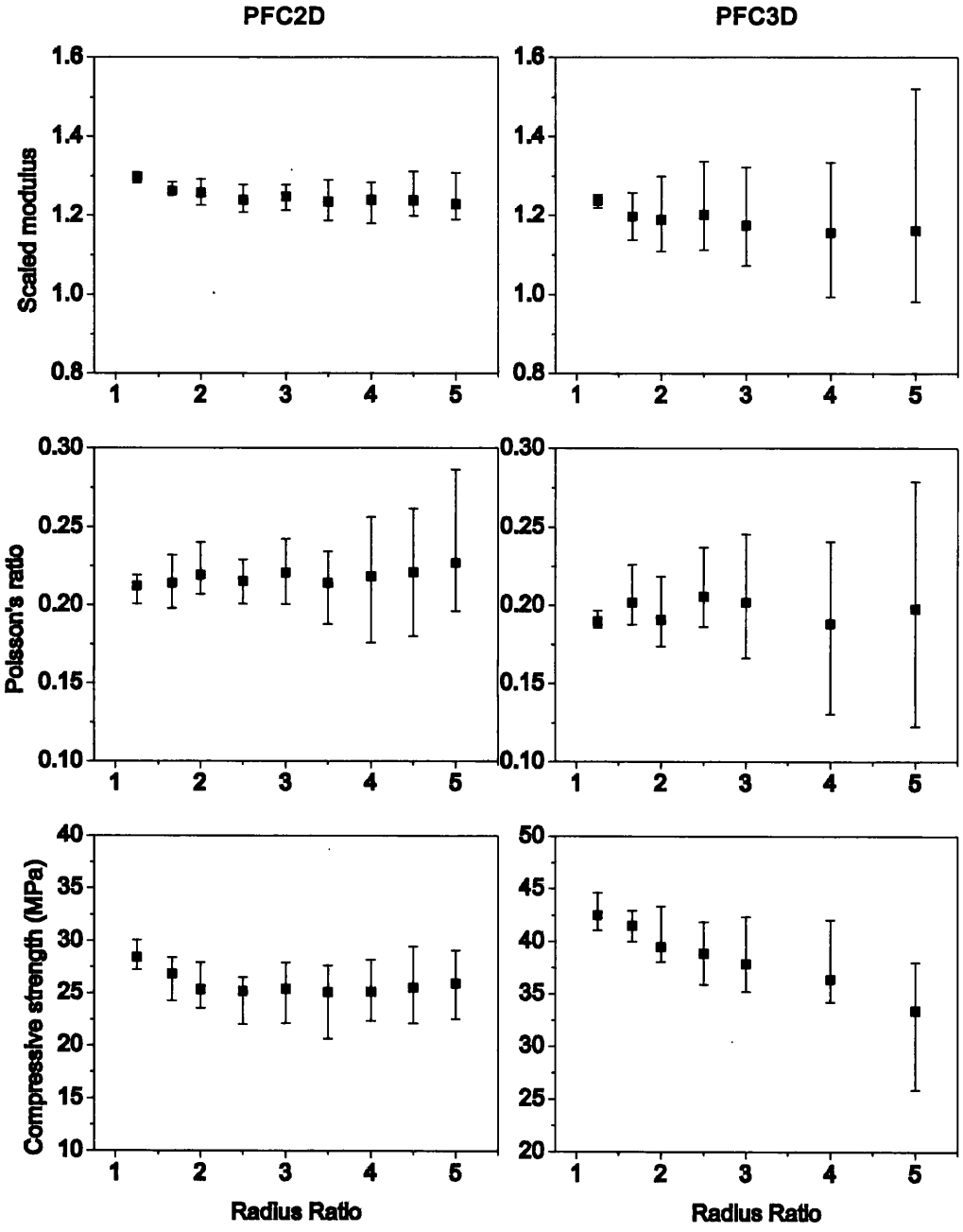

Figure 5.15: Effect of particle size ratio PFC2D and PFC3D.

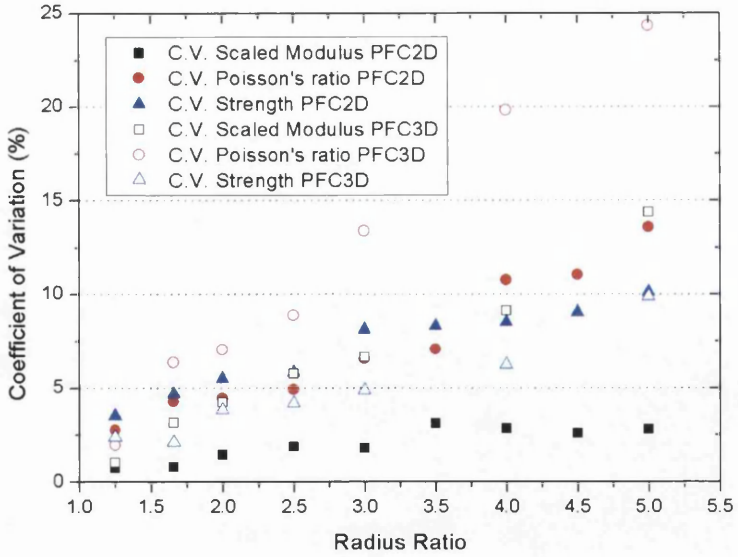

Figure 5.16: Coefficient of variation at different particle size ratio for PFC2D and PFC3D.

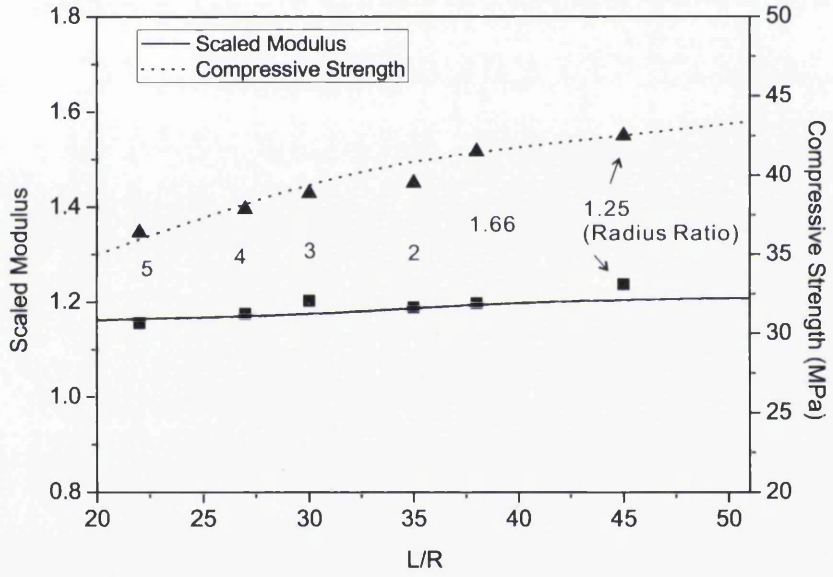

Figure 5.17: Distinguish the influence of heterogeneity by means of changing specimen radius ratio.

As a consequence of increasing radius ratio the average particle radius will increase and L/R ratio decreases. It is necessary to distinguish the effect caused by changing the radius ratio alone. In Figure 5.17 the solid and dot lines denote the variation of the scaled modulus and compressive strength with respective to *L/R* from the previous results in the previous section and the scatters correspond to different material responses obtained for different radius ratios. It can be seen that Young's modulus and

compressive strength obtained from the PFC3D specimens with different radius ratios are in good agreement with the curves. Therefore, the actual influence from increasing specimen heterogeneity by means of changing the radius ratio can be neglected. Instead, it can be viewed as another approach to modify the model resolution.

5.5 Conclusions

In this chapter, the influence of experimental and specimen geometric and physical parameters on behavior of parallel-bonded PFC model in uniaxial compression were investigated. The findings can be summarized as follows:

- Experimental parameter loading velocity has significant effect on Young's modulus, Poisson's ratio, ultimate strength stress-strain curve and damage model. Comparing to experimental results the dynamic increase factors obtained by PFC simulations are too large especially when specimen is submitted to high strain rates. The dynamic increase factors were affected by the model resolution and coarser resolutions leaded to lower dynamic increase factors. Comparison study of intensity of strain rate dependence between 2D and 3D models showed that 2D models exhibited more intense rate dependence than 3D models. Static macro properties were obtained when strain rate smaller than 0.1/s.
- The influence of model resolution (L/R) and particle size distribution (R_{max}/R_{min}) on the mean value of Young's modulus and Poisson's ratio obtained from 20 random packed specimens was indistinctive. However, the variance of macro-properties decreases significantly for large (L/R). Compressive strength of 2D models converged when L/R is large than 120. On the other hand, compressive strength obtained from 3D models increased with the increase of the model resolution and due to limitation of computing

power the convergence value has not been obtained. It has been found that the influence due to the increasing of specimen heterogeneity was weak.

References

Bischoff, P.H., Perry, S.H., 1995. Impact behavior of plain concrete loaded in uniaxial compression. Journal of engineering mechanics 121, 685-693.

Bischoff, P.H., Perry, S.H., 1991. Compressive Behavior of Concrete at High Strain Rates. Materials and structures 24, 425-450.

Comité Euro-International du Béton, 1993. CEB-FIP Model Code 1990 Redwood Books, Trowbridge, Wiltshire, UK,.

Fakhimi, A., Villegas, T., 2006. Application of Dimensional Analysis in Calibration of a Discrete Element Model for Rock Deformation and Fracture. Rock Mechanics and Rock Engineering 40, 193-211.

Fu, H.C., Erki, M.A., Seckin, M., December 1991. Review of Effects of Loading Rate on Concrete in Compression. Journal of Structural Engineering 117, 3645-3659.

Huang, H.Y., 1999. Discrete element modeling of tool-rock interaction. American: University of Minnesota.

Jiang, S.Q., Tan, Y.Q., Li, C., Yang, D.M., 2010. Studyon Mechanics Properties and Size Effect of Monocrystalle Silicon Using Discrete Element Method. 21.

Koyama, T., Jing, L., 2007. Effects of model scale and particle size on micro-mechanical properties and failure processes of rocks—A particle mechanics approach. Engineering Analysis with Boundary Elements 31, 458-472.

Lei, S., 2003. Distinct element modeling of laser asisted machining of silicon nitride ceramics. Service and Manufacturing Grantees and Research Conference Proceedings, 1270-1281.

Malvar, L.J., Ross, C.A., December 1997. Review of Static and Dynamic Properties of Concrete in Tension,. ACI Materials Journal.

Malvern, L., Jenkins, D., Tang, T., Ross, C., 1985. Dynamic compressive testing of concrete, Proc. Second Symposium on the Interaction of Non-Nuclear Munitions with Structures, Panama City Beach, Florida, pp. 194-199.

Nardin A, S.B.A., 2005. Modeling of cutting tool-soil interactin-part II: Macromechanical model and upscaling. Computer Mechanics 36, 343-359.

Potyondy, D.O., Cundall, P.A., 2004. A bonded-particle model for rock. International Journal of Rock Mechanics and Mining Sciences 41, 1329-1364.

Van Mier, J.G.M., 2004. Discussion of lattice modelling of size effect in concrete strength by Ince et al. . Engng Fract Mech 71, 1625.

Williams, M.S., March-April 1994. Modeling of Local Impact Effects on Plain and Reinforced Concrete. ACI structural journal 91, 178-187.

Wong, T.-f., Wong, R.H.C., Chau, K.T., Tang, C.A., 2006. Microcrack statistics, Weibull distribution and micromechanical modeling of compressive failure in rock. Mechanics of Materials 38, 664-681.

Yang, B., Jiao, Y., Lei, S., 2006. A study on the effects of microparameters on macroproperties for specimens created by bonded particles. Engineering computations 23, 607-631.

Yoon, J., 2007. Application of experimental design and optimization to PFC model calibration in uniaxial compression simulation. International Journal of Rock Mechanics and Mining Sciences 44, 871-889.

Chapter 6

Parametric study of parallel bonded DE model in compression –Micro constitutive parameters

The previous chapter has reviewed the parameters that might impact calibration outcomes and the most important experimental and specimen geometric and physical parameters have been investigated. This chapter will begin with the examination of different macro responses of 2D and 3D synthetic materials caused by varying the micro constitutive parameters. Then investigation on different failure modes, final crack patterns and post-peak stress-strain curves of specimen is conducted. Finally, based upon the results of obtained in this parametric study, recommendations on how to calibration PFC models to reproduce desired elasticity and ultimate strength is presented.

6.1 Effect of individual micro constitutive parameters on material deformability and strength

6.1.1 Contact modulus

Theoretical prediction by Chang (Chang, 1993) for randomly packed specimens with identical particle size found that the Young's modulus was linearly related to particle contact modulus while the Poisson's ratio was not affected. The numerical simulation result in Figure 6.1 indicates that both 2D and 3D Young's modulus of material are linearly related to the particle contact modulus and can be expressed as:

$$\begin{aligned} E &= 1.27E_c - 0.05 \quad R^2 = 1 \quad PFC2D \\ E &= 1.24E_c - 0.02 \quad R^2 = 1 \quad PFC3D \end{aligned} \tag{6.1}$$

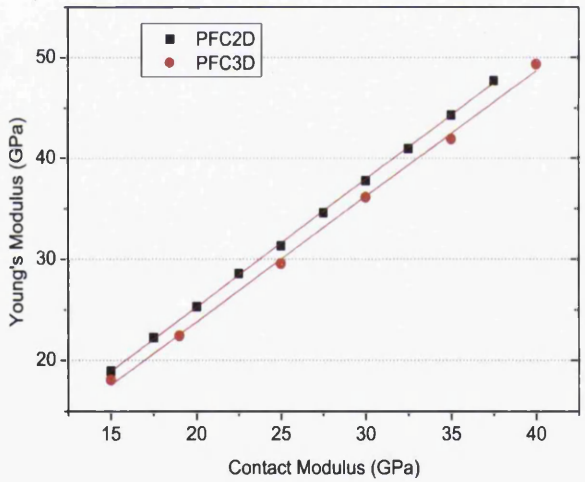

Figure 6.1 Effect of Contact Modulus on Young's Modulus for PFC2D and PFC3D

Since contact modulus is directly linearly related to normal stiffness as in Eq.3.38, the linear relationship can be obtained between the Young's modulus and normal stiffness in 2D model and exhibits size dependence in 3D model. The PFC2D Poisson's ratio have not been affected by particle contact modulus, the results have a very good agreement with theoretical prediction for random packing of identical particle sizes

made by Walton (Walton, 1986). Poisson's ratio of 3D model fluctuates noticeably with increasing contact modulus and approximately 17% difference is observed between the maximum and the minimum. The influence on compressive strength appears to be insignificant.

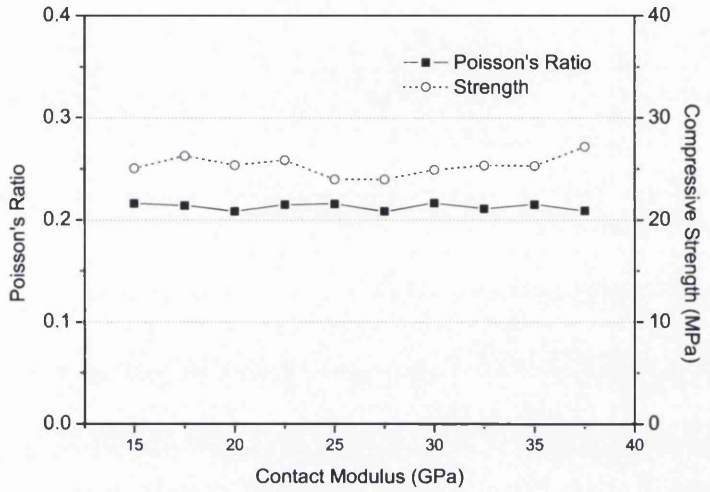

Figure 6.2: Effect of Contact Modulus on Poisson's Ratio and Compressive Strength PFC2D.

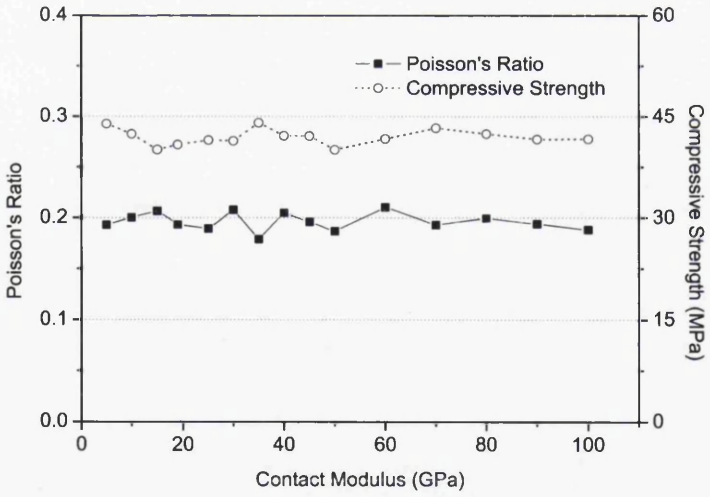

Figure 6.3: Effect of Contact Modulus on Poisson's Ratio and Compressive Strength PFC3D.

6.1.2 Contact stiffness ratio

Hence the normal stiffness is defined in terms of contact modulus (Eq.3.38) and this parametrical study is based upon the assumption that only one parameter is changing while the others keep are kept same. The contact stiffness ratio effect can be seen as the effect of shear stiffness. The shear contact stiffness decreases with the increase of the contact stiffness ratio. Results indicate that the Young's modulus and compressive strength decrease and Poisson's ratio increases as the contact stiffness ratio increases. Both scaled modulus and Poisson's ratio can be expressed as a logarithm function of contact stiffness ratio. The compressive strength is linear or second order polynomial function of the stiffness ratio for PFC2D and PFC3D respectively as shown in Eqs.6.2 and 6.3.

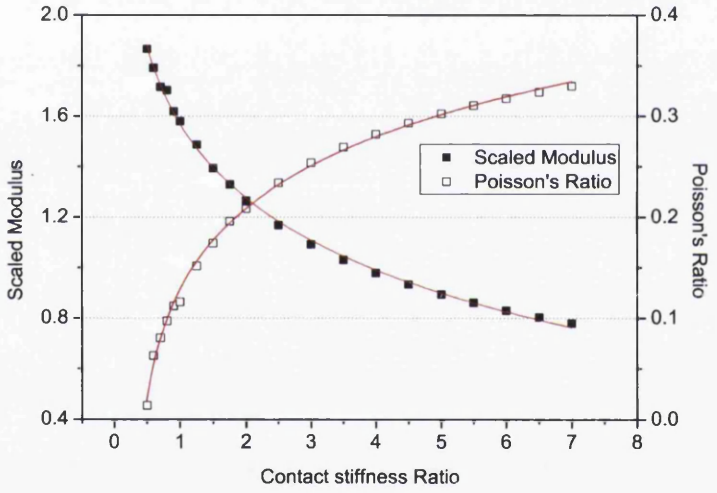

Figure 6.4: Effect of stiffness ratio on elastic constants PFC2D.

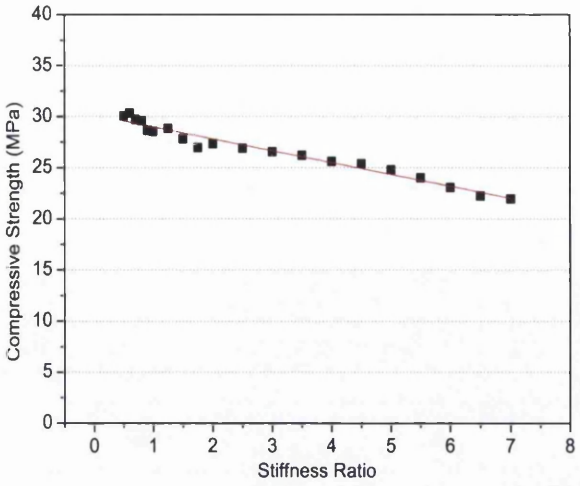

Figure 6.5: Effect of stiffness ratio on compressive strength PFC2D.

$$\frac{E}{E_c} = -0.42\ln\left(\frac{k_n}{k_s}\right) + 1.57 \qquad R^2 = 1$$

$$\nu = 0.11\ln\left(\frac{k_n}{k_s}\right) + 0.12 \qquad R^2 = 0.99 \qquad \text{PFC2D} \qquad (6.2)$$

$$q_u = -1.16\frac{k_n}{k_s} + 30.13 \qquad R^2 = 0.96$$

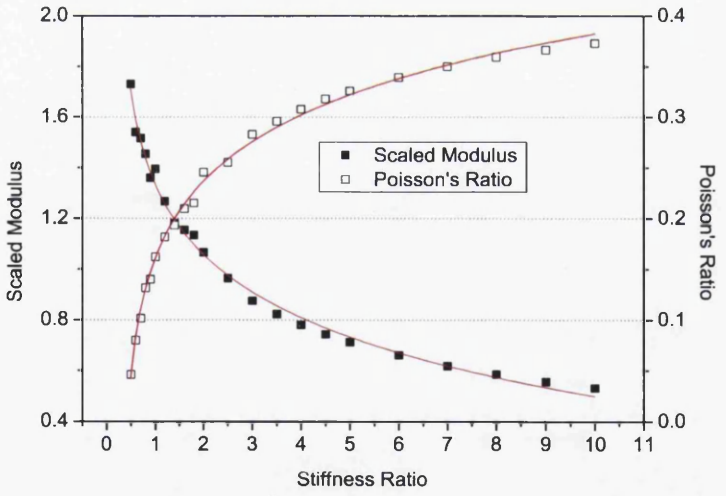

Figure 6.6: Effect of stiffness ratio on elastic constants PFC3D.

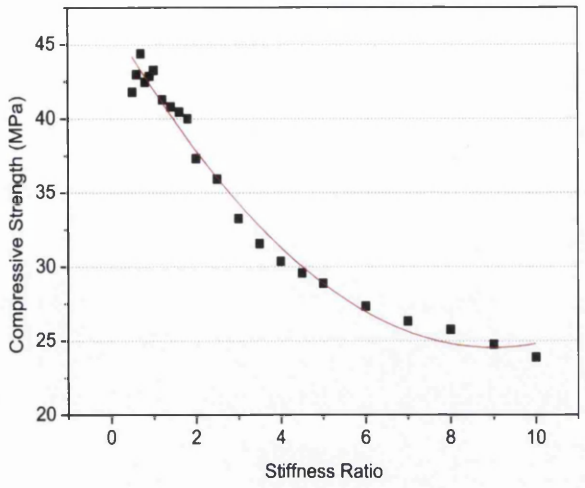

Figure 6.7: Effect of stiffness ratio on compressive strength PFC3D.

$$\frac{E}{E_c} = -0.39\ln\left(\frac{k_n}{k_s}\right) + 1.36 \qquad R^2 = 0.99$$

$$\nu = 0.11\ln\left(\frac{k_n}{k_s}\right) + 0.15 \qquad R^2 = 0.98 \qquad \text{PFC3D} \qquad (6.3)$$

$$q_u = 0.27\left(\frac{k_n}{k_s}\right)^2 - 4.9\frac{k_n}{k_s} + 46.56 \qquad R^2 = 0.98$$

6.1.3 Radius Multiplier

Model characteristic Eqs.3.40 and 3.41 suggest that the significant impact of bond radius on the stress-displacement behavior is observed at microscopic level. The beam-like element can be scaled in terms of radius multiplier (λ). Numerical simulation results indicate that the radius multiplier has a clear impact: for 2D model the material Young's modulus and compressive strength increase linearly and Poisson's ratio decreases as the radius multiplier increases. Similar results can be obtained for 3D models where the increasing trend of Young's modulus and compressive strength can be expressed as a second order polynomial. After regression analysis the following empirical relationships have been established:

$$\frac{E}{E_c} = 1.87\bar{\lambda} + 0.3 \qquad R^2 = 0.99$$

$$\nu = 0.20\bar{\lambda}^{-0.174} \qquad R^2 = 0.93 \qquad \text{PFC2D} \qquad (6.4)$$

$$q_u = 37.31\bar{\lambda} + 5.95 \qquad R^2 = 0.99$$

$$\frac{E}{E_c} = 0.64\bar{\lambda}^2 + 0.22\bar{\lambda} + 0.23 \qquad R^2 = 1$$

$$\nu = 0.19\bar{\lambda}^{-0.71} \qquad R^2 = 0.97 \qquad \text{PFC3D} \qquad (6.5)$$

$$q_u = 40\bar{\lambda}^2 - 0.13\bar{\lambda} + 2.88 \qquad R^2 = 1$$

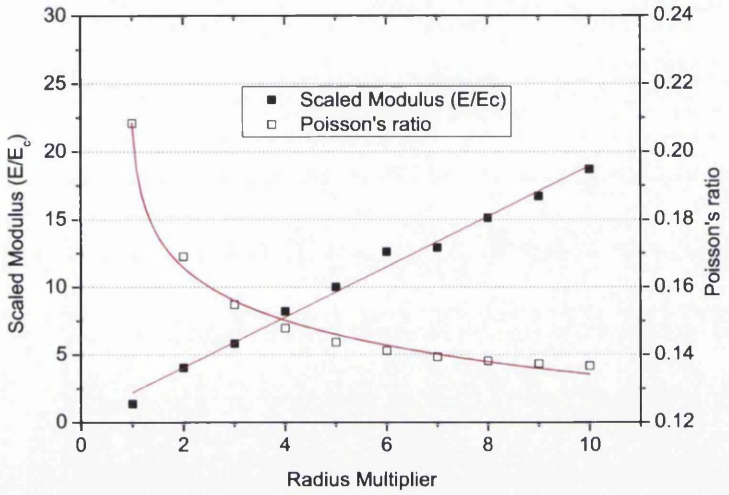

Figure 6.8: Effect of radius multiplier on elastic constants PFC2D.

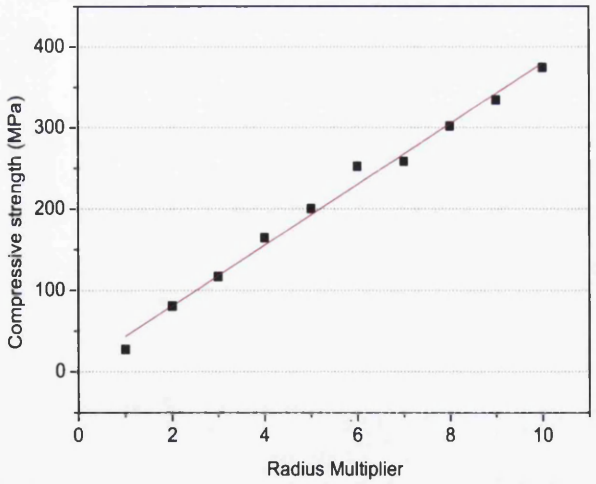

Figure 6.9: Effect of radius multiplier on compressive strength PFC2D.

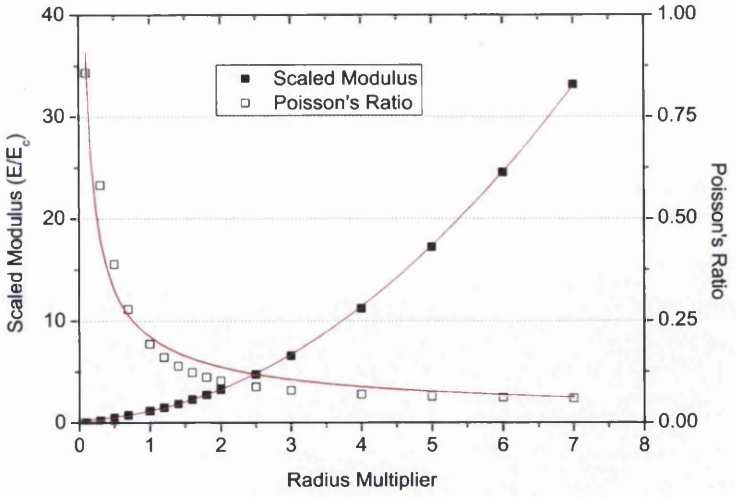

Figure 6.10: Effect of radius multiplier on elastic constants PFC3D.

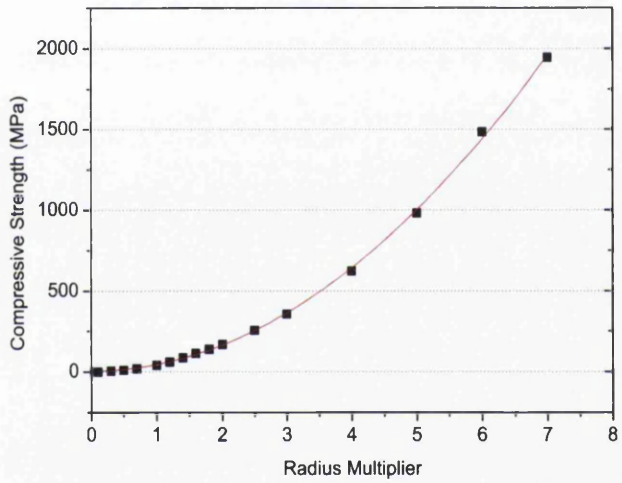

Figure 6.11: Effect of radius multiplier on compressive strength PFC3D.

6.1.4 Bond strength ratio

Potyondy and Cundall (Potyondy and Cundall, 2004) suggest setting the same value for both bond normal and shear strength ($\bar{\sigma}_b = \bar{\tau}_b$) in order to include both micro-tensile and micro-shear failure mechanisms. They show that including both micro-failure mechanisms leads to more sophisticated damage evolution adjacent to a circular hole than the case excluding micro-shear failure. Huang (Huang, 1999)

investigates the influence of bond normal and shear strength of contact bond by simulation of uniaxial compression tests of granular assemblies with different ratios of bond shear strength to normal strength. They conclude that a low ratio of shear strength to normal strength (less than 2) results in unrealistic response. Yang (Yang et al., 2006) also suggest the same threshold for the bond strength ratio, noting that when the ratio larger than 2, the compressive strength is mainly determined by bond normal strength, otherwise bond shear strength is dominant. Cho (Cho et al., 2007) conducted uniaxial compression test and Brazilian test simulations and found that the ratio of tensile to uniaxial compression strength of the predicated macroscopic behaviour is not influenced by the bond strength ratio.

According to previous dimensional analysis, the material uniaxial compressive strength can be scaled by either bonded mean value of normal or shear strength. In this section we keep the bond normal strength at a constant level and varies the bond strength ratio by changing bond shear strength. Figure 6.12 shows the material elasticity is not affected by the variation of bond strength ratio.

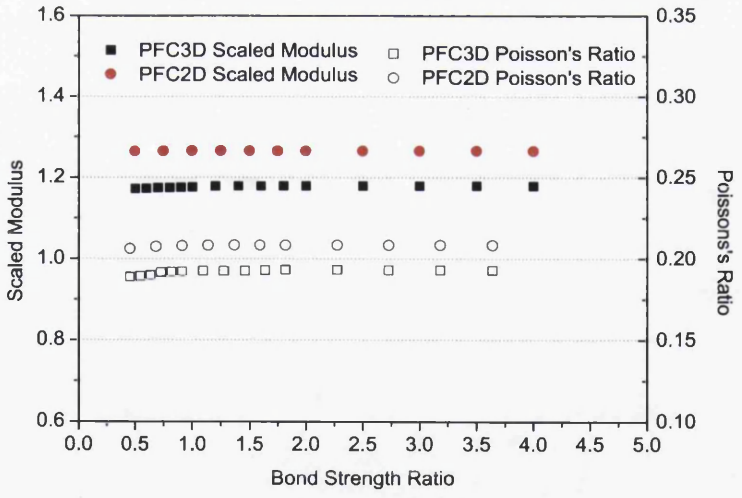

Figure 6.12: Effect of bond strength ratio on elastic constant.

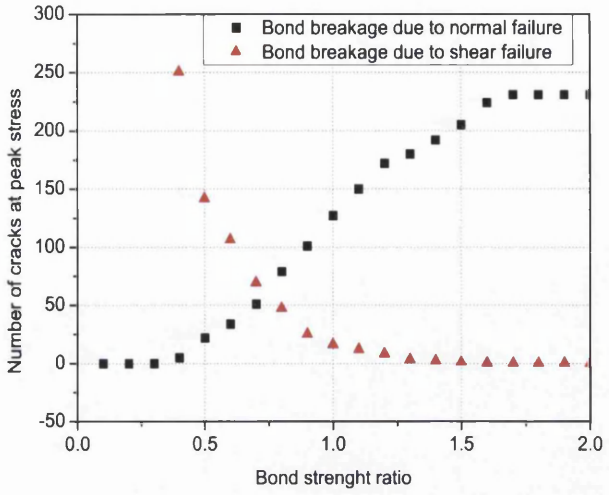

Figure 6.13: Number of cracks at peak stress PFC2D.

Similar compressive strength response can be found in PFC2D and PFC3D specimens. Both of results can be divided into three parts by two characteristic bond strength ratio values 0.5 and 1.5 (2.0 for PFC3D). As the bond shear strength to normal strength ratio increases, the material compressive strength increases linearly up to the lower bound. The compressive strength keeps rising up to the upper bound but not as fast as before. Then compressive strength reaches a constant value when bond strength ratio is equal to the upper bound. At this point a higher uniaxial compressive strength can be obtained by specifying a higher bond normal strength.

Figure 6.13 indicates the number of cracks at peak stress for micro-shear and micro-tensile failure. The material failure is dominated mainly by micro-shear bond breakage when the bond strength ratio is smaller than the lower-bound value,. To reproduce both micro-tensile and micro-shear failure mechanisms the bond strength ratio should be defined between the lower and upper bounds. The parallel bond tensile failure dominates the macro-failure mechanism and the number of cracks remains at a constant level when the bond strength ratio is larger than the upper bound value.

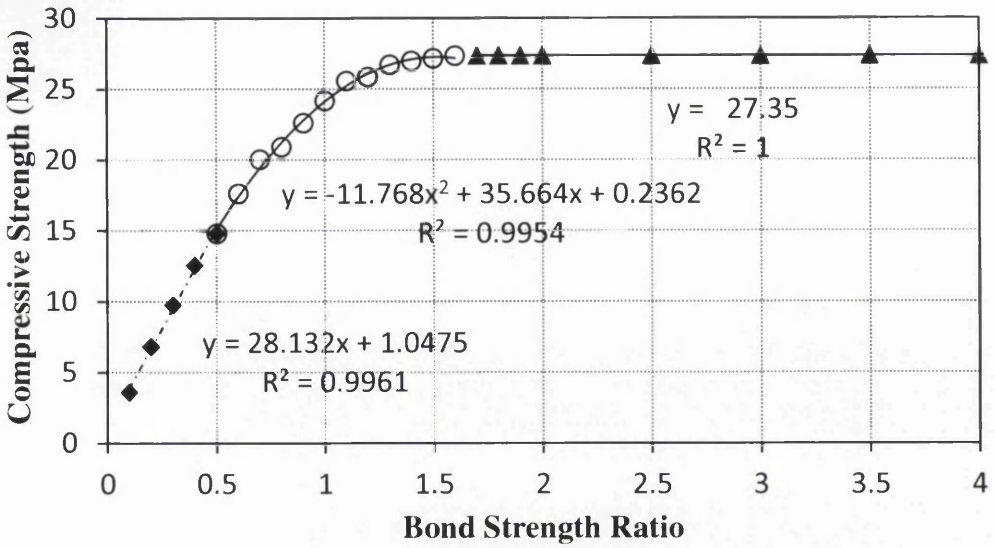

Figure 6.14: Effect of bond strength ratio on compressive strength PFC2D.

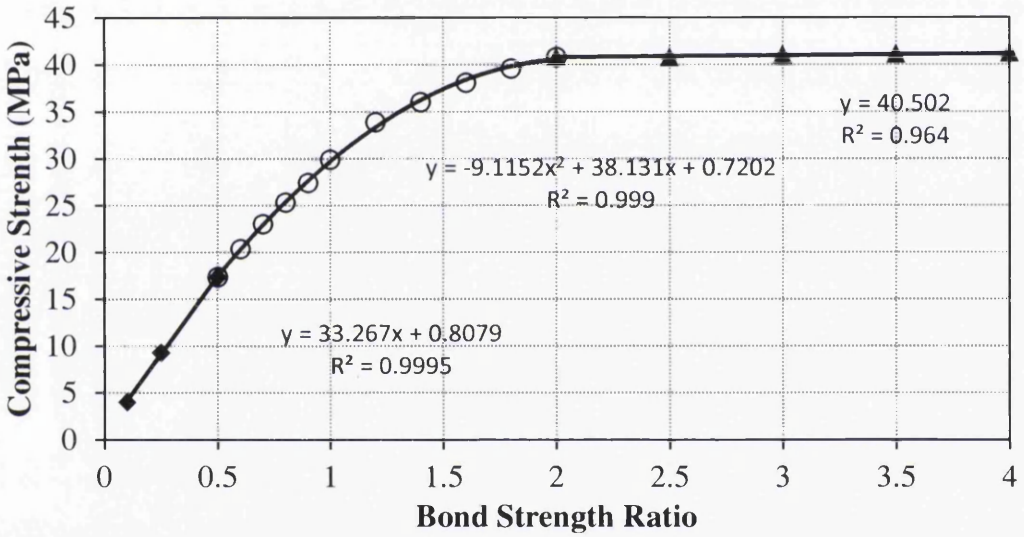

Figure 6.15: Effect of bond strength ratio on compressive strength PFC3D.

The effect of the parallel bond strength ratio on the uniaxial compressive strength obtained can be expressed as following:

$$\begin{cases} \sigma_c = 28.13\dfrac{\tau_{b,m}}{\sigma_{b,m}} + 1.05 & 0 \le \dfrac{\tau_{b,m}}{\sigma_{b,m}} \le 0.5 \quad R^2 = 1 \\ \sigma_c = -11.76\left(\dfrac{\tau_{b,m}}{\sigma_{b,m}}\right)^2 + 35.66\left(\dfrac{\tau_{b,m}}{\sigma_{b,m}}\right) + 0.24 & 0.5 < \dfrac{\tau_{b,m}}{\sigma_{b,m}} \le 1.5 \quad R^2 = 1 \quad PFC2D \\ \sigma_c = \text{Constant} & 1.5 < \dfrac{\tau_{b,m}}{\sigma_{b,m}} \quad R^2 = 1 \end{cases} \tag{6.6}$$

$$\begin{cases} \sigma_c = 33.27\dfrac{\tau_{b,m}}{\sigma_{b,m}} + 0.81 & 0 \le \dfrac{\tau_{b,m}}{\sigma_{b,m}} \le 0.5 \quad R^2 = 1 \\ \sigma_c = -9.12\left(\dfrac{\tau_{b,m}}{\sigma_{b,m}}\right)^2 + 38.13\left(\dfrac{\tau_{b,m}}{\sigma_{b,m}}\right) + 0.72 & 0.5 < \dfrac{\tau_{b,m}}{\sigma_{b,m}} \le 2.0 \quad R^2 = 1 \quad PFC3D \\ \sigma_c = \text{Constant} & 2.0 < \dfrac{\tau_{b,m}}{\sigma_{b,m}} \quad R^2 = 1 \end{cases} \tag{6.7}$$

Once the bond strength ratio between the bond shear strength and the bond normal strength is selected, desired material macroproperty uniaxial compressive strength can be reproduced by multiplying the mean normal and shear strength and their standard deviation by a scale factor. Figure 6.16 shows that a linear relationship between compressive strength and scale factor is obtained for different bond strength ratios.

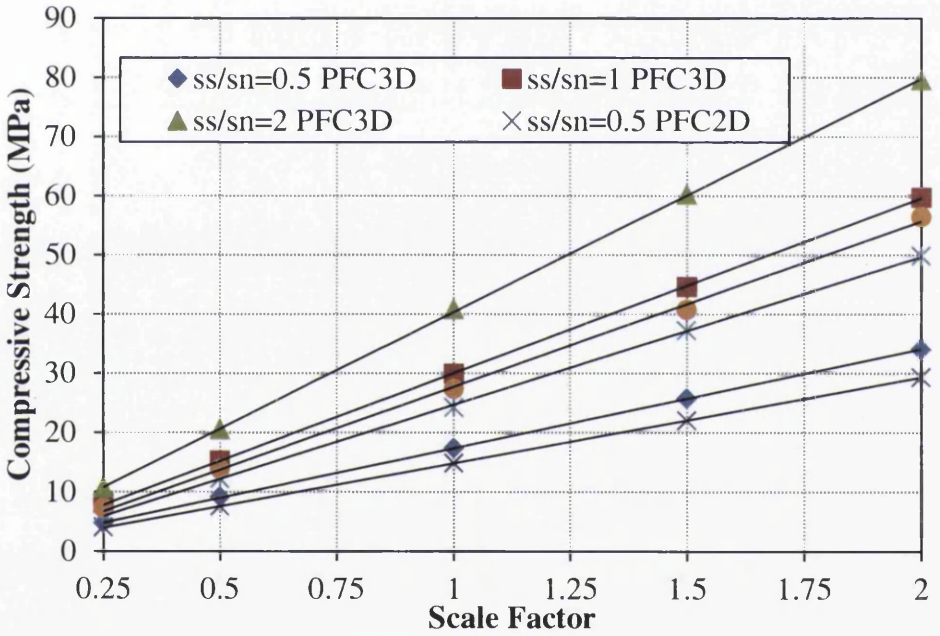

Figure 6.16: Scale factor for different bonding strength ratio.

6.1.5 Friction coefficient

Huang (Huang, 1999) and Yang (Yang et al., 2006) performed a study on effect of friction coefficient for contact bond and parallel bond model respectively and reported that peak compressive strength in uniaxial compression of particle assemblies is only slightly affected by the inter-particle friction coefficient. Wang and Mora (Wang and

Mora, 2008) also derived the same conclusion from uniaxial compression simulations with a pre-existing crack. Huang (Huang, 1999) concluded that the macroscopic residual strength is only slightly related to the inter-particle friction coefficient. They suggest instead that the residual strength can be linked to force anisotropies and the slip surface evolution. Cho (Cho et al., 2007) also investigated the effect of inter-particle friction coefficient and arrived at the conclusion that the friction coefficient only slightly affects dilation and has no effect on the macroscopic tensile strength to compressive strength ratio.

However previous studies mainly focus on the strength of two-dimensional synthetic material. Figure 6.17 indicates that the deformability is clear affected by grain friction coefficient. Young's modulus increases with increasing friction coefficient while Poisson's ratio decreases with increasing friction coefficient. Friction coefficient has more significant impact on PFC3D model than PFC2D model. Up to 22% and 29% increase or decrease rate can be found for scaled modulus and the Poisson's ratio respectively material where 18% and 23% are for two dimensional model. After aggression analysis both tendencies can be approximated by a second order polynomial function as expressed in Eqs.6.8 and 6.9. PFC3D material compressive strength increases 24% while on the other hand the PFC2D compressive strength fluctuate as little as 8% and no clear trend can be observed. It is reasonable to argue that the impact of particle friction coefficient on the compressive strength for PFC2D model is weak and can be ignored.

$$\begin{aligned} &\frac{E}{E_c} = -0.2\mu^2 + 0.44\mu + 1.1 && R^2=1 \\ &v = 0.07\mu^2 - 0.13\mu + 0.26 && R^2=1 \end{aligned} \qquad \text{PFC2D} \qquad (6.8)$$

$$\begin{aligned} &\frac{E}{E_c} = -0.17\mu^2 + 0.45\mu + 1 && R^2=1 \\ &v = 0.06\mu^2 - 0.15\mu + 0.25 && R^2=1 \\ &q_u = -8.86\mu^2 + 19.11\mu + 33.5 && R^2 = 1 \end{aligned} \qquad \text{PFC3D} \qquad (6.9)$$

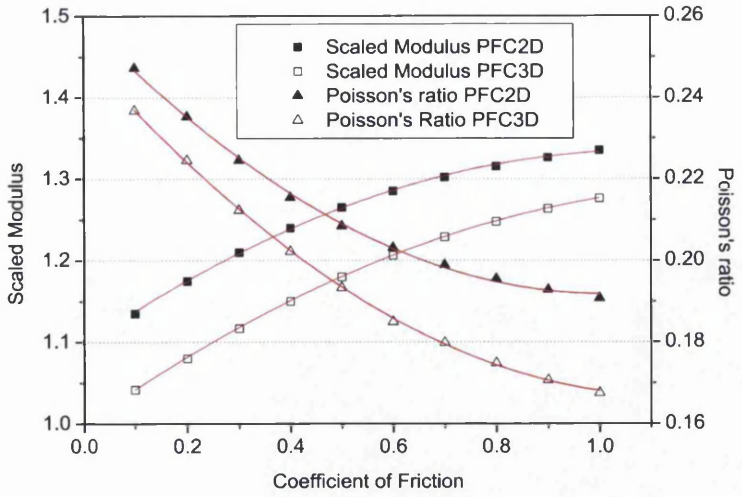

Figure 6.17: Effect of coefficient on material elasticity.

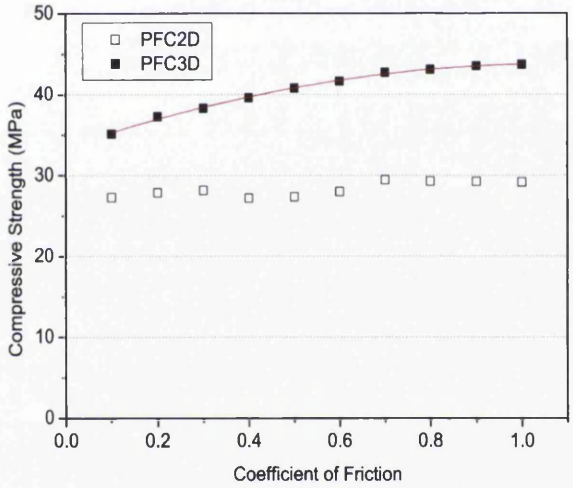

Figure 6.18: Effect of coefficient on Compressive Strength.

6.1.6 Crack-initiation stress

To better describe the heterogeneity characteristic of brittle material such as concrete, the bond strength at each contact was assigned random strength values drawn from a probability distribution. For one of the most popular normal distribution specification of two parameters, namely the mean value and standard deviation, are required. The crack-initiation stress is defined as the axial stress at which non-elastic dilation begins, and is identified as the point of deviation from linear elasticity on a plot of axial stress

versus volumetric strain (Potyondy and Cundall, 2004). During the uniaxial compressive test the crack-initiation stress is recorded as the axial stress at 1% of the total number of cracks at peak strength. Numerical results indicate that the crack-initiation stress is affected only by the ratio between the standard deviation of bond strength and mean value bond strength. As the standard deviation of bond strength increases, both crack-initiation stress and compressive strength decrease as shown in Figure 6.19 while the crack-initiation stress drops more significantly than the compressive strength. The most noticeable reduction of fraction of crack-initiation stress can be observed when the coefficient of variation of bond strength is between 20% and 50%.

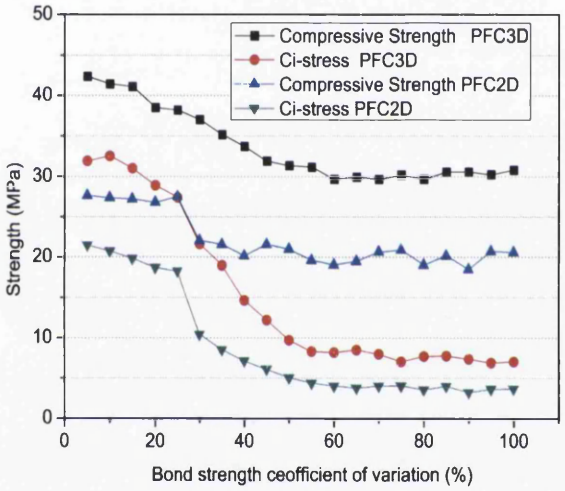

Figure 6.19: Compressive and crack initial strength verse coefficient of variation of bond strength.

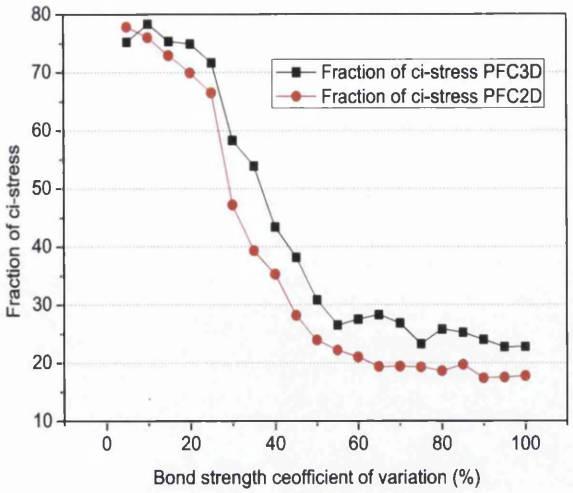

Figure 6.20: Fraction of ci-stress verse coefficient of variation of bond strength.

6.2 Failure mode and post-peak stress-strain curve

6.2.1 Crack pattern

As discontinuities are an inherent part of the DEM method, without any additional descriptions are required for the evolution of cracks. The breakage of bonds between particles automatically initiates crack pattern. In laboratory experiments, two specimen's results are never identical even the same conditions are applied. The failure crack patterns are phenomenological similar but the exact positions of the cracks and spalling vary. Thus the exact damage pattern cannot be replicated in experiment and numerical simulations, even the state of the art algorithms can only determine the major crack path. However, valuable information such as failure type, crack initiation, and propagation direction can be obtained from modelling.

It has been well understood that the elastic mismatch between loading platen and the specimen leads the different lateral deformation in platen and specimen. In the case of loading platen stiffer than specimen, the friction force caused by interaction between platen and specimen will develop a confining compressive stress at the end of

specimen then cause triaxial compressive stress fields in the specimen near the loading platens (Fig.6.21a). As a consequence, the famous hourglass failure mode appears (Fig.6.21b).

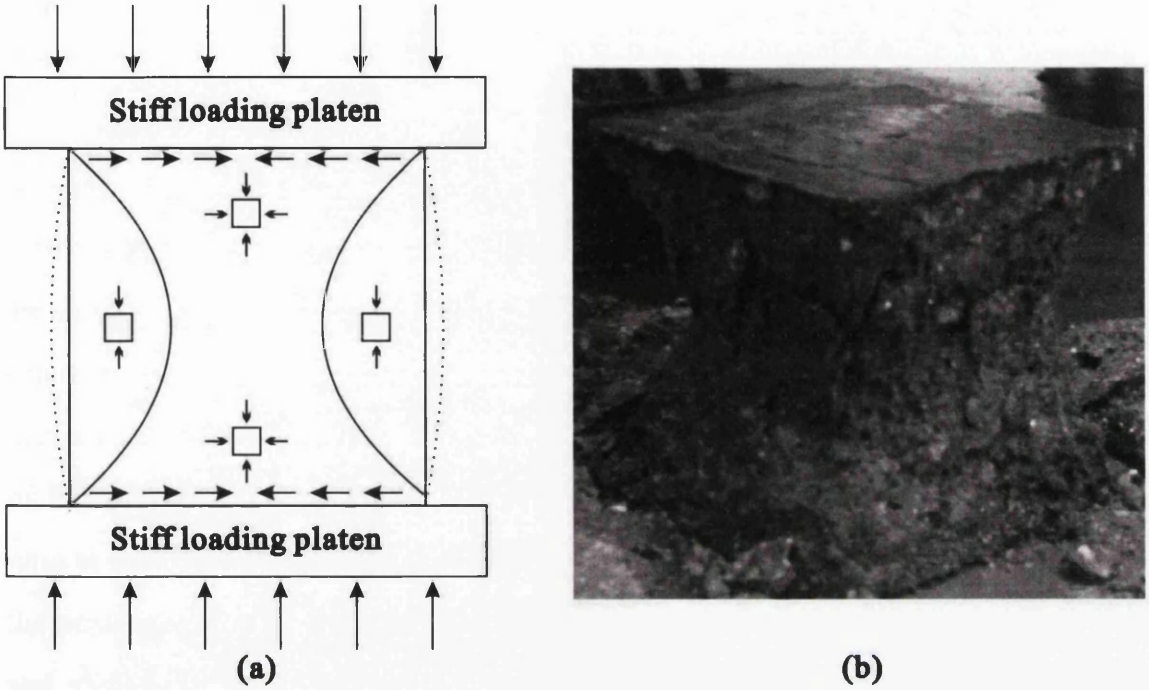

Figure 6.21: Cubic concrete specimen failure mode (a) Triaxial compressive stress fields cause by shear stress between loading platen and specimen; (b) experimental observation of hourglass failure mode (Tang *et al.*, 2010).

In this study, we intended to analyze the variations in the crack pattern due to the micro-parameters of the parallel boned discrete element model. Note that the numerical analysis is carried out by assuming that the bond strengths are identical to minimize disturbance raised from strength heterogeneity, and the random seed keeps constant to construct an identical particle packing configuration. Images of bond breakages are represented by black and red line segments which distinguishes micro-tensile failure mode from micro-shear failure mode.

The results indicate that final crack pattern in the synthetic material is affected by the local stiffness ratio (k_n / k_s) and bond strength ratio ($\tau_{b,m} / \sigma_{b,m}$). This is illustrated by the damage pattern for the synthetic specimens with different local stiffness ratios and

bond strength ratio values in Figure 6.22. When the external loading reaches the crack initial stress, the cracks, representing by bond rupture, began to uniformly form inside the specimens. Further loading leads to cracks concentrating along the major shear band which results in specimen failure. As the stiffness ratio increases more diffuse crack pattern is observed. For those models consisting of both micro-tensile and micro-shear failure models, increasing the stiffness ratio leads to a larger percentage of bond rupture in the micro-tensile failure model. It is due to the fact that by increasing the normal stiffness, greater local normal stresses and hence tensile cracks are developed in the specimen. As suggested by Potyondy and Cundall (Potyondy and Cundall, 2004), by keeping the strength ratio smaller than 1, both micro-tensile and micro-shear failure mechanisms are replicated. According to results from Figure 6.22 much more realistic rupture path can be reproduced in the models by setting strength ratio to 0.5 and stiffness ratio larger than 2. A major inclined shear band is formed at the post-peak loading regime, the top and bottom block sheared against each other, and sliding results in shear bond breakages and frictional slips between particles adjacent to the shear band (Yoon, 2007).

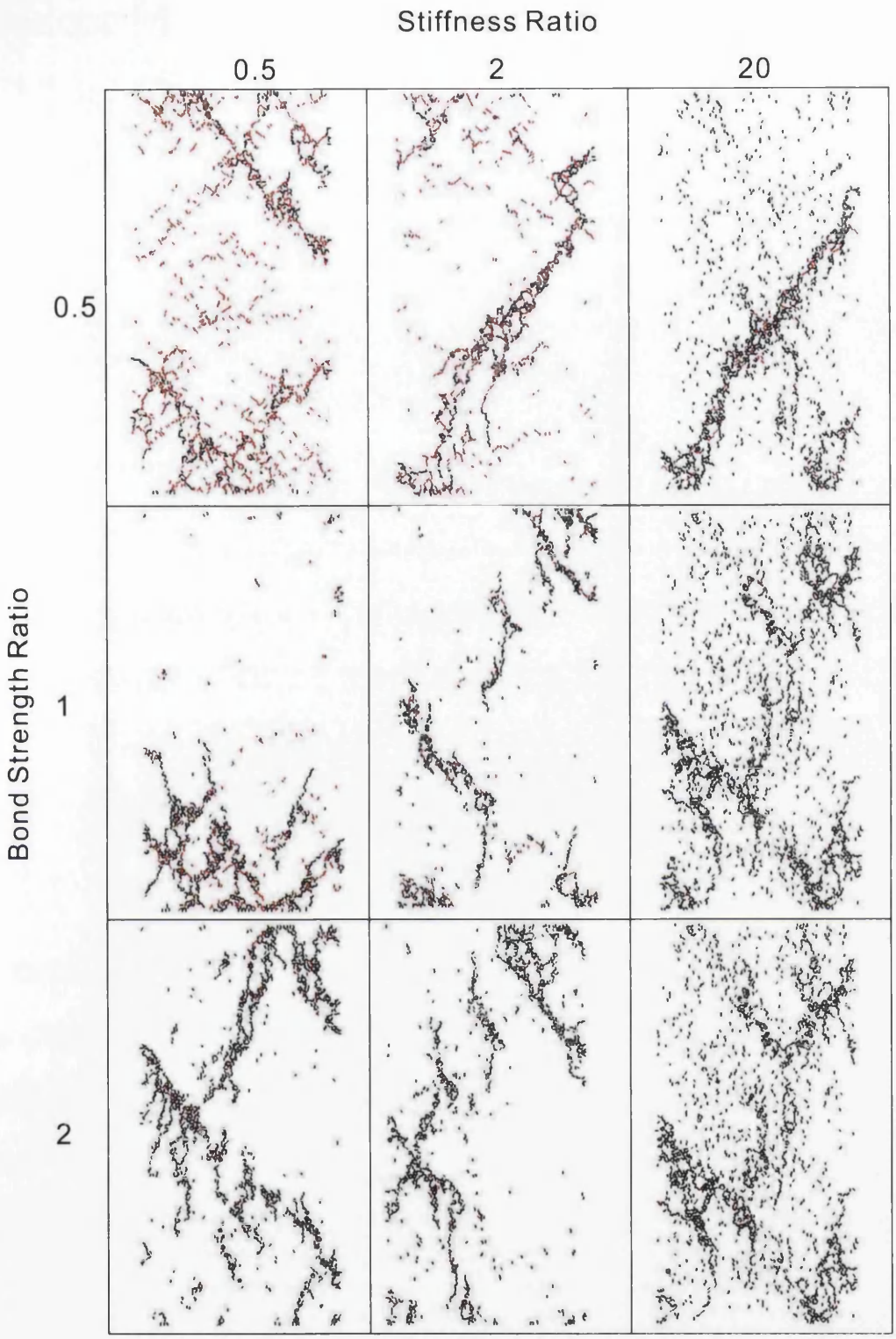

Figure 6.22: Crack pattern in the damaged specimens.

The lateral constraint can be simulated by defining friction to the loading platen. As the loading platen wall is rigid in particle flow code, introduction of frictional restraint

leads to shear forces developed between boundary particles and the loading platen. These shear forces can be seen as confining compressive stress at the specimen ends. As a consequence, the compressive strength will increase. Moreover, change in frictional end confinement will affect the contact force chain in the end zone. Fig.6.23 indicates that one additional main crack arising from the bottom corner at peak stress caused by the end constraint which leads to spalling of specimen, although the exact damage pattern observed from experiment could not be replicated. However, it has been found that by introducing interface friction increases the probability of reproduce shear band.

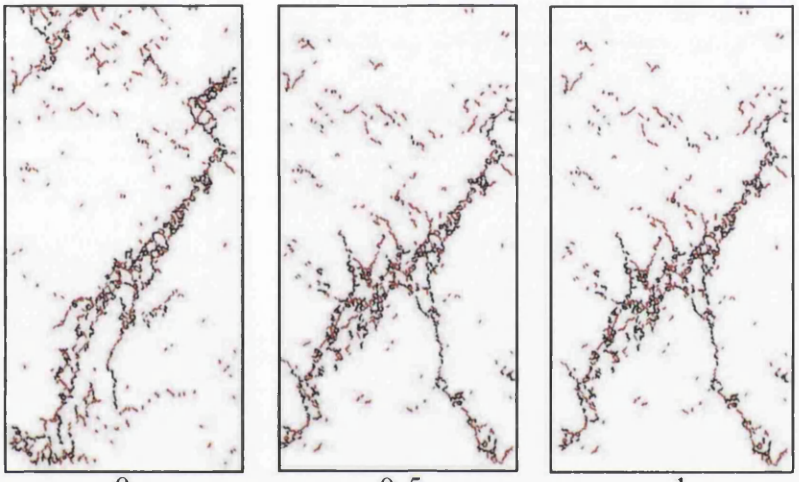

Figure 6.23: Crack pattern for different friction coefficients of load plates.

The crack pattern observed in laboratory experiments is sensitive to the shape of the specimen (del Viso et al., 2008) where cylinders broke by a diagonal fracture plane and cubes present a busting rupture combined with a dense columnar cracking have been reported. The slenderness, defined as the ratio of height to diameter of specimen, has been considered as the major component of specimen geometry effect. Increasing the specimen high causes perturbation of the nominally homogeneous stress field discussed above. A rectangular and cubic simulation model can be considered as approximation of cylinders and cubic specimen in laboratory experiment respectively. As shown in Figure 6.24 the damage pattern reproduced by the calibrated PFC2D is in good agreement with laboratory observation.

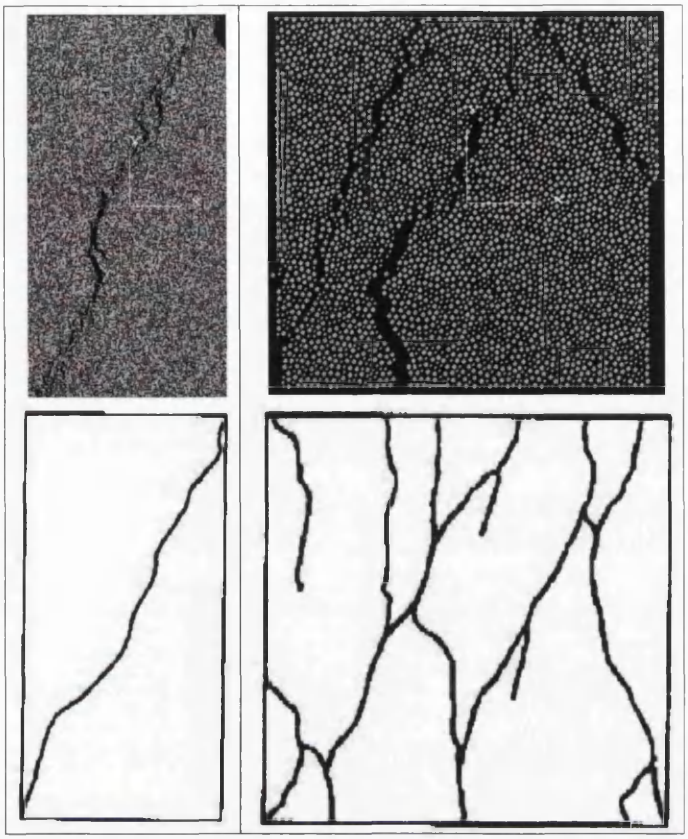

Figure 6.24: Comparison of numerical final damage modes under uniaxial compressive loading and experiment data (Vonk, 1993) without frictional restraint.

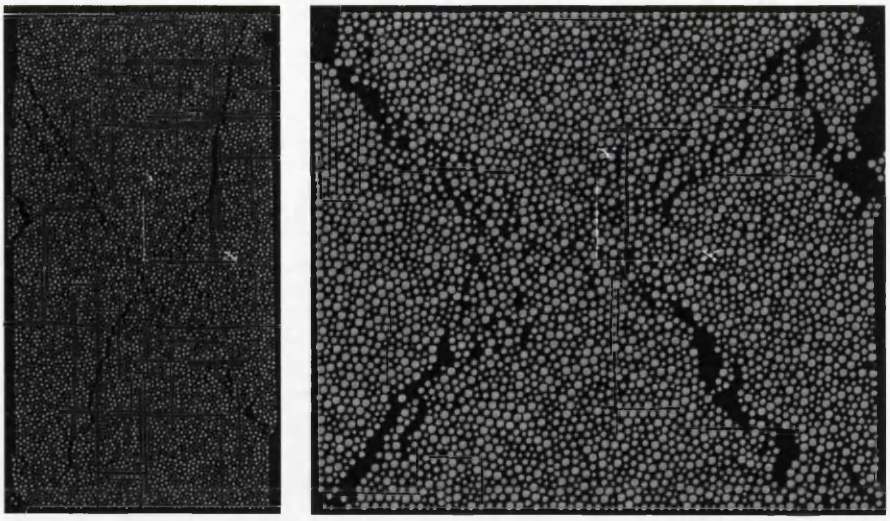

Slenderness ratio = 2 Slenderness ratio =1

Figure 6.25: Replication of hour-glass failure mode with lateral restraint.

6.2.2 Post-peak response

Although the linear elastic bond constitutive model is adopted the overall stress-strain curve of synthetic material appears to be nonlinear and post-peak strain softening can be simulated. As mentioned in section.5.3 not only the apparent ultimate strength is sensitive to strain rate, but also the post-peak stress-strain curve exhibits strain rate dependence. The descending portion of the stress-strain curve becomes steeper by lowering the strain rate, or in other words, the material fails in a more brittle fashion.

From the normalized complete stress-strain curve in Figure 6.26, we can see that a minor improvement of ductility and residual strength of synthetic material can be achieved by increasing inter-particle friction.

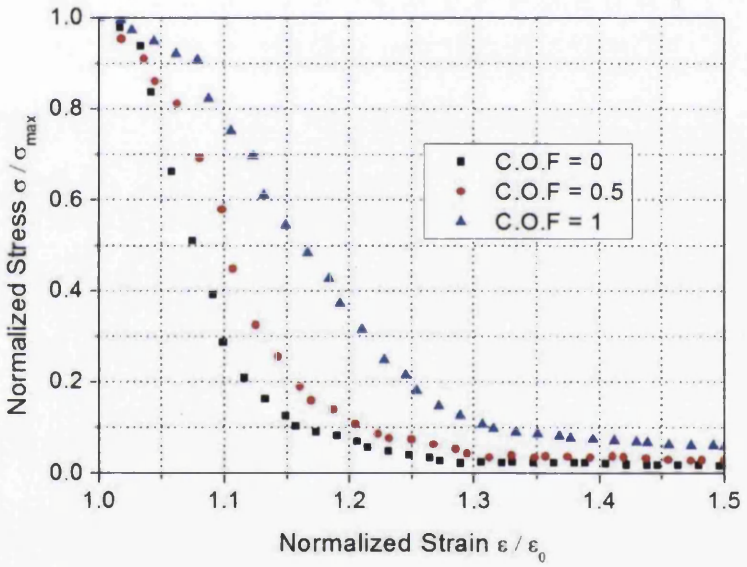

Figure 6.26: Effect of inter-particle friction on post-peak stress-strain curve.

6.3 Recommendations on calibration elastic constants and compressive strength

An inverse analysis of the calibration process for the discrete element simulation could be time-consuming and tedious as many micro-properties involved and each

parameter has its effect on macro-response of a synthetic material. The following sections describe how to match elastic properties, peak strength and crack initiation stress under uniaxial loading to minimize iterations for a parallel-bonded material.

As demonstrated previously, setting grain and bond stiffness equal to each other is an effective approach. Although previous study has showed that the each material macro-property could be affected by multiple micro-parameters, it's important to assume a one-to-one relationship. In this research we assume that Young's modulus is mainly governed by particle contact modulus (E_c), Poisson's ratio is dominated by contact stiffness ratio (k_n / k_s) and peak strength is controlled by bond strength ($\bar{\sigma}_b$ and $\bar{\tau}_b$) . By doing so a better understanding and more efficient calibration process could be obtained.

1. Determine geometric and physical parameters: sample characteristic length (L), particle size distribution ($R_{\max}$ *and* $R_{\min}$) , particle density (ρ). If a nonuniform particle size distribution is employed, the radius ratio should be set less than 2 to avoid unstable response and large variation. When considering the ratio L/R as a measure of the degree of discretization, the previous analysis has shown that special attention should be paid to the selection of L/R for the discrete media. For low L/R ratio the randomness packing of particle assembly leads to large variation of elastic constants and peak strength while on the other hand high L/R ratio requires more computational time. L/R larger than 120 or 50 is recommended for two-dimensional or three-dimensional model.
2. Determinate experimental parameter: loading velocity (v). In order to eliminate the inertial effects within the specimen and damage caused apply this velocity in a single step the platen acceleration should be applied in a controlled manner. If a static or quasi-static loading condition is desired the

dynamic effect should be prevented by following the previous discussion on dynamic increase factor. The loading velocity should be selected so that the overall strain rate is less than 0.1/s.

3. Selection of micro-parameters: Setting bond normal and shear strength ($\bar{\sigma}_b$ and $\bar{\tau}_b$) to large value and reproduce material Poisson's ratio (v) by changing stiffness ratio (k_n / k_s). Then varying contact modulus (E_c) to match material Young's modulus with a linear relationship can be expected. It is necessary to perform a few iterations to match both values. Match compressive strength by varying grain and bond normal and shear strength.

Figure 6.27 demonstrate that the stress-strain curve obtained from calibrated PFC model is in good agreement with experimental results.

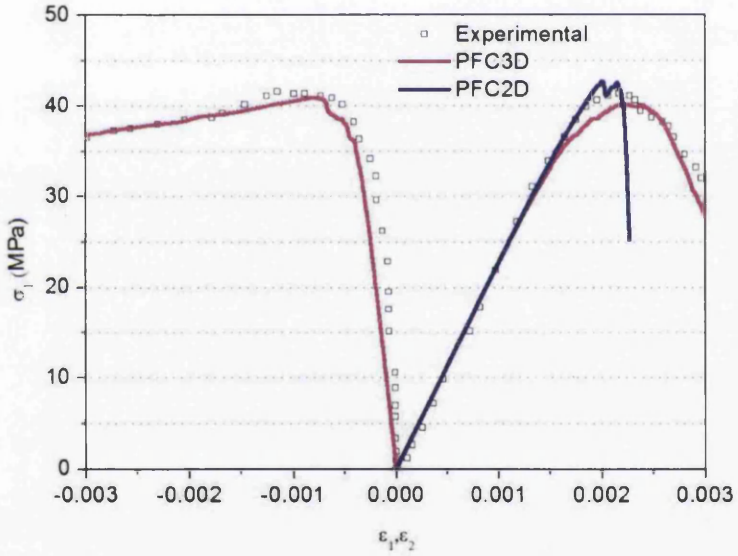

Figure 6.27: Stress-strain curves for uniaxial compressive test, experimental data (Tran *et al.*, 2011).

6.4 Conclusions

In this chapter, the influence of the micro constitutive parameters of the parallel-bonded PFC model in uniaxial compression was investigated. The findings can be summarized as follows:

- Young's modulus is mainly governed by contact modulus and stiffness ratio has the most significant influence on Poisson's ratio. Compressive strength is mainly governed by micro-tensile when the strength ratio is smaller than 0.5 and dominated by Micro-shear failure when the strength ratio is larger than 1.5 or 2 for 2D or 3D models.
- Failure mode and crack distribution is affected by the stiffness ratio and the bond strength ratio. Inclusion of both micro-shear and micro-tensile failure leads to more sophisticated damage modes.
- Introducing interface friction between specimen and loading platen increases the probability of reproducing shear bands and the hour-glass failure mode.
- Shape of post-peak stress-strain curve is mainly governed by loading velocity and increasing inter-particle friction has a minor effect.
- It should be noted that the relationships between micro-parameters and macro-properties obtained are empirical in nature. Modifications may be required for a specific problem. These quantitative relationships still provide valuable information such as the sensitivities of each microparameters and demonstrate the differences between 2D and 3D model.

References

Chang, C.S., 1993. Effective elastic moduli of heterogeneous granular solids. International Journal of Solids and Structures 30, 2547–2566.

Cho, N., Martin, C., Sego, D., 2007. A clumped particle model for rock. International Journal of Rock Mechanics and Mining Sciences 44, 997-1010.

del Viso, J.R., Carmona, J.R., Ruiz, G., 2008. Shape and size effects on the compressive strength of high-strength concrete. Cement and Concrete Research 38, 386-395.

Huang, H.Y., 1999. Discrete element modeling of tool-rock interaction. American: University of Minnesota.

Potyondy, D.O., Cundall, P.A., 2004. A bonded-particle model for rock. International Journal of Rock Mechanics and Mining Sciences 41, 1329-1364.

Tang, X., Zhou, Y., Zhang, C., Shi, J., 2010. Study on the Heterogeneity of Concrete and Its Failure Behavior Using the Equivalent Probabilistic Model. Journal of Materials in Civil Engineering 23, 402-413.

Tran, V.T., Donzé, F.V., Marin, P., 2011. A discrete element model of concrete under high triaxial loading. Cement and Concrete Composites 33, 936-948.

Vonk, R.A., 1993. A micromechanical investigation of concrete loaded in compression. Heron, 38(No 3)(1993).

Walton, K., 1986. The effective elastic moduli of a random packing of spheres. Journal of the Mechanics and Physics of Solid 35.

Wang, Y., Mora, P., 2008. Modeling Wing Crack Extension: Implications for the Ingredients of Discrete Element Model. Pure and Applied Geophysics 165, 609-620.

Yang, B., Jiao, Y., Lei, S., 2006. A study on the effects of microparameters on macroproperties for specimens created by bonded particles. Engineering Computations 23, 607-631.

Yoon, J., 2007. Application of experimental design and optimization to PFC model calibration in uniaxial compression simulation. International Journal of Rock Mechanics and Mining Sciences 44, 871-889.

Chapter 7

Meso-scale discrete element modelling of concrete

At the meso-level concrete is a three-phase composited synthetic material consisting of mortar matrix, aggregate and interfacial transition zone. Its overall physical and mechanical characteristics are significantly affected by the properties of each component phase. Utilizing the 2D random aggregate generation algorithm introduced in Chapter 3, aggregate structures are generated and projected onto a random particle assembly. A user-defined FISH program in particle flow code is developed and implemented in order to recognize the aggregate structures. As a quasi-brittle composite material, the aggregate and interface phase in all specimens are assumed to break in brittle and softening manner respectively. Both brittle and softening contact models are considered for mortar phase and the results are compared with each other. Concrete specimens with 40% and 60% aggregate content are investigated. Simulations of virtual notched three-point bending test are performed and the results including the complete load-CMOD response and fracture process are presented. The numerical predictions are verified against experimental observations followed by a brief discussion. It should be noticed that since random particle size is used, where all particle have different radius, thus, different stiffness and strength, disorder is already introduced at the 'geometrical' level.

7.1 Model configuration

The concrete beam geometry is $400\,mm \times 100\,mm \times 100\,mm$ and the notch size is 10 *mm* in depth and 3 *mm* in width. The concrete beam is discretized using random particle arrangement with minimum particle radii and size ratio 1 *mm* and 1.2 respectively. A total number of 8831 particles have been used in the simulation. A constant displacement rate of CMOD of 0.01mm/s is applied at the middle span, leading to an equivalent strain rate of 0.1/s which is slow enough to satisfy quasi-static loading conditions. During the simulations, the particle packing configuration is kept unchanged. Then by utilizing the polygonal aggregate generator introduced in Chapter 3 different aggregate structures are generated and projected onto the particle assembly.

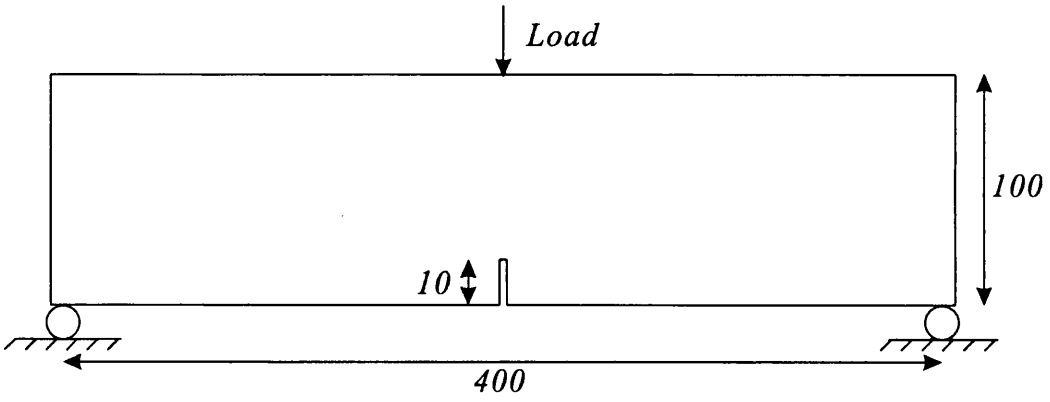

Figure 7.1: Three-point bending test setup and dimensions of concrete specimen.

Figure 7.2 illustrated a four-grade concrete specimen that consists of 60% coarse aggregate and the aggregate gradation curve is shown in Figure 7.3. The proportions of the coarsest to finest in the specimen are 3:3:2:2. The configuration aggregate structure can be easily controlled by specifying the lower and upper size limits and required the area or volume fraction of each grade. It should be noted that the actual aggregate fraction in the DEM model may be slightly different from the geometrical model due to the fact that the particle size is not infinitesimal as shown in Fig.7.4. An

assumption has been made in the analysis: All particles within a radius of 10 *mm* of notch tip are assumed belong to mortar phase. This simplification can avoid at the crack initiation stage.

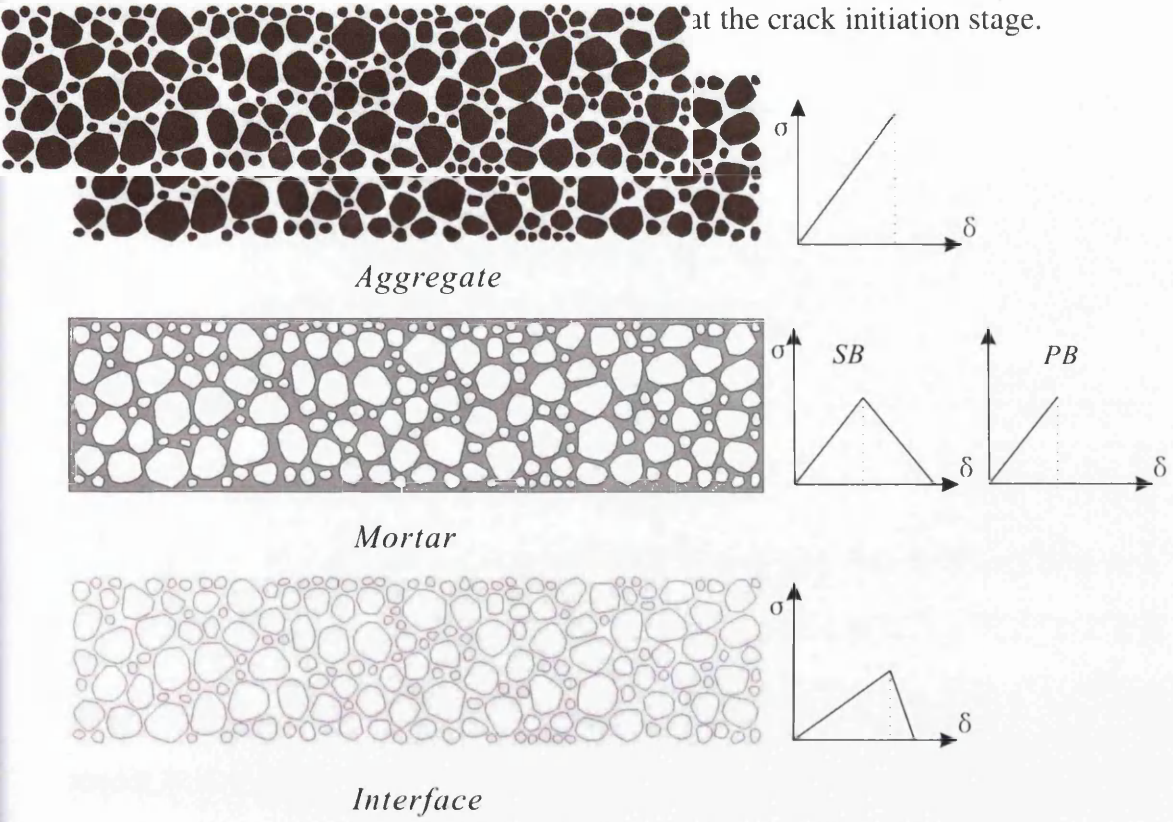

Figure 7.2: Geometrical and constitutive models for each material phase.

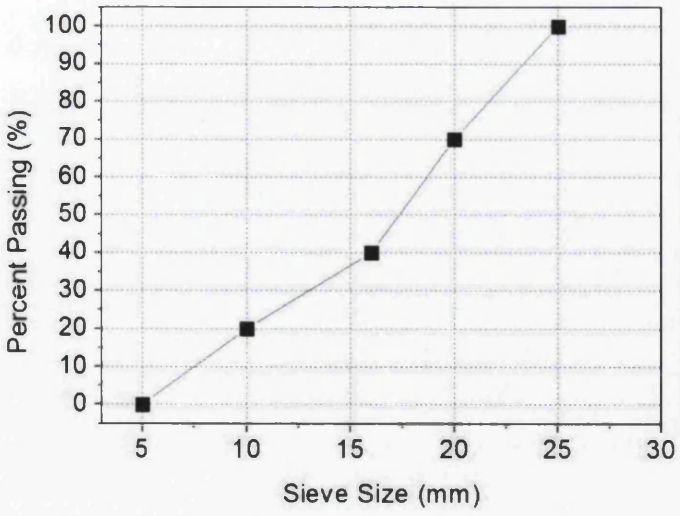

Aggregate number in each group

Range	Quantity
5-10	104
10-16	35
16-20	29
20-25	19

Figure 7.3: Aggregate gradation in four-grade concrete specimen.

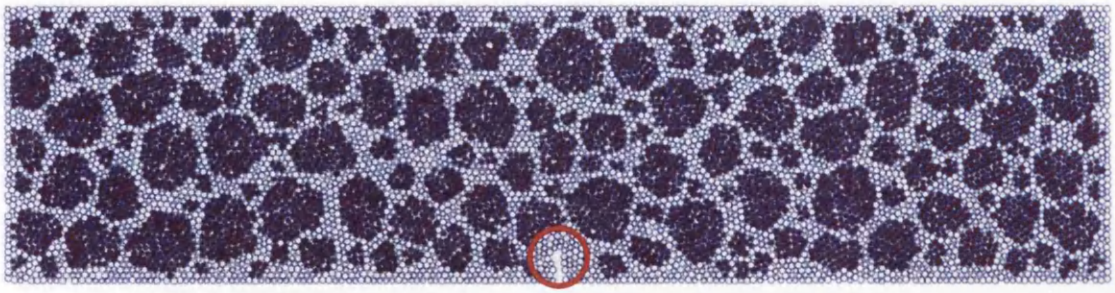

Figure 7.4: Four-grade concrete specimen in DEM model.

In the last chapter, the cement mortar specimen was treated as linear elastic material with brittle failure behaviour. However, some scholars (Bažant et al., 1990) suggests that concrete material displays some ductility after reaching its ultimate strength. Thus softening model such as cohesive zone model originally proposed by Hillerborg and co-workers (Hillerborg et al., 1976) has been widely adopted in FE analysis. The numerical predications have been proved to be very accurate for both Mode I and mixed mode loading (Elices et al., 2002). As the displacement softening contact model is very similar to cohesive zone model, both brittle parallel bond and bilinear displacement softening bond have been considered then a comparison study is performed.

One of the major challenge of modelling composite material such as concrete is determination of the appropriate mechanical relationship between each component materials, specially, the mechanical properties of interfaces. Various experimental investigations have been reported in the literatures. Depending on the types of concrete, the weakest component is different. The strength of coarse aggregates plays a different role in conventional concrete (compressive strength < 41 MPa) and high strength concrete. Conventional concrete mixtures typically correspond to a water-cement ratio in the range of 0.5-0.7. Within this range, the weakest components are the transition zone between the mortar and the coarse aggregate (Mehta, 1986; Zhi Yuan and Jian Guo, 1987). Unless the aggregate contains some constituents (e.g. reactive silica mineral), the mineralogy of coarse aggregate is rarely of concern

(Aitcin and Mehta, 1990). On the other hand, researchers have noted that the strength of the coarse aggregate control the ultimate strength of concrete rather than mortar and transition zone (Neville, 1995).

In the field of conventional concrete, Wong (Wong et al., 1999) utilized notched three-point bending test to investigated the mechanical properties of mortar-aggregate interface and found that the flexural strength of interface is one third of mortar flexural strength; Rao (Rao and Prasad, 2002) reached a similar conclusion by performing tensile tests on sandwiched composites specimens.

Experimental investigations on mortar-aggregate interfacial fracture energy (e.g., three-point bending test by Wong (Wong et al., 1999), the aggregate push out test by Mistui et al. (Mitsui et al., 1994) and the wedge splitting test by Tschegg et al.(Tschegg et al., 1995)) indicate that the interfacial fracture energy is only about 10% of the corresponding mortar fracture energy.

In this study we assume that the aggregate type is hard limestone with the ratio 9:3:1 for the aggregate to matrix to interface strength. The material properties adopted in the calculation are given in Table 7.1 where the Poisson's ratio of mortar and aggregate is taken to be 0.16 and 0.22 respectively. The micro-parameters of DEM model are calibrated by performing virtual tensile tests on each component phase and then incorporated in the later simulations.

Table 7.1: . The macro material properties adopted in the analysis

Material	Young's modulus (GPa)	Fracture energy (N/m)	Tensile strength (MPa)
Aggregate	70	-	9.6
Mortar	35	170.4	3.2
Interface	25	18	1.1

7.2 Results and discussions

7.2.1 Load-CMOD response

The results presented in Fig.7.5 indicate that the numerical predictions of both parallel bond and softening bond models are capable of reproducing reasonable load-CMOD response during the three-point bending test. Despite the assumed brittleness of local bond, global softening can be obtained in brittle model. Five loading phases can be identified: in the early stage of loading, the load-CMOD response is almost linear elastic and the deformation is uniformly distributed along the whole specimen; As the microcracks distributed within the concrete, the curves becomes nonlinear; maximum load; steep softening stage; shallow softening stage. Overall the softening model provides a better predictions than the brittle model.

In the ascending branch of brittle model load-CMOD curve the nonlinear portion of the curve appears to be very short which implies that the predicted cracking strength (which is defined as the stress level at which crack starts to propagate in the present study) is slightly higher than expected. This defect can be overcome by incorporating probabilistic model (e.g., assuming the phase material properties conform to the Weibull distribution law, as demonstrated in Chapter 4 and Chapter 6, the non-linear and softening behavior of concrete can be controlled by specifying appropriate heterogeneity index). On the other hand, up to ultimate flexural strength, a very good agreement between the softening model and that experimental data was established. However, the brittle model leads to closer predictions of the ultimate load. The softening model slightly underestimates the peak load and overestimates the corresponding displacement.

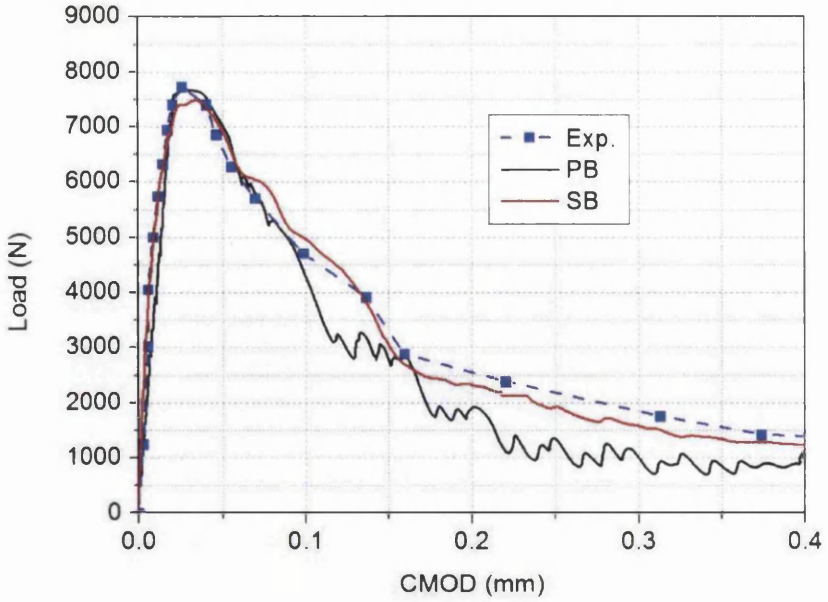

Figure 7.5: Numerical predictions and experimental results (Zhang et al., 2005) of load-COMD curves.

The descending branch of load-CMOD curve consists of a steep softening stage and a relative shallow softening stage. The post-peak load-CMOD curve of the parallel model fluctuations, and strengthening appears due to the local instability. This disturbance is probably caused by different rupture behaviors of component materials. It has been found that that softening model exhibits the same fluctuations and strengthening when reducing the maximum plastic displacement allowance in local contact model. This unstable response can be reduced by increasing model resolution and slowing down the loading velocities, but in a consequence that a much higher computing cost is required (e.g., Kim et al. (Kim et al., 2009)).

As the load-CMOD curve is obtained, the fracture energy can be evaluated by computing the area under the curve. The fracture energy value and the residual strength for brittle model are lower than the experimental data.

7.2.2 Crack propagation

Two different four-grade concrete specimens consisting of 40% and 60% aggregate were investigated. Fig.7.6 indicates the amount of contacts in each component

material for two specimens. It can be seen that 60% specimen contains more the strongest (aggregates) and weakest links (interfaces). The dynamic crack propagation processes is shown in Figs. 8.7 and 8.8.

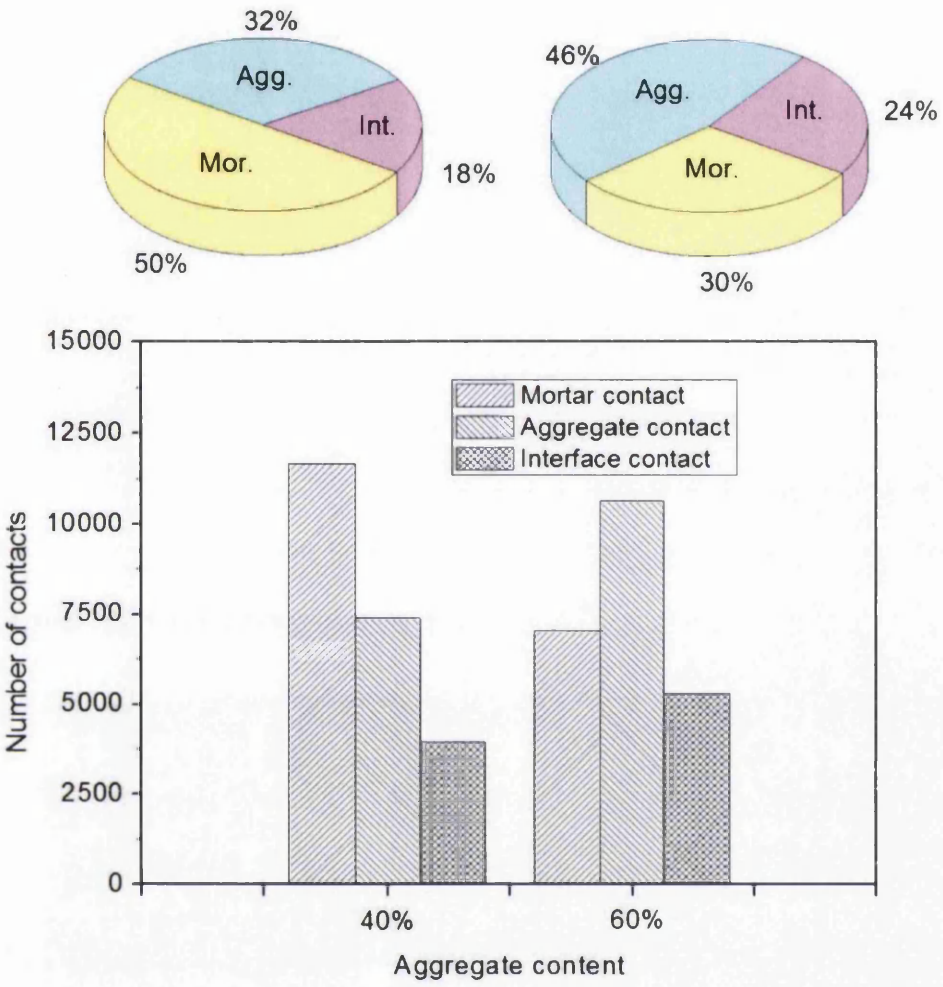

Figure 7.6: Relationship between the amount of contacts in each component material.

The crack preparation is naturally captured in DEM by means of debonding of particles. The crack path is color coded to distinguish the location where a crack is situated, i.e. in the mortar, aggregate or interface. When the applied force excesses the bond strength, the brittle bonds fail immediately and this breakage is denoted by a magenta line. Softening bonds yield when their strength exceed, any further force leads to plastic deformations (black lines) until complete failure (black lines replaced by red lines).

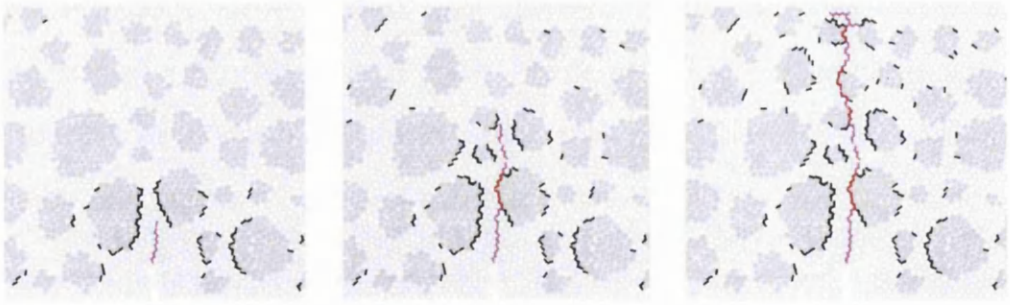

(a) Brittle model

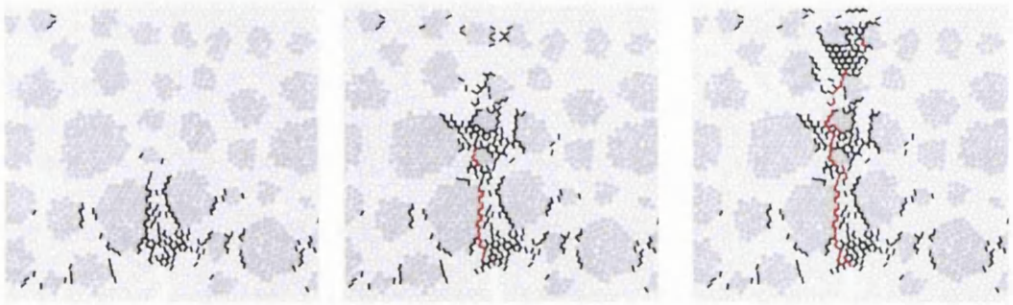

(b) Softening model

Figure 7.7: Crack propagation in concrete specimen consisting of 40% aggregate.

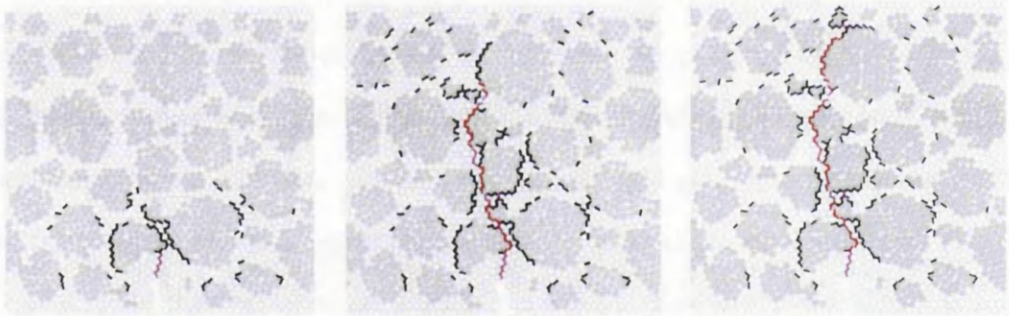

(a) Brittle model

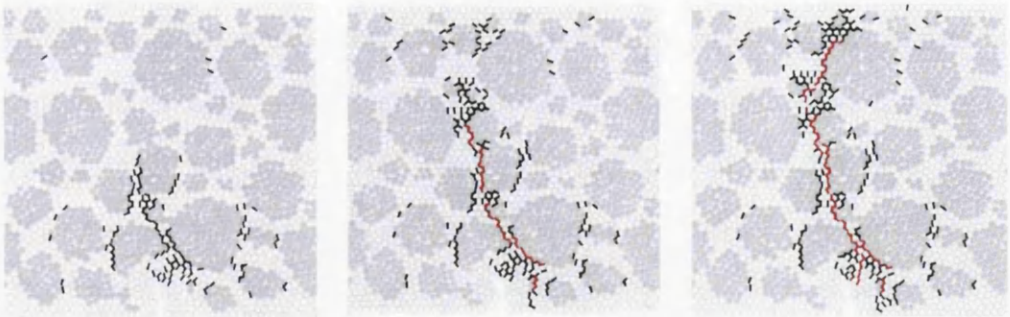

(b) Softening model

Figure 7.8: Crack propagation in concrete specimen consisting of 60% aggregate.

Since the models were notched and therefore, as the load increases, stress concentrates near the tip of initial notch. Plastic deformation starts to accumulate. This interface or mortar bonds plastic deformation is the cause of the considerable non-linear behaviour in the pre-peak part of the load-CMOD curve.

Just after the peak load, a sharp decrease in the load carrying capacity is observed as complete local bond breakages take place. In the brittle model, complete bond breakages first take place at the mortar phase while interface bond failure occures first in the softening model.

In the brittle model, further load leads to the growth of the initial damage in the mortar phase, the direction of the cracking depends on the local contact forces and bond strength. Interfacial bonds yielding in the region just ahead of the crack tip always occurs before the macrocrack passes or parapogates towards the aggregates. The presence of aggragete blocks or alters the crack development significantly. It is well known that when concrete is loaded cracks prefer to propagate along the weaker phase. When the macro crack meets an aggregate, it is forced either to propagate throught the touher aggregate or deflect and travel around the interface. Since the interface toughtness is lower than the matrix and aggregate, the advancing crack is prone to travel around the aggregate resulting in a tortuous cracking path. The final crack path of britlle specimens in Figs.7.7 and 7.8 is denoted as a single line joined toghter by magenta (mortar bond failure) and red (interface bond failure) segments. Comparing the crack path between the 40% and 60% specimens, the crack path in the 60% speciemn is more tortuous and consists of more interfacial debondings than the 40% specimen (Fig.7.9) for two reasons: Firstly, due to the fact that the 60% specimen consists of more interface bonds; secondly, the 40% specimen has more space and freedom between the aggregates, the chance of cracking penetrates through the martor phase instead of joining the interfaces is higher.

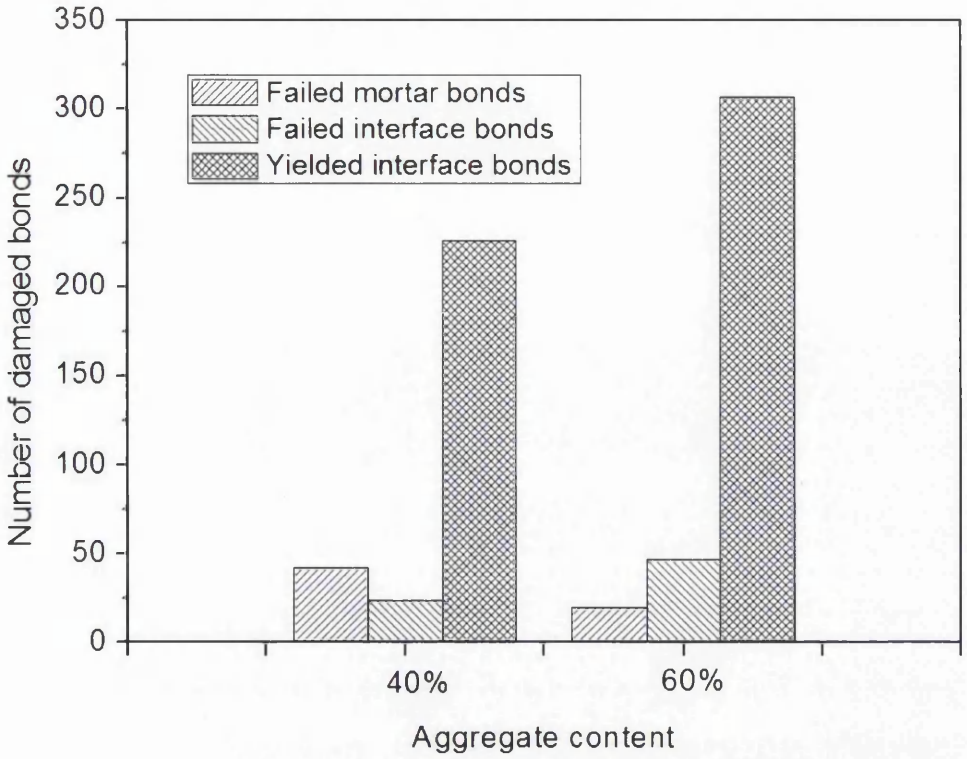

Figure 7.9: Damage in brittle models.

The softening model predicts a rather different fracture process: micro cracks first take place at the interfacial transition zone then propagate along the interface. Just before the peak load is reached, mortar cracks start to develop and then join the interface cracks to form the final damage pattern. These observations are in better agreement with the experimental findings (Lilliu and van Mier, 2007) for uniaxial tension than the brittle model.

7.3 Conclusions

Meso-level DE model, with both linear elastic-purely-brittle and softening failure laws were adopted for simulating the fracture process of concrete specimens in three-point bending test. The DE model is intended to provide insight into the fracture behaviour of concrete. The virtual specimen of concrete was conceived as a three-phase material, composed of mortar matrix, aggregates and an interfacial

transition zone. In the present study, concrete is modeled at meso-level: the aggregates were represented as polygons and their distribution obeys a Fuller curve. The aggregate diameters ranging from 5 to 25 mm were employed for all aggregate contents. Results including the complete load-CMOD curve and fracture process have been analyzed and discussed. Both brittle and softening models obtained reasonable results compared to experimental observation. However, the results suggest that the softening model leads to more realistic predictions than linear elastic-purely-brittle model. The multi-grade polygon aggregates generation algorithm have been successfully implemented and proved to be reliable and efficient for the multi scale simulations.

Based on these encouraging results, the DE model developed can be extended to investigate more sophisticated problems, such as the effect of aggregate size distribution, content, types and shape on the mechanical properties, load-deformation relationship and damage behavior of normal or high strength concrete under various loading conditions. With better computer infrastructures becoming available, 3D models can be implemented and it is reasonable to expect that more realistic numerical results will be obtained.

Reference

Aitcin, P., Mehta, P., 1990. Effect of coarse aggregate characteristics on mechanical properties of high-strength concrete. ACI Materials Journal 87.

Bažant, Z., Tabbara, M., Kazemi, M., Pijaudier - Cabot, G., 1990. Random particle model for fracture of aggregate or fiber composites. Journal of engineering mechanics 116, 1686–1705.

Elices, M., Guinea, G.V., Gómez, J., Planas, J., 2002. The cohesive zone model: advantages, limitations and challenges. Engineering Fracture Mechanics 69, 137-163.

Hillerborg, A., Modéer, M., Petersson, P.-E., 1976. Analysis of crack formation and crack growth in concrete by means of fracture mechanics and finite elements. Cement and concrete research 6, 773-781.

Kim, H., Wagoner, M.P., Buttlar, W.G., 2009. Micromechanical fracture modeling of asphalt concrete using a single-edge notched beam test. Materials and structures 42, 677-689.

Lilliu, G., van Mier, J.G.M., 2007. On the relative use of micro-mechanical lattice analysis of 3-phase particle composites. Engineering Fracture Mechanics 74, 1174-1189.

Mehta, P.K., 1986. Concrete. Structure, properties and materials.

Mitsui, K., Li, Z., Lange, D.A., Shah, S.P., 1994. Relationship Between Microstructure and Mechanical Properties of Paste-Aggregate Interface. ACI Materials Journal 91.

Neville, A.M., 1995. Properties of concrete.

Rao, G.A., Prasad, B., 2002. Influence of the roughness of aggregate surface on the interface bond strength. Cement and concrete research 32, 253-257.

Tschegg, E., Rotter, H., Roelfstra, P., Bourgund, U., Jussel, P., 1995. Fracture mechanical behavior of aggregate-cement matrix interfaces. Journal of materials in civil engineering 7, 199-203.

Wong, Y., Lam, L., Poon, C., Zhou, F., 1999. Properties of fly ash-modified cement mortar-aggregate interfaces. Cement and concrete research 29, 1905-1913.

Zhang, J., Liu, Q., Wang, L., 2005. Effect of Coarse Aggregate Size on Relationship between Stress and Crack Opening in Normal and High Strength Concretes. J. Mater. Sci. Technol 21, 691-700.

Zhi Yuan, C., Jian Guo, W., 1987. Bond between marble and cement paste. Cement and concrete research 17, 544-552.

Chapter 8

DEM modelling of debonding in FRP-to-concrete interface

Fiber reinforced polymer (FRP) laminates are being successfully adopted for strengthening of existing reinforced concrete (RC) and prestressed concrete (PC) structures. The interface between the external FRP reinforcement and the concrete substrate is of critical importance for the effectiveness of the technique, since it is the means for the transfer of stresses between concrete and FRP in order to develop composite action (De Lorenzis et al., 2001). A number of failure modes in FRP-strengthened RC members are directly caused by debonding of the FRP from the concrete (Sebastian, 2001; Smith and Teng, 2002). Therefore, understanding of the fracture behaviour of FRP-to-concrete interfaces is essential for safe and economic design of externally bonded FRP systems.

Yuan et al. (Yuan et al., 2004) proposed that if it is assumed that both concrete and FRP are only subjected to axial forces and any bending effect is neglected, the debonding would be dominated by mode II fracture. The stress state of the interface is similar to that in a pull test specimen in which a plate is bonded to a concrete prism and is subjected to tension (Fig.8.1). Extensive experimental and theoretical works have been conducted based on pull tests on bonded joints. Most of theoretical solutions were based on Cohesive Zone Model. According to different global

traction-separation laws assumed, the analytical solutions can be classified as linear, bilinear, and nonlinear models (Wang, 2006, 2007). Most of the experimental investigations were carried out using the mode II single or double shear test to characterize the traction-separation law, with mounted strain gages on top of the bonded FRP laminate. Empirical equations have been reported in numerous literatures (Ferracuti, 2006; Popovics, 1973).

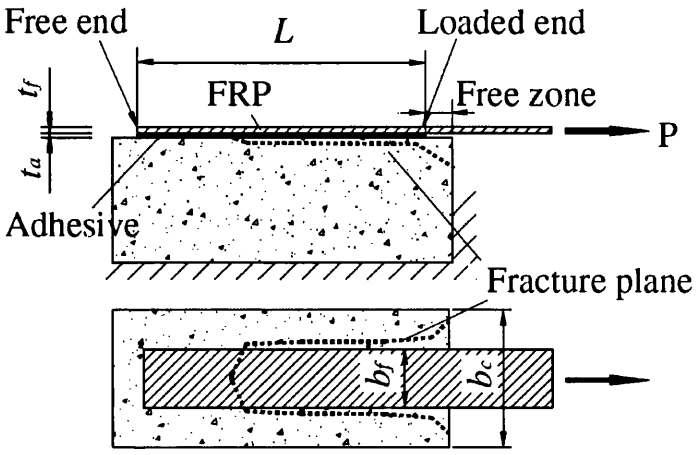

Figure 8.1: Schematic of a pull test (Lu et al., 2006).

Besides experimental and theoretical studies, numerical methods particularly finite element method have also been used to study debonding in FRP-to-concrete interface. From early linear elastic FE analysis (Teng et al., 2002) to more recently development of nonlinear analysis, the FE analysis aimed at the simulation of the entire debonding process. However, the accuracy of FE simulation highly depend on the definition of a correct interface law and its unknown parameters require extensive calibration. Furthermore, the crack propagation has to be predefined according to experimental investigations.

In this chapter, taking the full advantage of intrinsic characteristics of DEM, the dynamic failure process in the FRP-to-concrete interface is simulated. Displacement softening model is used to represent the FRP-to-concrete interface. The heterogeneity of concrete is taken into account statistically by utilizing the Weibull distribution to micro-parameters.

8.1 Discrete element modelling of pull test

A typical delamination test setup and DEM model is shown in Fig.8.2a. DE model with 50 *mm* bonded length and 100 *mm* free zone is adopted to enable comparison of numerical results with experimental results conducted by Mazzontti *et al* (Mazzotti et al., 2008). The height of the concrete prism modeled is only 30 mm, as the lower part of the concrete prism is not believed to exert a significant effect on the result.

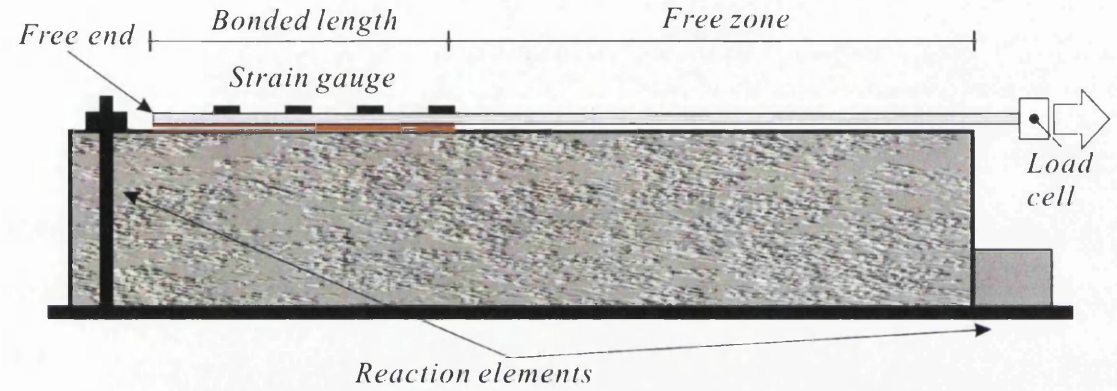

(a) Typical delamination test setup

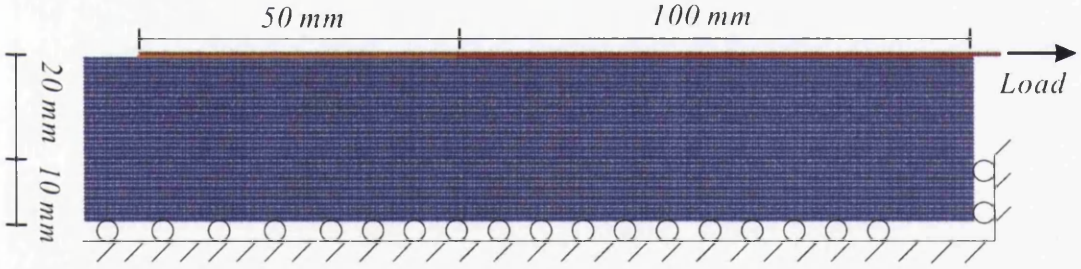

(b) Discrete element model

Figure 8.2: Typical experiment setup and DEM model configuration for delamination test.

Meso-scale simulation of full scale experimental data requires extensive computing effort as the concrete specimen height to thickness of FRP sheet ratio is relatively large. The 1.2 mm thick FRP sheet is modeled as a single layer of particles in six-particle hexagonal packing arrangement. The particle size is uniformly distributed over specimen and has a radii value of 0.2 *mm*. A total of 35561 particles and 105308

contacts are arranged according to the hexagonal particle arrangement. A total of 1161 particles are labeled as FRP, 34400 particles are labeled as concrete, and 125 contacts are used to represent the adhesive interfaces between FRP and the concrete.

In experimental test, concrete block is positioned on a rigid frame with two steel reaction elements in order to prevent horizontal and vertical displacements. In DE model, boundary conditions are applied to restrict of the horizontal movement in the right end of concrete specimen and the vertical movement in the low end of concrete. Simulations are carried out under control of loaded end displacement and the final displacement rate, $1\mu m / s$, is applied to the loading end of FRP in a controlled fashion to neglect possible inertia effect. The applied traction force is recorded by computing the out-of-balance forces at loading particles. A series of strain gauge is installed to record longitudinal strains. The position of these gauges start from the starting end of adhesive layer and distributed uniformly over the bonded FRP sheet.

In this study, the pull test is simulated as a 2D problem, but in reality, the width of the FRP plate and that of the concrete specimen may be different (the width of FRP sheet and concrete specimen is 50 *mm* and 80 *mm*.in this study). In comparing DE predications with experimental results, the numerical simulation results should be adjusted by the following width ratio factor β_w proposed by Chen and Teng (Chen and Teng, 2001).

$$\beta_w = \sqrt{\frac{2 - b_f / b_c}{1 + b_f / b_c}} \tag{8.1}$$

where b_f and b_c are the widths of FRP plate and the concrete specimen, respectively. The adjustment involves the multiplication of a factor to the simulated values of the applied load and the stress and strain in the FRP plate based on the relationship of Eq.8.1.

8.1.1 Hexagonal packing arrangement

In discrete element modeling, the material is generally discretized by adopting one of particle arrangements in Figure 8.3 (Chang et al., 2002). The square arrangement is very simple to implement. However, material response may be inadequate due to the inability of this packing arrangement to generate a Poisson's effect (theoretically, the Poisson's ratio of this packing arrangement is zero.) (Mustoe and Griffiths, 1998). The random arrangement is the closest to the real material in which Poisson's effect and random crack paths can be included. Difficulties will be encountered when particle radius appears in local contact or bond model formulation (e.g. parallel bond model and contact softening model). Hexagonal packing arrangement has nearly the same benefits as the random packing and a directly relationship between micro-parameters and material properties (i.e., Young's modulus and Poisson's ratio) has been reported and verified in the literatures. Therefore, the hexagonal packing arrangement is adopted in the simulations presented in the present study.

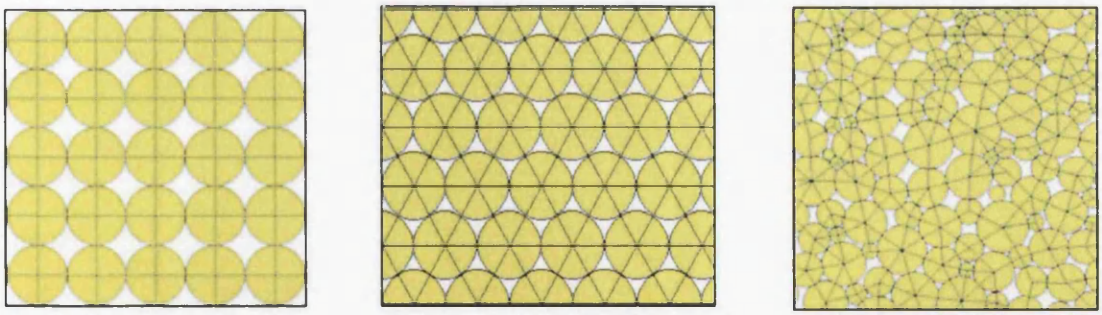

(a) Square (b) Hexagonal (c) Random

Figure 8.3: Common packing arrangements for discrete element modeling (Kim et al., 2008).

Based on strain energy and two-dimensional Hooke's law the relationship between elastic properties and stiffness of particles in contact have been obtained by numerous scholars. Sawamoto (Sawamoto et al., 1998), Kim (Kim et al., 2008), and Taverez (Tavarez and Plesha, 2007) derived equations for isotropic materials while Liu (Liu et al., 2004; Liu and Liu, 2006) concluded a general formula for anisotropic and

isotropic materials. Validity and accuracy of each formula and DEM models have been demonstrated by performing DEM simulation and comparing numerical results to the theoretical solution, continua approach (e.g., FEM, FVM) or experimental data. Considering discrete isotropic materials into hexagonal packed particle assembly with unite thickness:

Plane strain

$$K^n = \frac{E}{\sqrt{3}(1+\nu)(1-2\nu)}$$
$$K^s = \frac{E(1-4\nu)}{\sqrt{3}(1+\nu)(1-2\nu)} \tag{8.2}$$

Plane stress

$$K^n = \frac{E}{\sqrt{3}(1-\nu)}$$
$$K^s = \frac{E(1-3\nu)}{\sqrt{3}(1-\nu^2)} \tag{8.3}$$

8.1.2 Heterogeneity characterization of concrete material

As pointed out by Wittmann (Wittmann, 1983), concrete is a typical multi-scale material with different structural details appearing at different levels of observation, so the research of concrete material have been focused mainly on these three distinct levels, namely the micro, meso- and macro-level. The meso-level was generally considered to be 10^{-3} m when we study the laboratory scale responses of concrete (Van Mier and Van Vliet, 1999). At the macro-level, the concrete is generally assumed to be a homogeneous material. In order to characteristic the heterogeneity and discrete nature of the internal structure of concrete, micro-parameters are assigned to each particle and bond drawing from given Weibull distribution. The probability density function of a Weibull random variable x can be expressed as:

$$f(x;\ \lambda, k)=\frac{k}{\lambda}(\frac{x}{\lambda})^{k-1}e^{-(x/\lambda)^k} \tag{8.4}$$

where x denotes material properties (i.e. modulus and strength); λ is the scale parameter of the distribution which is related to the average value of material properties; κ is the shape parameter defining the shape of the Weibull probability density function. The micro constitutive parameters of each component phase are randomly assigned to particles and bonds from the pre-defined Weibull distribution. Figure 8.4 shows the Weibull probability density function with different parameters where the shape parameter reflects dispersion of concrete material properties. When increasing shape parameter the distribution of micro parameters becomes centralized around the scale parameter λ. Shape parameter k can be seen as a measurement of material homogeneous degree, a large value of k leads to a more homogeneous material.

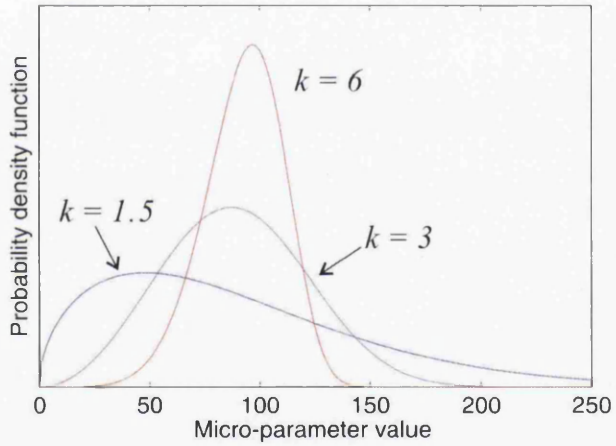

Figure 8.4: Micro-parameter probability density functions with various shape parameters.

8.1.3 Calibration of material phase

The DEM model of delamination test consists of three material components: FRP sheet, concrete and interface zone between FRP and concrete. FRP and concrete materials are modeled as particles packed in hexagonal arrangement as shown in Fig.8.5. Different local constitutive models are adopted for different components in

which both FRP sheet and concrete particles are bonded by parallel bonds. Although, the FRP sheet exhibits elastic-plastic behavior, the elastic parallel bond models can rarely account for the plastic deformation. Softening model seems to be more appropriate chosen, however, it is reasonable to argue that the tensile strength of FRP is always much larger than concrete and interface strength and the failure of delamination test is mainly governed by debonding of FRP and concrete interface. Thus, the linear elastic assumption for the FRP sheet is sufficient. The epoxy adhesive layer is treated as contacts between FRP and concrete particles contact while displacement softening model is applied at each contact. Both parallel bond and displacement softening constitutive behaviors are described in Chapter 3. The heterogeneity of concrete material is taken into account statistically by applying the Weibull distribution to micro-parameters.

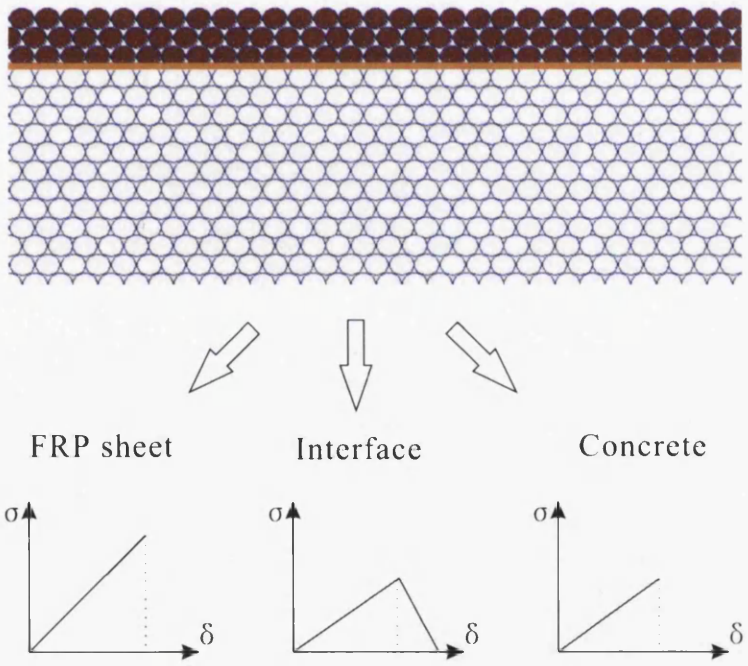

Figure 8.5: FRP interface and concrete in DEM model.

It's has been found that the theoretical equations derived by Kim *et al* exhibited size dependence and could not guarantee an accurate prediction of micro-parameters for all circumstances. Thus, an inverse analysis based on virtual simulation laboratory tests is still required to obtain the desired macro mechanical properties. Compressive

and tension tests are carried out on concrete and FRP materials respectively.

The material properties are shown in Table 8.1 according to the experimental study carried out by Mazzotti *et al* (Mazzotti et al., 2008). $50\times1.2\,mm$ FRP and $60\times30\,mm$ concrete specimen is utilized in virtual tension and compression tests respectively. The calibrated stress-strain curves are shown in Figs. 8.6 and 8.7. The tensile strength of FRP sheet is set to a large value to prevent any bond breakage. Then the calibrated micro-parameters for different material phases then are applied to benchmark delamination simulation.

Table 8.1: Macro properties of each component material.

Concrete compressive strength	52.6MPa
Concrete tensile strength	3.81MPa
Concrete Young's modulus	30.7GPa
Concrete Poisson's ratio	0.23
FRP Young's modulus	195.2GPa
FRP tensile strength	Infinite
Interfacial tensile strength	30.2MPa
Interfacial elastic modulus	12.8GPa
Interfacial fracture energy (mode II)	525.1 N/m

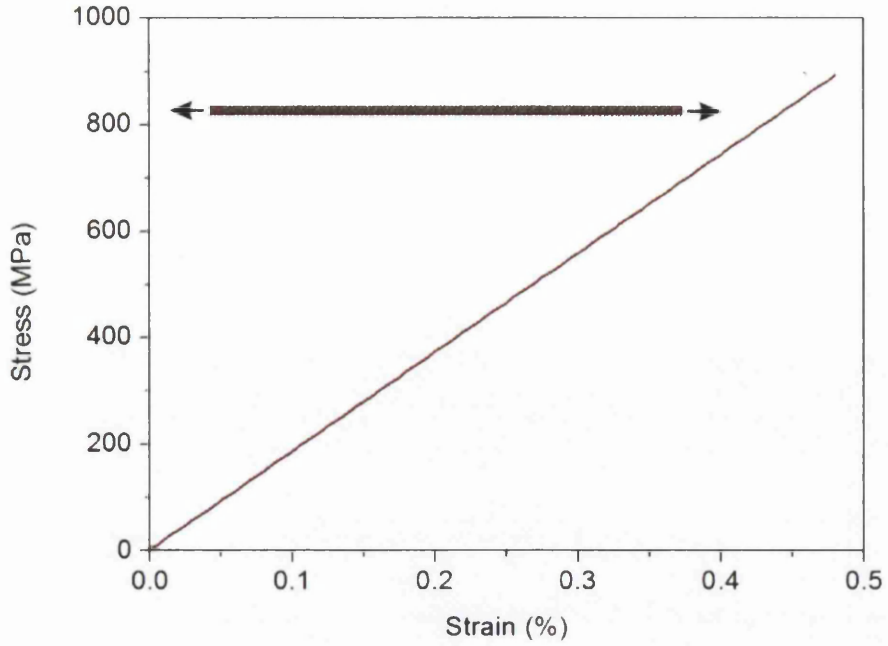

Figure 8.6: Stress-strain curve in DEM simulation of FRP tension test.

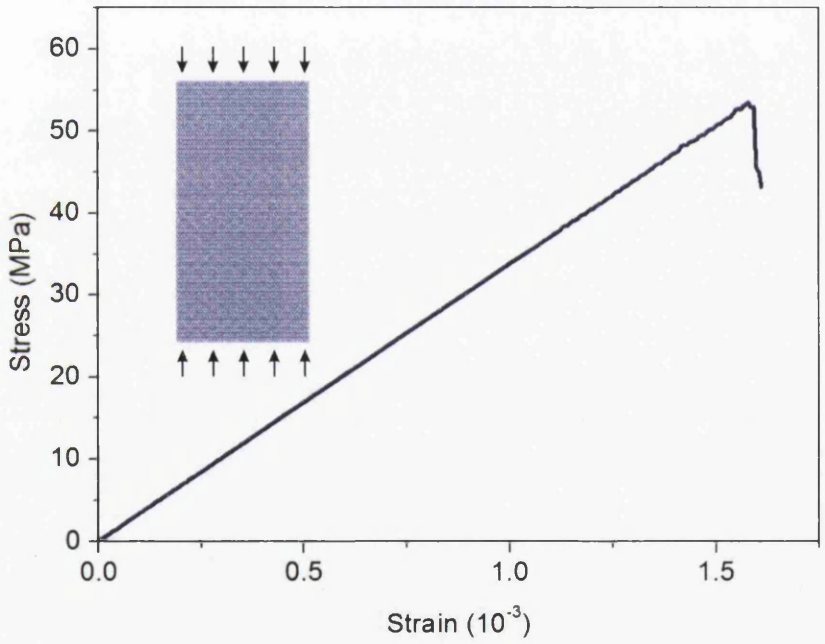

Figure 8.7: Stress-strain curve in DEM simulation of concrete compressive test.

8.2 Results and discussions

8.2.1 Strain distribution in FRP

During numerical simulation strain distribution in the FRP plate are recorded at various loading level and four of them (4KN, 8KN, 12KN and 14 KN) have been selected to compare with experimental results. Fig.8.8 illustrates the comparisons of strain distribution in the FRP plate between the numerical results and the test results from (Mazzotti et al., 2008) where the strains at 0 are calculated from values of the applied force as:

$$\varepsilon_0 = \frac{F}{E_p t_p b_p} \tag{8.5}$$

A good agreement with experimental and FE model results can be found.

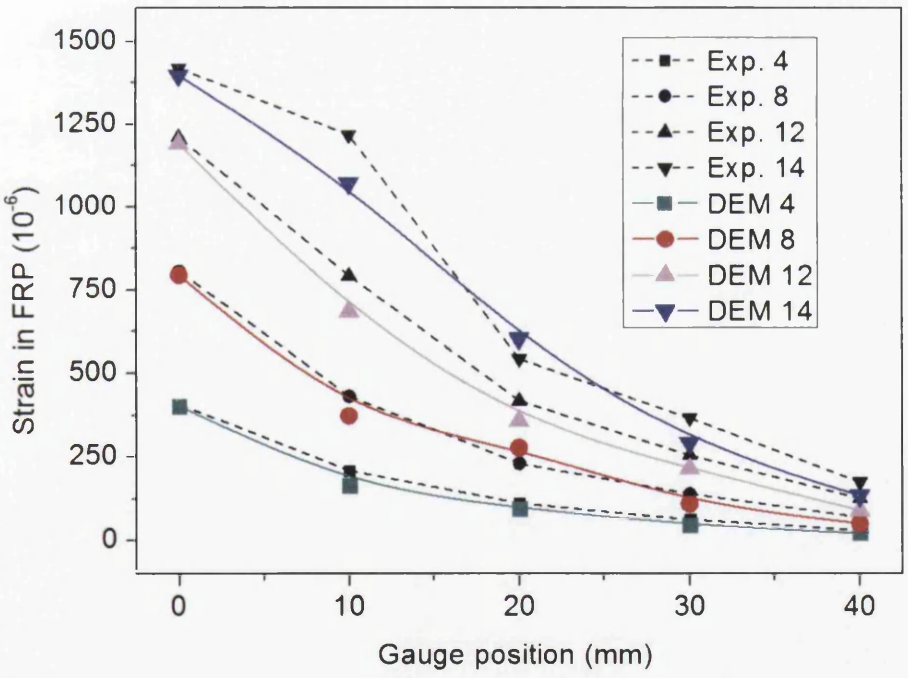

Figure 8.8: Comparison of test and DE strain distribution in the FRP plate.

8.2.2 Load-carrying capacity

An important feature of the behaviour of the bonded joints is that there exists an effective bond length beyond which an extension of the bond length cannot increase the ultimate load. This is a fundamental difference between an externally bonded plate and an internal reinforcing bar for which a sufficiently long anchorage length can always be found so that the full tensile strength of the reinforcement can be achieved. Parametric study on the load-carrying capacity is conducted by varying the boned length. Fig.8.9 indicates that the load-carrying capacity is a function of the bonded length and the increase of loading-carrying capacity slows down when the bond length reaches 100 mm. The difference between the DE model results and the experimental observation within a reasonable range. Both comparisons suggest that the DE model proposed in this study can correctly simulate the debonding process.

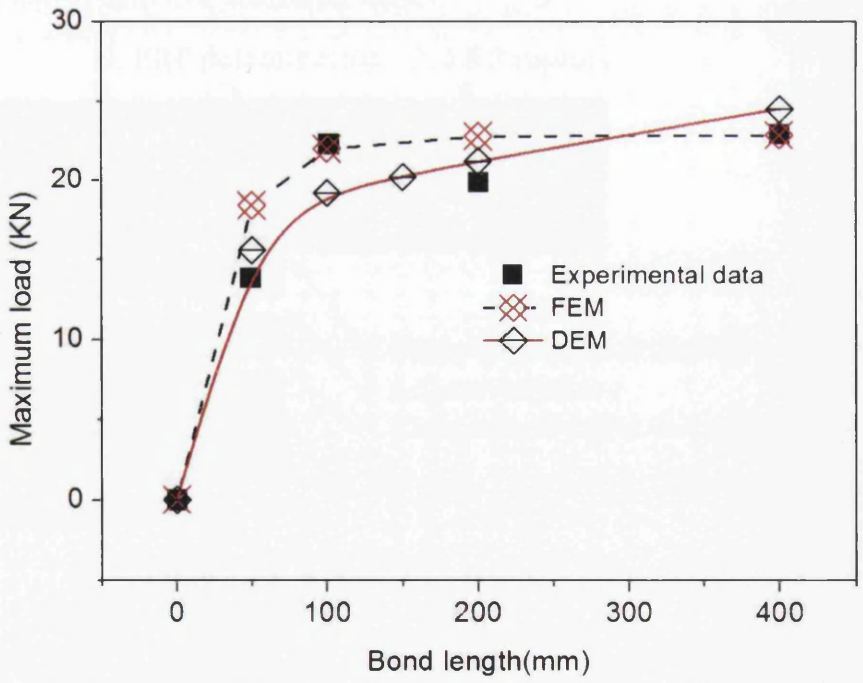

Figure 8.9: Load-carrying capacity verse bonded length: experimental results, FE results, and DE results.

8.2.3 Failure progression

When a plate is bonded to a concrete specimen and is subject to axial loading up to failure (i.e., in tangential direction with respect to the interface), Mode II shear failure occurs (Bažant and Pfeiffer, 1986). For single or double shear tests, there are six possible distinct failure modes in theory for an FRP or steel plate bonded to concrete, although they may be mixed in an actual failure. These are listed below in the order of their likeliness, based on existing test data (Chen and Teng, 2001) and a schematic view of failure modes is shown in Fig.8.10.

1. Concrete failure
2. Plate tensile failure including FRP rupture
3. Adhesive failure
4. FRP delamination for FRP-to-concrete joints
5. Concrete-to-adhesive interfacial failure
6. Plate-to-adhesive interfacial failure

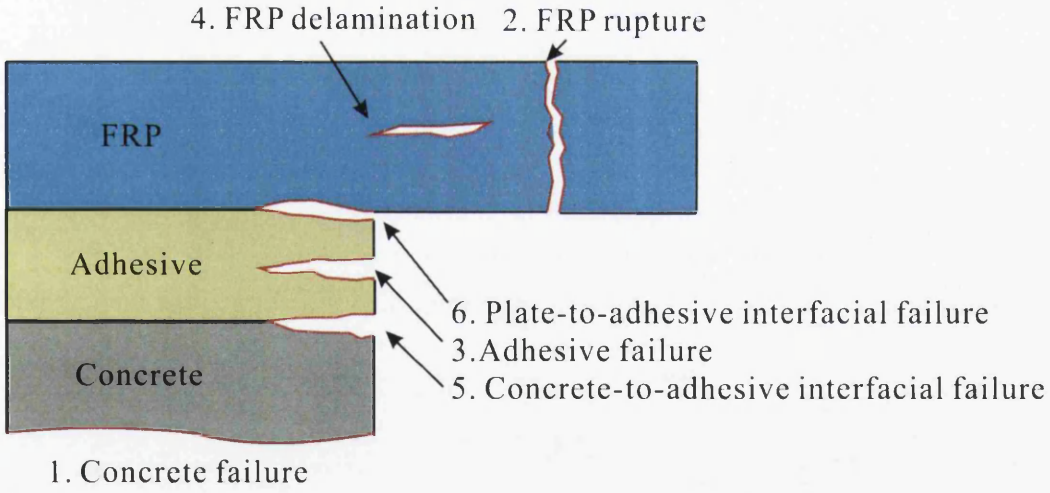

Figure 8.10: Schematic view of failure modes.

Literature survey indicates that most experimental joints fail in the concrete part. Adhesive and interfacial failure, between either the adhesive and the concrete or the adhesive and the FRP, is rare. Because of the availability of strong adhesives that bond well to FRP and concrete. For this study, the adhesive has a much higher tensile

strength than the concrete (about 8 times) and smaller elastic modulus (about 40%), so under the same deformation, concrete cracking occurs first. As a result, the failure process can be expected to depend strongly on the initial and propagation of cracking in the concrete.

With the increase of the applied load, a concentration of contact force is developed at the beginning point of the anchorage. When this contact force reaches the strength of concrete, micro-cracking occurs by means of local bond breakage. As the micro-cracking grows, this concentration of contact force shifts with crack tip as indicated by the red lines in Fig.8.11. Crack is initiated a few millimeter beneath the FRP and the adhesive layer in the concrete substrate at every early loading stage, where most of the concrete is still in elastic range. When the load increases to 31% of the ultimate load, the cracking region becomes larger and micro-cracks can be observed in a deeper level of concrete. As the load continues to increase the cracking region continues to propagate. Depending on the local bond strength of concrete particles, traverse crack appears and propagates towards the deeper level of concrete. As the applied load increases to 92% of load-capacity, the cracking region spreads over the whole bond length and a transverse crack appears near the free end of the bonded region. Eventually, the FRP sheet is deboned from concrete with a thin layer of concrete attached to it. Comparing numerical results with experimental finding obtained by Wu and Jiang in Fig.8.13, it is clearly that the developed model validated.

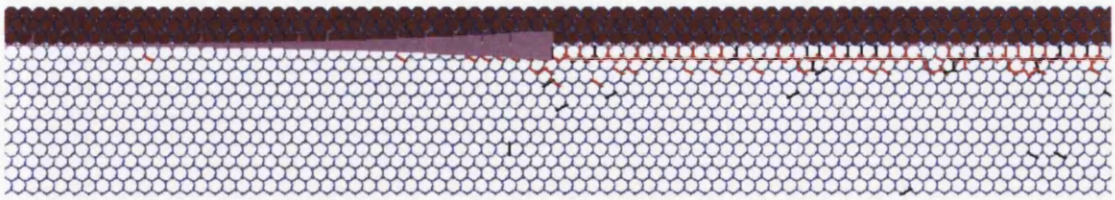

Figure 8.11: Contact force at crack tip.

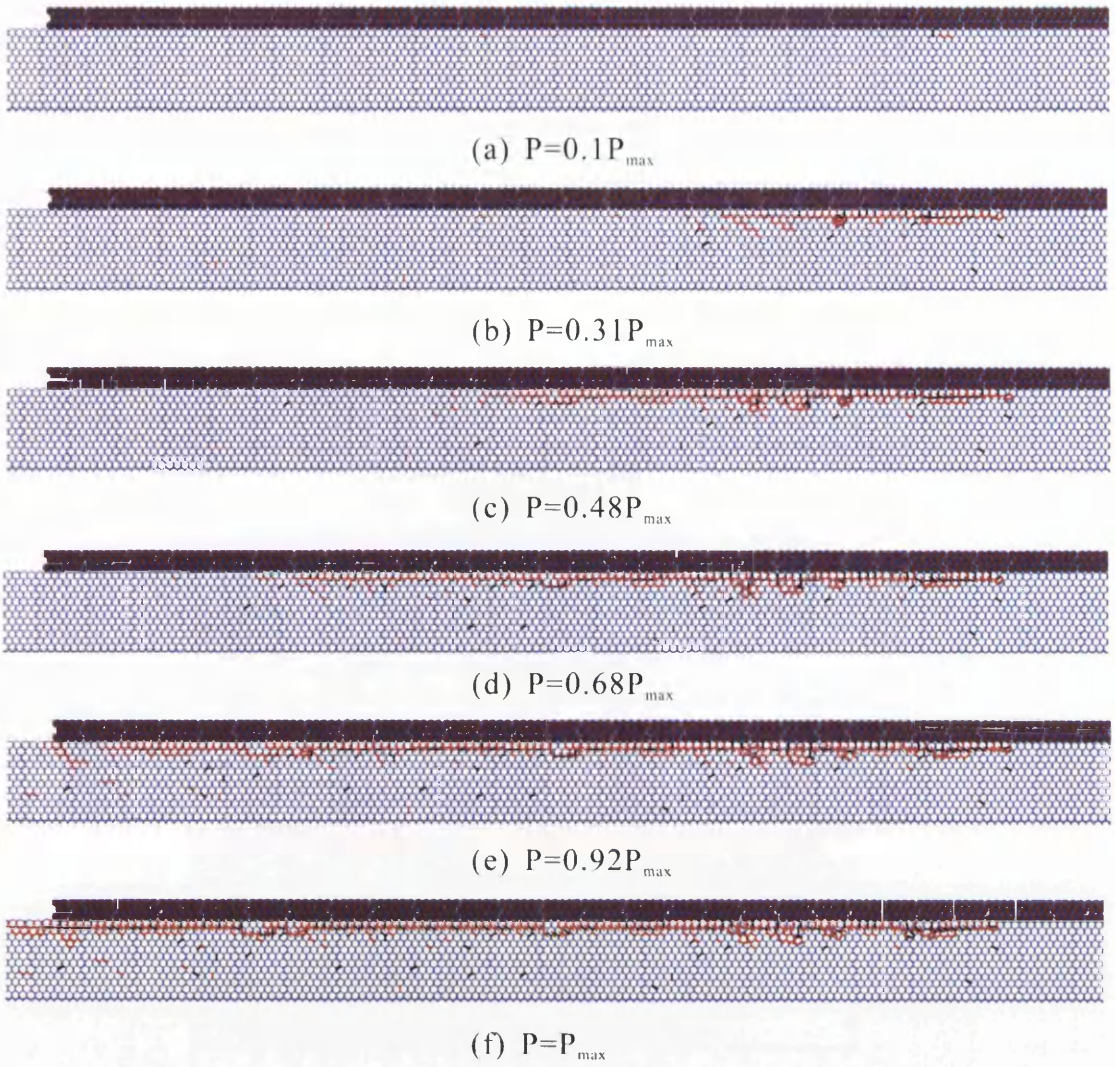

Figure 8.12: Crack propagation in FRP-to-concrete interface

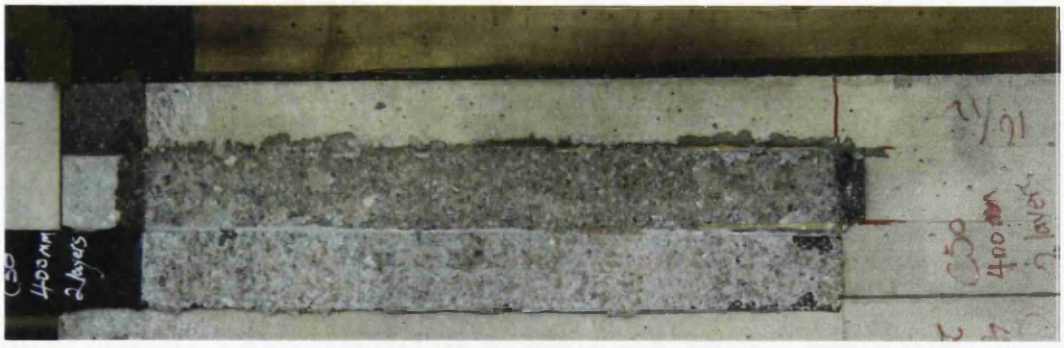

Figure 8.13: Fail mode in experimental test (Wu and Jiang, 2013).

8.2.4 Effect of free zone length

In the above analysis, numerical simulation is conducted by considering a large value of free zone where no bond is presented at the contacts between FRP and concrete particles. It has been found that the bond failure is sensitivity to the starting position of bonded surface along the specimen.

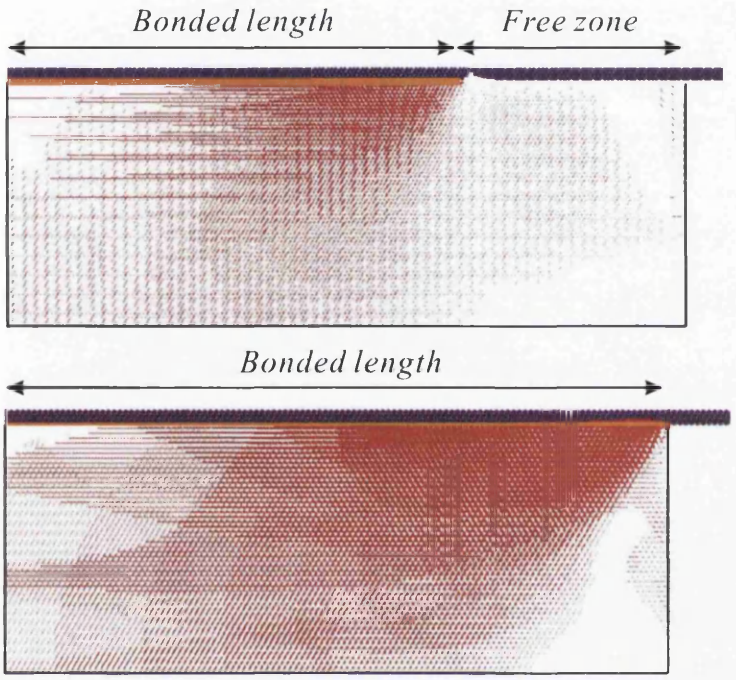

Figure 8.14: Bond force chain fabric before any bond brakeage: (a) Bonded FRP starting from front of concrete specimen; (b) Bonded FRP far from the front of concrete specimen.

When the FRP plate is pulled starting from the front side of concrete specimen, a much higher contact force will be developed in concrete (Fig.8.14a). On the other hand, by setting the bonded length far from the front side (Fig.8.14b), the contact force is much smaller due to the confinement effect and a more regular growth of delamination along the specimen can be followed during test. Similar behavior has been reported by FE analysis (Mazzotti et al., 2008).

The effect of free zone length was investigated and the results indicate that the load-carrying capacity increases with the increase of the free zone length. When the

free zone length is zero, early failure typically occurs due to concrete splitting of a prism with triangular section has been observed in experimental test (Figure 8.16). This failure mode can be captured well by the DE model (Fig.8.15). The shape of concrete prism is independent of bonded length. Similar observations have also been reported in pull-out test of steel or composite bars embedded in concrete (De Lorenzis et al., 2002). Numerical simulation in Fig.8.15 indicates that this failure mode can be well captured by the DE model.

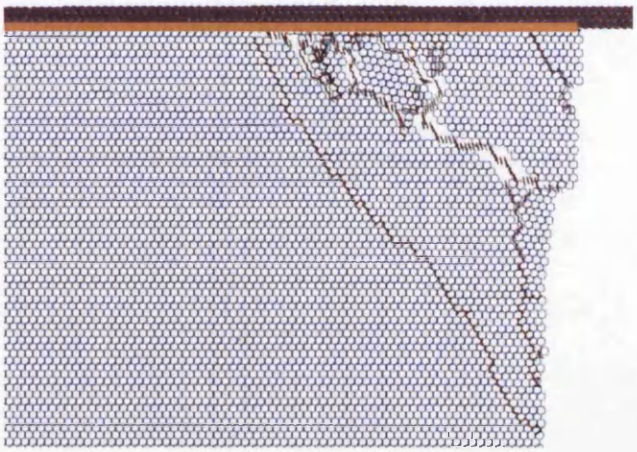

Figure 8.15: DEM model damage pattern for FRP bonded starting from the front side of concrete.

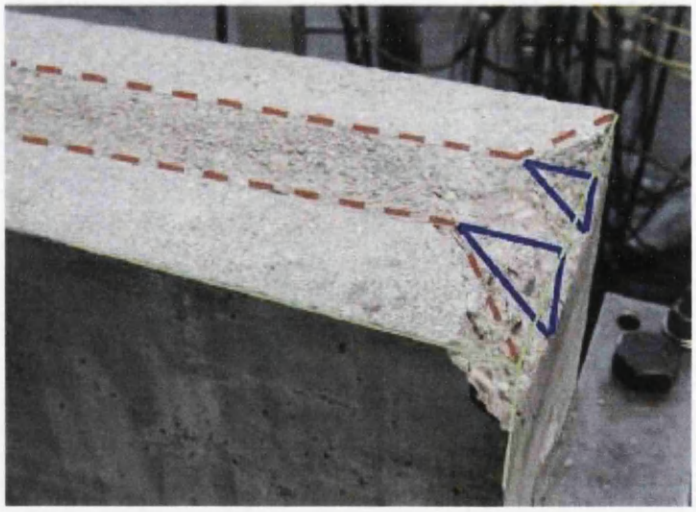

Figure 8.16: FRP plate bonded starting from the front side of concrete specimen after debonding (Mazzotti et al., 2008).

8.3 Conclusions

Pull tests on FRP reinforced concrete specimens were modeled by means of a lattice type DE model. The DE model employed displacement softening model to count for the adhesive between FRP and concrete. Heterogeneity characterization of concrete material has been considered statistically by applying the Weibull distribution to micro-parameters. Comparison with the experimental data was performed to verify the validity of the procedure. Numerical results of strain distribution in FRP and load-carrying capacity were found agreed well with results from experimental findings and finite element analysis. Then the calibrated DE model was utilized to predict the initiation and propagation of interfacial debonding. It has been found that the failure mode is mainly governed by the crack in a thin layer of concrete beneath the FRP and adhesive layer, this is because the FRP and adhesive have a higher tensile strength and lower elastic modulus than concrete. This result is in very good agreement with experimental observation. The effect of free zone length has also been investigated and the results indicated that the load-carrying capacity increased with the increase of free zone length. The early failure mode due to the boundary effect has also been captured well. The comparison studies confirm that the DEM model is capable of modelling delamination and capturing the failure propagation.

Reference

Bažant, Z., Pfeiffer, P., 1986. Shear fracture tests of concrete. Materials and structures 19, 111-121.

Chang, C., Wang, T., Sluys, L., Van Mier, J., 2002. Fracture modeling using a micro-structural mechanics approach—I. Theory and formulation. Engineering Fracture Mechanics 69, 1941-1958.

Chen, J., Teng, J., 2001. Anchorage strength models for FRP and steel plates bonded to concrete. Journal of Structural Engineering 127, 784-791.

De Lorenzis, L., Miller, B., Nanni, A., 2001. Bond of FRP laminates to concrete. ACI Materials Journal 98, 256-264.

De Lorenzis, L., Rizzo, A., La Tegola, A., 2002. A modified pull-out test for bond of near-surface mounted FRP rods in concrete. Composites Part B: Engineering 33, 589-603.

Ferracuti, B., 2006. Strengthening of RC structures by FRP: Experimental Analysis and Numerical Modeling. University of Bologna, Bologna.

Kim, H., Wagoner, M., Buttlar, W., 2008. Simulation of Fracture Behavior in Asphalt Concrete Using a Heterogeneous Cohesive Zone Discrete Element Model. Journal of materials in civil engineering 20, 552-563.

Liu, K., Gao, L., Tanimura, S., 2004. Application of discrete element method in impact problems. JSME International Journal Series A 47, 138-145.

Liu, K., Liu, W., 2006. Application of discrete element method for continuum dynamic problems. Archive of Applied Mechanics 76, 229-243.

Lu, X., Jiang, J., Teng, J., Ye, L., 2006. Finite element simulation of debonding in FRP-to-concrete bonded joints. Construction and Building Materials 20, 412-424.

Mazzotti, C., Savoia, M., Ferracuti, B., 2008. An experimental study on delamination of FRP plates bonded to concrete. Construction and Building Materials 22, 1409-1421.

Mustoe, G., Griffiths, D., 1998. An equivalent model using discrete element method (DEM), Proc. 12th ASCE Engineering Mechanics Conf., La Jolla, CA.

Popovics, S., 1973. A numerical approach to the complete stress-strain curve of concrete. Cement and concrete research 3, 583-599.

Sawamoto, Y., Tsubota, H., Kasai, Y., Koshika, N., Morikawa, H., 1998. Analytical studies on local damage to reinforced concrete structures under impact loading by discrete element method. Nuclear Engineering and Design 179, 157-177.

Sebastian, W.M., 2001. Significance of midspan debonding failure in FRP-plated concrete beams. Journal of Structural Engineering 127, 792-798.

Smith, S., Teng, J., 2002. FRP-strengthened RC beams. I: Review of debonding strength models. Engineering Structures 24, 385-395.

Tavarez, F.A., Plesha, M.E., 2007. Discrete element method for modelling solid and particulate materials. International Journal for Numerical Methods in Engineering 70, 379-404.

Teng, J., Zhang, J., Smith, S., 2002. Interfacial stresses in reinforced concrete beams bonded with a soffit plate: a finite element study. Construction and Building Materials 16, 1-14.

Van Mier, J., Van Vliet, M., 1999. Experimentation, numerical simulation and the role of engineering judgement in the fracture mechanics of concrete and concrete structures. Construction and Building Materials 13, 3-14.

Wang, J., 2006. Debonding of FRP-plated reinforced concrete beam, a bond-slip analysis. I. Theoretical formulation. International journal of solids and structures 43, 6649-6664.

Wang, J., 2007. Cohesive zone model of FRP-concrete interface debonding under mixed-mode loading. International journal of solids and structures 44, 6551-6568.

Wittmann, F.H., 1983. Fracture mechanics of concrete. Elsevier. Distributors for the US and Canada, Elsevier Science Pub. Co.

Wu, Y.-F., Jiang, C., 2013. Quantification of Bond-Slip Relationship for Externally Bonded FRP-to-Concrete Joints. Journal of Composites for Construction.

Yuan, H., Teng, J., Seracino, R., Wu, Z., Yao, J., 2004. Full-range behavior of FRP-to-concrete bonded joints. Engineering Structures 26, 553-565.

Chapter 9
Conclusions

9.1 Conclusions

The main results of this study consists of two parts, namely, the scaling laws for material properties of discrete disc and spherical assemblies, and the discrete element modelling of the fracture of concrete.

1. Scaling law. For irregular disc (2D) and spherical (3D) assemblies with linear elastic bond model (refer as parallel bond in particle flow code), the relationships between macro-scale material properties (deformability , strengths, post-peak behaviors and failure modes) and the micro-scale constitutive and physical parameters are established using dimensional analysis and numerical uniaxial tests. Parameters are categorized into two groups, experimental and specimen geometric and physical parameters (loading velocity, degree of discretisation and particle size distribution) and contact model constitutive parameters (contact stiffnesses, strengths, etc.).

- Loading velocity has a significant effect on Young's modulus, Poisson's ratio, ultimate strength stress-strain curve and damage model. Comparing to experimental data, the dynamic increase factors obtained by PFC simulations are too large especially when specimens are submitted to high strain rate. The dynamic increase factors obtained in numerical simulations are sensitive to model resolution where coarser resolutions lead to lower dynamic increase factors. Comparison study of intensity of strain rate dependence between 2D and 3D models shows that 2D models exhibit more intense rate dependence than 3D models.
- Numerical results indicate that the influences of model resolution (L/R) and particle size distribution (R_{max}/R_{min}) on the mean value of Young's modulus and Poisson's ratio obtained from 20 random packed specimens are indistinctive. However, the variance of macro-properties is reduced significantly. The mean compressive strength of 2D models starts to converge when L/R reaches the critical value of 120. On the other hand, the mean compressive strength obtained from 3D simulations increases with the increase of the model resolution, but due to limited computing power the convergence value has not been obtained.
- Young's modulus is mainly governed by the contact modulus, and the stiffness ratio has the most significant influence on Poisson's ratio. The compressive strength is mainly governed by micro-tensile when the strength ratio is smaller than 0.5 and dominated by micro-shear failure when the strength ratio is larger than 1.5 or 2 for 2D or 3D models.
- Failure mode and crack distribution are affected by the stiffness ratio and the bond strength ratio. Inclusion of both micro-shear and micro-tensile failure leads to more sophisticated damage modes. Introducing the interface friction between the specimen and the loading platen increases the probability of reproducing shear bands and the hour-glass failure mode.

- The shape of the post-peak stress-strain curve is mainly governed by the loading velocity, and increasing inter-particle friction has a minor effect.

2. Meso-level DE models, with both linear elastic-purely-brittle and softening failure laws, are adopted for simulating the fracture process of concrete specimens in the three-point bending test. The virtual concrete was conceived as a three-phase material, composed of mortar matrix, aggregates and an interfacial transition zone. Results including the complete load-CMOD curve and fracture process have been analyzed and discussed. Both brittle and softening models have obtained reasonable results compared to experimental observation. However, the results suggest that the softening model leads to more realistic predictions than the linear elastic-purely-brittle model. The multi-grade polygon aggregates generation algorithm has been successfully implemented and proved to be reliable and efficient for multi-scale simulations.

3. Pull tests on FRP reinforced concrete specimens were modeled by means of a lattice type DE model. The DE model employs a displacement softening model to account for the adhesive between FRP and the concrete. Heterogeneity characterization of the concrete material has been considered statistically by applying the Weibull distribution to micro-parameters. Numerical results of strain distribution in FRP and the load-carrying capacity were found to agree well with results from the experimental findings and finite element analysis. It has been found that the failure mode was mainly governed by the crack in a thin layer of concrete beneath the FRP and the adhesive layer. The effect of the free zone length has also been investigated and the results indicate that the load-carrying capacity increases with the increase of the free zone length. The early failure mode due to the boundary effect has also been captured well. The comparison studies confirm that the DEM model is capable of modelling delamination and capturing the failure propagation.

9.2 Future work

The following topics are suggested as future work to gain a further understanding of both the constitutive behavior of discrete assemblies and the mechanism of concrete fracture simulation.

1. Discrete element method

   - Current parametric studies of the parallel bond particle assembly are mainly based on uniaxial compression tests. The effect of micro-parameters on the macro-properties of synthetic material under mix mode loading is still not fully understood. To establish a complete and universal parameter calibration procedure remains to be a big challenge.

   - Parametric studies of other micro-scale contact models (e.g., displacement softening model) are needed to improve the reliability and repeatability of the simulated results. Particularly when various contact models are involved in one single model.

   - In recent years, parallel computing technology growths rapidly and has been successfully implemented in large-scale analysis. Meso-scale modelling requires extensive computing effort. Thus development of relevant parallel algorithms will significantly improve the computational efficiency. More recently, GPU (Graphics Process Unit) based DEM code has been successfully implemented and the performance appears to be inspiring.

2. Meso-scale concrete fracture modelling

   - Statistic description should also be introduced into the contact parameters for each component phase to realistically model the macro-scale constitutive behavior of concrete. In our meso-scale simulations, contacts within the same phase are assigned the same stiffnesses and strengths. The resultant

load-deformation relationship appears to be brittle. Only a few micro-failure events occur. The ductility of synthetic material could be better controlled.

- The constitutive behavior of the interfacial transition zone between mortar matrix and aggregates is extremely complicated. Additional experimental investigations and more sophisticated numerical model are necessary. The thickness of interfacial transition zone is neglected in the present study. In reality, the thickness of a typical interfacial transition zone is around 10-30 micrometers and contains a gradient of properties and can have a significant effect on material properties.

- The DE model developed here can be extended to investigate more sophisticated problems such as: the effect of aggregate size distribution, content, types and shape on the mechanical properties, load-deformation relationship and damage behavior of normal or high strength concrete under various loading conditions. With a better computer infrastructure becoming available, three dimensional models can be implemented and it is reasonable to expect more realistic numerical results can be obtained.